# Exciton spectroscopy of van der Waals heterostructures


Dissertation
zur Erlangung des Doktorgrades der Naturwissenschaften
(Dr. rer. nat.)
der Fakultät für Physik der Universität Regensburg

vorgelegt von

Philipp Nagler
aus Erlangen

im Jahr 2018

Das Promotionsgesuch wurde eingereicht am: 24.01.2018
Die Arbeit wurde angeleitet von: Prof. Dr. Tobias Korn

| | | |
|---|---|---|
| Prüfungsausschuss: | Vorsitzender: | Prof. Dr. Andreas Schäfer |
| | 1. Gutachter: | Prof. Dr. Tobias Korn |
| | 2. Gutachter: | Prof. Dr. Rupert Huber |
| | weiterer Prüfer: | Prof. Dr. Franz Gießibl |

# Contents

Chapter 1

# Introduction

The concept of the heterostructure is one of the most important pillars of solid state physics [Mit99]. Initiated by technological advances such as the invention of molecular beam epitaxy at the Bell laboratories [Cho70], the deterministic fabrication of atomically sharp interfaces between different materials has allowed to realize and study quantum mechanical model systems, such as potential wells or tunnel barriers. There, quantum confinement is enabled by the small dimensions of the devices in the nanometer regime, which are comparable to the extent of the electronic wave function. The resulting novel experimental playground allows one to test the predictions from quantum mechanics and led to fundamental discoveries such as the observation of the quantum Hall effect in a two-dimensional electron system [Kli80].
At the same time, the enormous technological advancements and the resulting economic progress over the last decades can be traced back in substantial parts to the development and steady miniaturization of solid-state heterostructures. Numerous building blocks of modern information technology such as thin-film transistors, light-emitting diodes or lasers could be realized via this building principle. The importance of these developments was highlighted with the Nobel Prize in physics in 2000 for Kroemer, Kilby and Alferov for "developing semiconductor heterostructures used in high-speed- and opto-electronics" and "the invention of the integrated circuit". Therefore it is obvious that the continuous improvement and evolution of heterostructure systems is of fundamental importance for both basic scientific research and technological applications. In this respect, the ultimate limit of miniaturization in vertical dimensions is strictly predetermined by the thickness of a single atomic layer, which is in the sub-nanometer regime.

Recently, the notion of the heterostructure was greatly expanded by the discovery of atomically thin van der Waals crystals. This novel research field was initiated by the successful isolation of graphene as a monolayer of $sp^2$-hybridized carbon [Nov04]. Due to their thickness of only one atomic layer, such monolayers represent the ultimate quantum limit in two dimensions. The peculiar electronic properties of graphene [Cas09] allowed for the observation of unique fundamental phenomena such as the half-integer quantum hall effect [Nov05a, Zha05] or Klein tunneling [You09].

However, the lack of a band gap strongly hampers the implementation of graphene into optical devices and applications or thin-film field effect transistors. Novoselov *et al.* [Nov05b] demonstrated in 2005 that the isolation of monolayer crystals by mechanical cleavage is readily extendable to other van der Waals materials such as $MoS_2$ or $NbSe_2$. Specifically, $MoS_2$ belongs to the family of transition metal dichalcogenides (TMDCs) and is an indirect semiconductor in its bulk form [Gou97]. Five years later, by using photoluminescence spectroscopy the seminal experimental works by Mak *et al.* [Mak10] and Splendiani *et al.* [Spl10] demonstrated that $MoS_2$ is a direct band gap semiconductor in its monolayer form. These studies marked the beginning of the vibrant research field of two-dimensional semiconductors, which experienced a staggering growth ever since.

The optical transitions in atomically thin TMDCs are governed by the formation and dissociation of Coulomb-bound quasiparticles, so-called excitons [Kli12]. As a composite many-body state, an exciton consists of an electron and a hole and can be understood as an elementary excitation in a semiconductor. Due to the spatial confinement and the reduced dielectric screening in monolayer TMDCs, excitons in these materials possess binding energies on the order of 0.5 eV and are thus highly stable even at room temperature [Wan18]. As a result, the fundamental optical properties in these materials are determined by pronounced excitonic resonances, with up to 20 % light absorption in the monolayer limit depending on the energetic region [Li14a]. This strong interaction further enables the formation of more intricate many-body states such as charged excitons [Mak13] and excitonic molecules in the form of biexcitons [You15].

Moreover, owing to the crystal structure in monolayer TMDCs combined with strong spin-orbit interaction, a peculiar coupling of spin and the global extrema in momentum space, so-called valleys, emerges. This spin-valley coupling can be harnessed to optically address and read out a valley polarization using circularly polarized light [Xia12, Mak12, Zen12]. In analogy to the concept of spintronics, which makes use of the spin as the information carrier, this gives rise to the field of valleytronics in

two-dimensional materials, where the so-called valley pseudospin serves as a switchable quantity [Sch16]. In recent years, this has led to the observation of fascinating fundamental phenomena such as the valley Hall effect [Mak14] or ultrafast switching of the valley pseudospin on subcycle timescales [Lan18].

Atomically thin crystals are not only subject to intriguing physics, they can also serve as building blocks for a fundamentally novel type of heterostructure, the so-called van der Waals heterostructure [Gei13]. In such a system, the different functionalities of the individual monolayers can be combined to create an entirely novel material platform in the ultimate thickness limit. Over the last years, a variety of transfer techniques was developed to deterministically fabricate heterostructures consisting of different van der Waals crystal sheets [Fri18b]. In stark contrast to artificially grown semiconductor heterostructures such as AlGaAs/GaAs, van der Waals heterostructures are not subject to lattice matching conditions due to the chemically saturated surfaces. As a result, the twist angle between different layers emerges as a hitherto inaccessible degree of freedom. The sheer endless parameter space of van der Waals heterostructures renders these structures one of the currently most promising testbeds of condensed matter physics.

Naturally, it can be expected that the properties of excitons in TMDC-based heterostructures can strongly deviate from their physical behavior in the individual monolayers. Novel excitonic physics in heterostructures could, for instance, stem from the varying dielectric environment or the interaction between different TMDC monolayers. This calls for detailed optical studies to advance our understanding of light-matter interaction in such systems.

In this thesis, photoluminescence (PL) spectroscopy is employed to shed light on the physics of excitons in van der Waals heterostructures. Two distinct heterostructures will be fabricated and thoroughly investigated during the course of the work. The first material platform is an atomically thin vertical heterostructure consisting of two different semiconducting monolayer TMDCs, $WSe_2$ and $MoSe_2$. In this system, the spatial separation of electrons and holes gives rise to a novel excitonic species, called interlayer exciton. Due to their comparatively long lifetimes in the nanosecond regime, these excitons are particularly promising for future applications [Riv18]. In the second part, a semiconducting monolayer of $WS_2$ is encapsulated by two thin sheets of the insulating hexagonal boron nitride (hBN). The surrounding by hBN will allow to study the excitonic resonances of the monolayer TMDC with a drastically reduced spectral linewidth. In particular, this will positively affect the observation of biexcitons and the subsequent investigation of this many-body state in high magnetic fields.

This thesis is structured as follows: Chapter 2 gives a brief overview of the most important theoretical foundations for this thesis. This includes the band structure and the properties of excitonic quasiparticles in monolayer TMDCs, along with the intricate valley physics in these systems. Furthermore, the concept and realization of van der Waals heterostructures will be described in more detail.
Subsequently, chapter 3 elaborates on the experimental techniques employed during this work. The photoluminescence setup is presented, including the realization of time-resolved measurements and the magneto-PL studies at the High Field Magnetic Laboratory in Nijmegen. Additionally, the sample fabrication of van der Waals heterostructures by a deterministic transfer approach is discussed.
In chapter 4, a detailed spectroscopic study of interlayer excitons in a $WSe_2/MoSe_2$ heterostructure is presented. This involves the investigation of the dynamics and interaction effects of this excitonic species. Moreover, magneto-PL studies on interlayer excitons in high magnetic fields reveal the peculiar valley physics of the investigated heterostructure.
The experiments presented in chapter 5 deal with the physics of biexcitons in an hBN-encapsulated monolayer $WS_2$. The encapsulation with hBN gives access to spectrally ultra-narrow linewidths of all excitonic features, including the biexciton. By employing magneto-PL measurements, further insight on the momentum space structure of this many-body state will be gained.
The experimental findings and the resulting conclusions are summarized in chapter 6 together with an outlook on possible future research directions.

Chapter 2

# Theoretical foundations

## 2.1 Basic properties of atomically thin transition metal dichalcogenides

### 2.1.1 Crystal structure

Transition metal dichalcogenides are a class of materials with the chemical formula $MX_2$, where M is a transition metal from subgroup IV, group V or group VI of the periodic table and X is a chalcogen. The focus of this thesis will be on TMDCs, where the transition metal is either molybdenum (Mo) or tungsten (W) from group VI and the chalcogen is either sulfur (S) or selenium (Se), resulting in four different compounds, namely $MoS_2$, $MoSe_2$, $WSe_2$ and $WS_2$. These four configurations are all semiconducting and can be considered the most commonly studied systems for optical experiments within the family of TMDCs. While the research on TMDCs in the atomically thin limit has just emerged over the past couple of years, the structural properties of the respective bulk systems have already been examined in detail many decades ago. The first basic study on the crystal structure of a TMDC was published in 1923 by Linus Pauling on the prototypical material $MoS_2$ [Dic23].

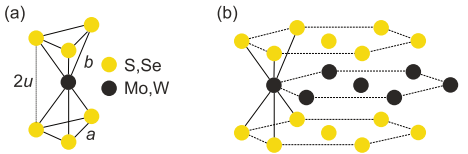


**Figure 2.1** | (a) Trigonal prismatic unit cell of a $MX_2$ TMDC. (b) Arrangement of the hexagonal crystal lattices in a monolayer TMDC.

Naturally occurring TMDCs crystallize either in the 2H or 3R stacking order, whereas the 2H type is much more commonly found. Therefore, only crystals of the 2H polytype will be treated in the following and studied experimentally in this work. The relevant unit cell is trigonal prismatic, where the transition metal is in the center and the six chalcogen atoms are situated at the corners of the cell, see Fig. 2.1(a). The distance between the chalcogen atoms in the same plane is given by $a$, and $b$ is the separation between a chalcogen atom and a transition metal. The height of a single monolayer is determined by $2u$. In general we have $2u = a$ and $b = \sqrt{\frac{7}{12}}a$ for the trigonal prismatic unit cell. Using values for the prototypical TMDC $MoS_2$ [Wil69], we obtain $a = 3.16$ Å, $b = 2.41$ Å resulting in a thickness of a monolayer of about 6 Å. The related space group of the monolayer is $D_{3h}$. Note that the monolayer lacks an inversion center, giving rise to the coupling of the spin and valley degree of freedom, see section 2.3. The crystal arrangement of a monolayer TMDC is further depicted in Fig. 2.1(b), showing that one monolayer consists of three hexagonal lattices of a single type of atoms in a honeycomb-like arrangement.

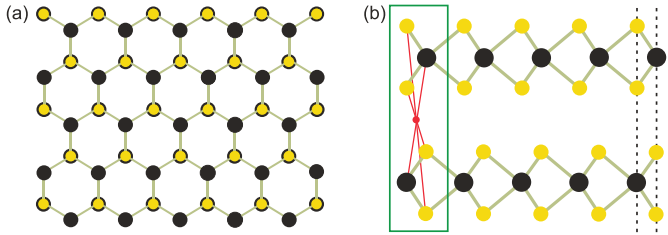


**Figure 2.2** | (a) Top view of the crystal structure of 2H TMDCs. (b) Side view of the 2H crystal structure, where the unit cell that reconstructs the whole lattice is indicated in green. The red dot together with the respective red lines indicate the center of inversion, present in any even-layered 2H TMDC crystal. The chalcogen atoms in the upper layer are situated exactly above the metal atoms in the lower layer, as indicated by the dashed lines.

Stacking individual monolayers on top of each other results in a bulk crystal that follows a $D_{6h}$ point symmetry group. A top view of such a 2H TMDC is depicted in Fig. 2.2(a), which highlights the honeycomb-like configuration of the atoms. In the case of the 2H polytype, which can be described by a bilayer system, the two monolayers are rotated by 60° with respect to each other and the transition metals of the upper layer are situated exactly above the chalcogen atoms of the second layer, see Fig. 2.2(b). As can be deduced from Fig. 2.2(b), the bilayer has an inversion center in the middle of the van der Waals gap (red dot), as the whole lattice can be reconstructed by the unit cell indicated in green. Consequently, even-numbered 2H TMDCs are always inversion-

symmetric, while odd-numbered are not. It is important to note that strong covalent bonds act within a single monolayer while the bonding between the stacked monolayers follows from comparatively weak van der Waals forces. The resulting anisotropy of the binding forces enables the mechanical exfoliation of TMDCs, in analogy to graphene, down to the monolayer limit [Nov04, Nov05b], see section 3.2.

### 2.1.2 Band structure, spin-orbit interaction and photoluminescence

#### Electronic band structure

A thorough understanding of the electronic band structure of a semiconductor is of key importance since the optical properties are largely determined by the energetic configuration in momentum space. In this respect, the gradual transition in TMDCs from an indirect gap in the bulk to a direct band gap in the monolayer limit [Mak10, Spl10] is largely responsible for the tremendous scientific interest of solid-state research in atomically thin materials. To start with, the Brillouin zone of typical TMDCs such as $MoS_2$ or $WSe_2$ is schematically depicted in Fig. 2.3(a). As can be seen, due to the hexagonal lattice in real space (see Fig. 2.2), the Brillouin zone also exhibits a hexagonal shape. The most important points of high symmetry are the Γ point in the center and the K points at the corners. A cut-through in the (001)-plane is shown in Fig. 2.3(b). The two inequivalent K points in the two-dimensional Brillouin zone, called $K^+$ and $K^-$, result from the fact that the crystal structure of TMDCs is based on two inequivalent sublattices [Bro72].

In the case of bulk TMDCs, both time-reversal symmetry $E_\uparrow(k)=E_\downarrow(-k)$ and inversion symmetry $E_\uparrow(k)=E_\uparrow(-k)$ hold, where $E_{\uparrow,\downarrow}(k)$ is the energy of the respective spin state at a certain wave vector $k$. This results in the Kramers degeneracy $E_\uparrow(k)=E_\downarrow(k)$ for

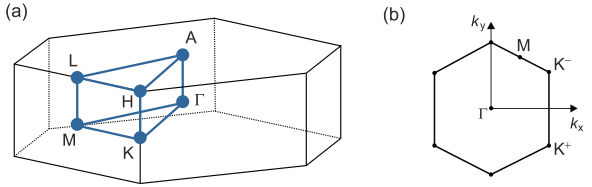


**Figure 2.3** | (a) The Brillouin zone of a bulk 2H TMDC and the corresponding high-symmetry points. (b) The hexagonal Brillouin zone in the 2D limit with the Γ point and the two inequivalent $K^+$ and $K^-$ points.

the different spin states in bulk TMDCs.

First band structure calculations for bulk TMDCs, mainly on $MoS_2$, date back to the 1970s and reported an indirect gap resulting from a global maximum of the valence band at the Γ point and a global minimum of the conduction band between the Γ and the K point [Bro72, Mat73a, Mat73b]. However, it was generally assumed that atomically thin TMDCs are unstable under ambient conditions until the first experimental exfoliation of graphene in 2004 [Nov04], which could explain the general lack of theoretical studies for the two-dimensional case. Following early calculations of the band structure of monolayer TMDCs [Alb02, Li07], the work by Lebègue *et al.* [Leb09] is considered the first study to suggest the direct band gap of monolayer $MoS_2$, which was confirmed by various following works [Mak10, Spl10, Kuc11, Yun12, Zha13b, Rol14]. The evolution of the bandgap with decreasing layer thickness for two prototypical TMDCs, namely $MoS_2$ and $WS_2$, is shown in Fig. 2.4.

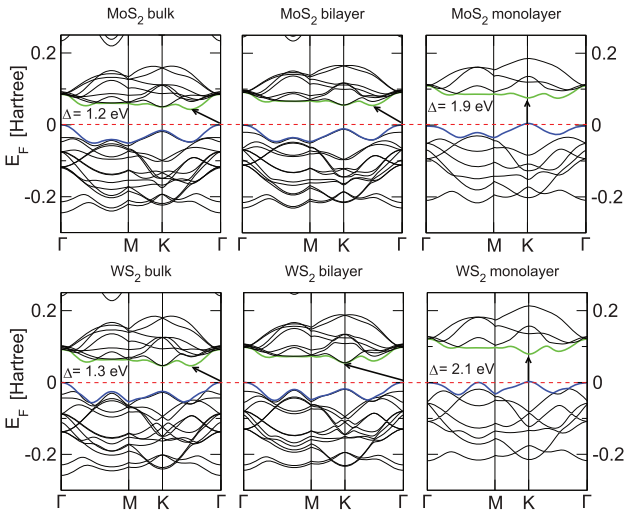


**Figure 2.4 |** Band structure calculations of $MoS_2$ and $WS_2$ performed by DFT for the case of bulk, bilayer and monolayer. The highest-lying valence band and the lowest-lying conduction band are marked in blue and green respectively. The position of the energetically lowest band gap is indicated by arrows. Figure taken from [Kuc11].

With decreasing number of layers, the fundamental indirect gap increases until the monolayer limit, where the material becomes an atomically thin direct gap semiconductor. Qualitatively, this transition can be understood by analyzing the atomic orbitals

contributing to the states near the Γ and K points, which will be shortly discussed in the following for the case of $MoS_2$ but is largely applicable to the other semiconducting TMDCs [Spl10, Kuc11]. The density of states at the Γ point comprises a linear combination of $d$-orbitals from molybdenum and antibonding $p_z$-orbitals originating from sulfur. The latter are highly sensitive to the surrounding and therefore also to the number of crystal layers. In contrast, the states at the K points are mostly composed of strongly localized $d$-orbitals of the transition metal, thus largely unaffected by the adjacent layers. Hence, by gradually thinning down the crystal, the states at the Γ point change their energy to higher levels while the energetic splitting at the K points remains basically the same, finally resulting in a direct gap at the K point in the monolayer limit.

**Spin-orbit interaction**

Additionally, to fully describe the electronic band structure of monolayer TMDCs, it is necessary to include the influence of spin-orbit interaction arising from the metallic $d$-orbitals [Zhu11, Xia12, Zen13]. For crystals with broken inversion symmetry, the Kramers degeneracy $E_\uparrow(k)$=$E_\downarrow(k)$ is lifted. In combination with the effect of spin-orbit interaction, this results in a spin-dependent split-up of conduction and valence bands at various points in the Brillouin zone [Xia12, Xu14]. As both conduction and valence band show an energetic splitting, the spin degeneracy is fully lifted, leading to chiral optical selection rules, which will be discussed in more detail in section 2.3.
For the valence band maximum at the K points, the splitting has a positive value for all studied monolayer TMDCs in this thesis and is on the order of a few hundreds of meV [Che12, Xia12, Zha14, Miw15] with good agreement between experimental and theoretical values (see Table 2.1). The large energy scale of the splitting results from the non-linear scaling of the spin-orbit interaction with the atomic number Z based on the approximation known from atomic physics ($\propto$ $Z^4$) taking into account that molybdenum (Z = 42) and tungsten (Z = 72) are relatively heavy atoms. The influence of spin-orbit interaction on the valence band splitting is also shown in Fig. 2.5(a) for the case of monolayer $MoSe_2$. Experimentally, the energetic splitting of the valence band due to spin-orbit interaction is accessible by angle-resolved photoemission spectroscopy (ARPES), as shown in Fig. 2.5(b) for the representative case of monolayer $MoSe_2$. Since this technique relies on exciting electrons from occupied states below the Fermi level into vacuum, it is only possible to determine the structure of the valence band.
At the conduction band minimum, a smaller but also significant splitting arises due to an admixture of chalcogen $p$-orbitals and $d_{xz}$- and $d_{yz}$-orbitals from the transition

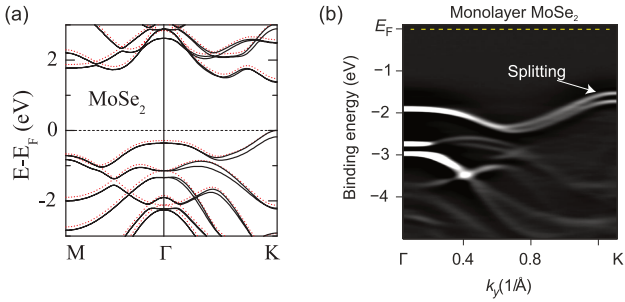


**Figure 2.5 |** (a) DFT band structure calculations for monolayer $MoSe_2$ with (black line) and without (red dotted line) inclusion of spin-orbit interaction. Figure taken from [Zhu11]. (b) Second derivative of angle-resolved photoemission spectra (ARPES) of monolayer $MoSe_2$, demonstrating the valence band splitting at the K point. Figure taken from [Zha14].

metals. Importantly, theoretical calculations predict that the sign of the conduction band splitting depends on the relative strength of these contributions, resulting in a positive splitting for molybdenum-based TMDCs ($MoS_2$ and $MoSe_2$) and a negative splitting for tungsten-based TMDCs ($WS_2$ and $WSe_2$) [Koś13, Kor15]. Experimentally, the negative sign of the conduction band splitting in $WX_2$ compounds and the positive sign in $MoSe_2$ has been confirmed by temperature-dependent PL studies [Zha15c] and measurements with transverse magnetic fields [Zha17b, Mol17]. However, the sign of the conduction band splitting in $MoS_2$ is still under debate due to contradicting experimental results. Table 2.1 summarizes a selection of theoretical and experimental values of the conduction- and valence band splitting of the relevant monolayer TMDCs.

| | $MoS_2$ | $MoSe_2$ | $WS_2$ | $WSe_2$ |
|---|---|---|---|---|
| $\Delta_{SO,v}$ (meV) Theo. | 148 [Zhu11] | 183 [Zhu11] | 426 [Zhu11] | 456 [Zhu11] |
| $\Delta_{SO,v}$ (meV) Exp. | 132 [Zha15d] | $\approx$180 [Zha14] | 410 [Zha13a] | 426 [Zha13a] |
| $\Delta_{SO,c}$ (meV) Theo. | 3 [Kor15] | 22 [Kor15] | –32 [Kor15] | –37 [Kor15] |
| $\Delta_{SO,c}$ (meV) Exp. | $\approx$1 [Mar17]<br>$\approx$–100 [Mol17] | $\approx$30 [Wan17b] | –55 [Wan17a]<br>–40 [Wan17a] | –46 [Zha17b] |

**Table 2.1:** Theoretical and experimental values of the spin-orbit splitting $\Delta_{SO}$ for the conduction- and valence band at the K point for different TMDCs.

The presented experimental and theoretical values for the spin-orbit splitting are not fully comparable, as the experimental values include the electron-hole Coulomb exchange energy, which is not considered in the theoretical calculations.

### Photoluminescence of monolayer TMDCs

The tremendous interest in atomically thin TMDCs was sparked by two experimental studies on the photoluminescence properties of $MoS_2$ in dependence of the number of layers [Mak10, Spl10]. Generally, photoluminescence is understood as the emission of photons in a material after excitation by an external light source, usually a laser.

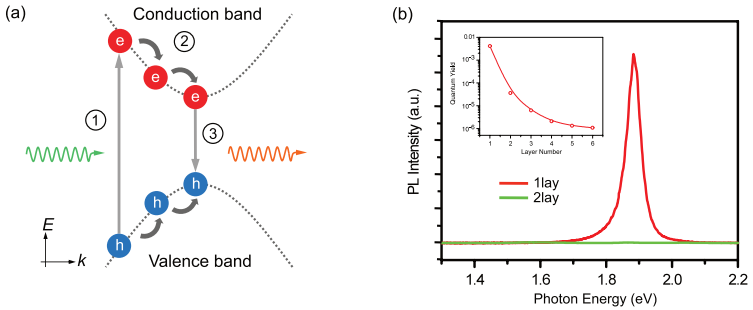


**Figure 2.6 |** (a) Schematic photoluminescence process in a direct gap semiconductor: (1) Excitation of an electron to the conduction band by a laser above the band gap. (2) Electrons and holes relax towards the direct band gap by emission of phonons. (3) Radiative recombination leads to the emission of a photon. (b) PL of monolayer (red) and bilayer (green) $MoS_2$. The inset shows the quantum yield of the material depending on the number of layers. Figure taken from [Mak10].

On a basic level, the process leading to photoluminescence in a semiconductor can be described by a three-step model, as depicted in Fig. 2.6(a). First, the excitation by a laser with a photon energy larger than the bandgap of the material excites an electron from the valence band to the conduction band, leaving a positively charged hole in the valence band behind (1). In the following, electrons and holes relax to the bottom of the conduction band and the top of the valence band under the momentum-conserving emission of phonons (2). Finally, electron and hole recombine at the direct band gap leading to the emission of a photon (3). Momentum conservation during excitation and recombination leads to approximately vertical transitions in the $E$-$k$ diagram (see Fig. 2.6(a)) due to the negligible momentum of photons.

The indirect to direct band gap transition from bulk to monolayer TMDCs as discussed previously can be readily observed in PL experiments (see Fig. 2.6(b)). In the case of an indirect band gap (bulk down to bilayer), the PL is strongly suppressed since an additional phonon is required for the emission of a photon to fulfill momentum conservation. However, the PL drastically increases (red line in Fig. 2.6(b)) in the case of

monolayer $MoS_2$ due to the direct band gap of the material. The strong increase of PL intensity from the bulk crystal to the monolayer limit was also observed in the other prominent semiconducting TMDCs (see [Ton13, Zha13a] for the first layer-dependent PL experiments on $MoSe_2$, $WSe_2$ and $WS_2$) directly confirming the theoretical predictions of a band gap transition.

## 2.2 Excitonic quasiparticles in monolayer TMDCs

Up to now, we have treated the properties of photo-excited electrons and holes by the band structure within the single-particle approximation. However, to adequately describe the optical properties of atomically thin TMDCs, it is of fundamental importance to include the effects of Coulomb interaction between the created electron-hole pair. The resulting correlated quasiparticle is called an exciton [Yu10, Kli12].
Excitons in solids can be usually separated into two limiting cases, either Frenkel-like or Wannier-Mott-like, depending on the spatial extent of the exciton and the related binding energy of the electron-hole pair. Frenkel excitons are strongly localized and exhibit an approximate electron-hole separation on the order of the lattice constant, leading to large binding energies of about $0.1-1\,\mathrm{eV}$ [Fre31, Bar14]. They are found in materials with a low dielectric constant, for instance in molecular crystals. Wannier-Mott excitons, on the other hand, are typically present in inorganic semiconductors such as GaAs with a high dielectric constant [Wan37, Rid13]. Due to the strong dielectric screening, Wannier-Mott excitons are weakly bound and can move quasi-freely through the crystal. Consequently, their radius is much larger than the lattice spacing and the binding energy is typically on the order of $0.1-0.01\,\mathrm{eV}$. Due to their lightly-bound nature it is possible to apply the effective mass approximation for parabolic bands in the case of Wannier-Mott excitons and thus to describe their energetic states by a modified Rydberg series, in close analogy to the hydrogen atom.
In this respect, both Wannier-Mott and Frenkel characteristics can at first glance be attributed to excitons in monolayer TMDCs. As will be discussed in the following in more detail, they possess very large binding energies on the order of hundreds of meV (Frenkel type) but also show a spatial extension of several lattice constants and can be described by a hydrogen-like model (Wannier-Mott type). Nevertheless, experimental and theoretical evidence shows that excitons in monolayer TMDCs are most adequately described within the Wannier-Mott picture [Wan18].
Figure 2.7(a) schematically illustrates an exciton in a two-dimensional crystal in real space. Electron and hole are separated by several unit cells, implying a Wannier-

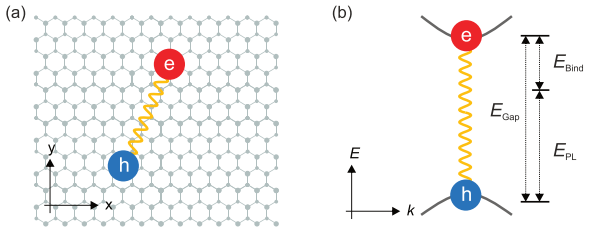


**Figure 2.7 |** (a) Schematic real-space depiction of an electron-hole pair in a Wannier-Mott exciton picture, spreading over several unit cells. (b) Momentum space representation of an exciton in a direct gap semiconductor. The binding energy ($E_{\mathrm{Bind}}$) and the optical bandgap ($E_{\mathrm{PL}}$) add up to the quasiparticle band gap ($E_{\mathrm{Gap}}$).

Mott description. As can be seen in Fig. 2.7(b), the energy $E_{\mathrm{PL}}$ that is emitted in photoluminescence (optical bandgap) is not equal to the quasiparticle band gap $E_{\mathrm{Gap}}$ but lowered by the binding energy of the exciton $E_{\mathrm{Bind}}$, resulting in $E_{\mathrm{Gap}}$=$E_{\mathrm{PL}}$+$E_{\mathrm{Bind}}$. Strictly speaking the representation of an exciton in the single-particle picture as shown in Fig. 2.7(b) is not correct since the exciton is a two-particle state with its own dispersion relation (see Fig. 2.9(a)).

### Exciton binding energy in monolayer TMDCs

High exciton binding energies have been experimentally extracted for all prototypical monolayer TMDCs, including $WS_2$ [Che14b, Sti16a, Ye14], $WSe_2$ [He14, Poe15], $MoS_2$ [Klo15, Rig16] and $MoSe_2$ [Uge14, Zha15a] (see [Wan18] for a comprehensive summary). The respective $E_{\mathrm{Bind}}$ values of the exciton range roughly from about 300 meV to 800 meV. These values were determined by a variety of experimental techniques, for instance linear reflectance [Che14b], scanning tunneling spectroscopy [Uge14] or magneto-reflectance measurements [Sti16a]. Similar values for the excitonic states and their binding energies have been obtained by a variety of theoretical approaches [Che12, Kom13, MS13, Qiu13, Tru16, Van17]. However, even though these high binding energies would suggest a Frenkel-like picture, it was shown that the wavefunction of excitons in monolayer TMDCs can extend over several nanometers [Che14b, Ple16b, Sti16a, Sti18] with a typical exciton Bohr radius of $a_B$ ∼1 nm [Sti16b, Ple16b]. The Wannier-Mott picture of excitons in monolayer TMDCs was further corroborated by the applicability of the effective mass approximation and the observation of a Rydberg-like series of the excitonic resonances [Che14b, He14, Hil15].

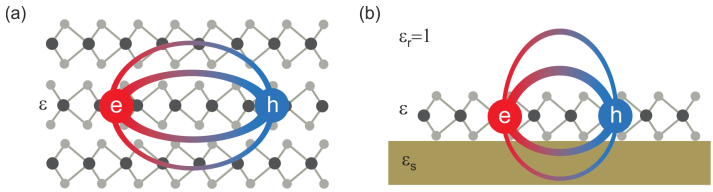


**Figure 2.8** | (a) Exciton in the three-dimensional bulk case. All of the field lines arising from the Coulomb interaction run within the crystal, which has a homogeneous dielectric constant $\epsilon$. (b) Monolayer TMDC on a substrate. The electric field lines permeate both the material and the surroundings, which typically have a far lower dielectric constant.

To understand the origin of the high binding energies in monolayer TMDCs, we have to take into account three contributions. First, following the hydrogen-like description of Wannier-Mott excitons, the reduction to the strictly two-dimensional limit leads to an increase of the binding energy by a factor 4 in comparison to the three-dimensional case [Kli12]. Moreover, the effective masses of electrons and holes, $m_\mathrm{e}$ and $m_\mathrm{h}$, which directly contribute to the binding energy are comparatively large in monolayer TMDCs at the K points, on the order of about $0.5\,m_0$, where $m_0$ is the mass of the free electron [Liu13]. Finally, we have to consider the effects of reduced dielectric screening on the binding energy in the monolayer case. As shown in Fig. 2.8(a), the electric field lines between electron and hole in the bulk case are situated within the crystal. The relatively high dielectric constants of TMDCs of $\epsilon \approx 10$ result in a strong screening and consequently lead to a reduction of the exciton binding energy in bulk crystals. In the case of a monolayer TMDC, which is typically placed on a substrate with a dielectric constant $\epsilon_\mathrm{s}$ and surrounded by air or vacuum ($\epsilon_\mathrm{r} = 1$), the field lines now mostly run outside of the crystal and experience a different dielectric environment. Hence, the screening is drastically reduced, resulting in a strongly increased binding energy of the exciton. To adequately describe this scenario within the effective mass approximation a potential of the following form is usually applied [Ryt67, Kel79]:

$$V(\rho) = -\frac{\pi e^2}{(1+\epsilon_\mathrm{s})r_0}\left[H_0\left(\frac{\rho}{r_0}\right) - Y_0\left(\frac{\rho}{r_0}\right)\right] \tag{2.1}$$

$H_0$ and $Y_0$ are first order Struve- and Neumann functions, $\rho$ is the relative electron-hole coordinate $\rho = \rho_\mathrm{e} - \rho_\mathrm{h}$, $r_0$ the effective screening length without substrate and $\epsilon_\mathrm{s}$ the dielectric constant of the substrate. The resulting energy spectrum of the exciton deviates from the ideal 2D hydrogen model, i.e. for small $\rho$ it behaves like $\log(\rho)$ and for large $\rho$ it is proportional to $1/r$ [Che14b, He14, Tru16].

### Radiative exciton dynamics in monolayer TMDCs

The strong interaction of electrons and holes in monolayer TMDCs directly affects the exciton dynamics in these systems. To analyze the optical activity of excitons it is important to consider the so-called light cone of excitons, see Fig. 2.9(a).

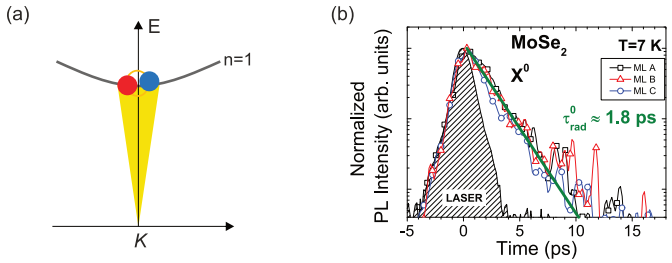


**Figure 2.9 |** (a) Parabolic dispersion of the exciton ground state with center-of-mass momentum $K$ including a schematic illustration of the light cone. Radiative recombination of excitons is only allowed within the cone. (b) Time-resolved PL spectra of the exciton resonance in monolayer $MoSe_2$ using quasi-resonant excitation via a phonon resonance. Figure taken from [Rob16].

In the two-particle picture, excitons have a dispersion with a center-of-mass momentum $K$, taking into account the correlated motion of electrons and holes. Owing to energy- and momentum conservation, the radiative recombination of excitons is only allowed within the light cone, which is based on the linear dispersion of photons (see Fig. 2.9(a)), while excitons outside of the light cone are essentially dark [Yu10]. Therefore, following non-resonant excitation, excitons have to relax towards the light cone in order to become optically bright.

In general, the total decay time $\tau_{\mathrm{tot}}$ of an exciton population is comprised by the effective radiative $\tau_{\mathrm{rad}}^{\mathrm{eff}}$ and non-radiative $\tau_{\mathrm{nonrad}}$ decay time via [Kli12]:

$$\frac{1}{\tau_{\mathrm{tot}}} = \frac{1}{\tau_{\mathrm{rad}}^{\mathrm{eff}}} + \frac{1}{\tau_{\mathrm{nonrad}}} \tag{2.2}$$

The effective radiative lifetime can be written as $\tau_{\mathrm{rad}}^{\mathrm{eff}} = \tau_{\mathrm{rad}}/\alpha$, where $\tau_{\mathrm{rad}}$ is the radiative recombination time of excitons in the radiative cone and $\alpha$ is the fraction of the total exciton population that lies within the radiative cone. Hence, the effective radiative lifetime is always longer than the radiative lifetime, since a considerable part of the exciton population is situated outside of the light cone, depending on their kinetic energy [And91, Moo16, Wan18].

In monolayer TMDCs, the small Bohr radius of about 1 nm implies a high probability of finding an electron and a hole within the same unit cell, leading to a radiative decay time $\tau_{\mathrm{rad}}$ of less than 1 ps based on theoretical calculations [Gla14, Pal15, Wan16a]. The most direct approach to experimentally access this decay time is based on terahertz pump-probe spectroscopy [Kai03]. For this technique, a pump pulse creates excitons in the ground state ($1s$) and a second mid-infrared pulse probes the internal transition of the exciton ($1s$–$2p$) irrespective of $K$, yielding radiative decay times $\tau_{\mathrm{rad}}$ of about 150 fs in monolayer $WSe_2$ [Poe15].
In contrast, other time-resolved measurements such as four-wave mixing [Moo15a, Dey16, Jak16] or time-resolved PL probe different quantities, such as exciton coherence time ($T_2$) or effective radiative decay time. Time-resolved PL measurements with off-resonant excitation conditions at low temperatures showed effective radiative lifetimes in the 1 – 10 ps range [Kor11, Lag14, Wan14, Wan15b] for monolayer TMDCs (see Fig. 2.9(b)) in very good agreement to calculations of the effective radiative lifetime [Pal15]. As a consequence, in experiments at room temperature, where most of the excitons are distributed outside of the light cone, the effective radiative lifetimes can extend to nanoseconds [Ama15, Kul18].

### Trions and biexcitons

Besides excitons, which are comprised of one electron and one hole, more complex many-body states such as trions or biexcitons can emerge in monolayer TMDCs, see Fig. 2.10 for a schematic depiction. In the case of trions, free charge carriers (either electrons or holes) bind to the neutral exciton and form a three-particle state in analogy to an ion in the hydrogen atom picture. Since monolayer TMDCs are predominantly n-doped [Rad11] one usually assumes the case of a negatively charged trion.
Calculations predict that the binding energy of trions amounts to about 10 % of the binding energy of the neutral exciton [Ber13, Drü17, Van17]. Experimentally, the bind-

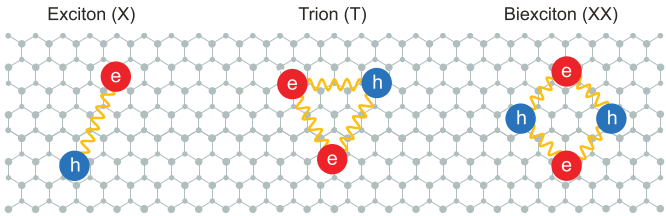


**Figure 2.10** | Schematic illustration of an exciton, trion and biexciton in real space.

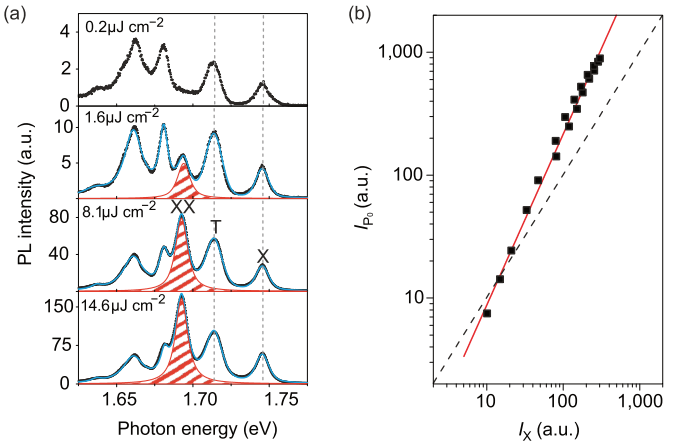


**Figure 2.11** | (a) Power-dependent spectra of monolayer $WSe_2$ at 10 K using pulsed laser excitation demonstrating the emergence of biexciton emission (XX). The dashed grey lines indicate the position of the neutral exciton (X) and the trion (T). (b) Double logarithmic representation of the biexciton intensity ($I_{P0}$) as a function of the neutral exciton intensity $I_X$. The red line is a power-law fit with $I_{P0} \sim (I_X)^\alpha$ with $\alpha = 1.39$. The black dashed line indicates a linear relation. Both figures taken from [You15] and slightly adapted.

ing energy of the trion ($E_{B,T}$) can be determined by subtracting a possible contribution of the Fermi energy ($E_F$) of the free charge carriers from the energetic separation between neutral exciton ($E_X$) and trion ($E_T$) [Mak13, Che15] with: $E_{B,T} = E_X - E_T - E_F$. Therefore, the spectral separation between exciton and trion peak represents an upper limit for the binding energy of the trion. Typical binding energies of trions in monolayer TMDCs were shown to be on the order of 30 meV for $MoS_2$ [Mak13], $MoSe_2$ [Ros13], $WS_2$ [Sha15, Ple15] and $WSe_2$ [Jon13] rendering these quasiparticles stable up to room temperature. Due to their charged nature, trions are sensitive to tunable carrier densities via electrostatic gating, which also gives access to negatively and positively charged trions in the same sample [Ros13, Wan17b, Cou17].

Biexcitons emerge when two excitons bind to form a molecule-like four-particle state. In experiments, biexcitons are observed as the dissociation of two excitons, where one of them recombines radiatively [Kli12]. A crucial hallmark of biexcitons is the superlinear emission characteristics, since the density of biexcitons generally depends quadratically on the density of excitons [Gou79, Kim94], resulting in a power law of the form $I_{XX} \sim (I_X)^\alpha$ with $\alpha = 2$ in the case of full equilibrium between the exciton and

biexciton population.

In monolayer TMDCs, biexciton emission was observed in $WSe_2$ [You15] (see Fig. 2.11), $WS_2$ [Sha15, Ple15, Sie16, Kim16, Oka17, Par17], $MoS_2$ [Sie15, Lee16] and $MoSe_2$ [Hao17a]. To reach the required high-density regime for the observation of biexcitons, experiments were either performed with a pulsed laser or high continuous-wave (CW) laser excitation powers. The parameter $\alpha$ from the power-law fit was usually found to be smaller than 2 in monolayer TMDCs (see for instance Fig. 2.11 (b)), which was attributed to a lack of full equilibrium between excitons and biexcitons. The binding energy of the biexciton corresponds to the difference of the emission of the exciton and the biexciton in the spectrum. Experiments on monolayer TMDCs showed a considerable spectrum of binding energies of the biexciton in a range from 20 meV [Hao17a] to 75 meV [Oka17], which was also present in a variety of theoretical calculations [You15, Kyl15, Zha15b, May15, Kid16, Szy17, Dan17]. The reason for this large spread could arise from inconsistent spectral attributions of the biexciton feature and the possibility of a charged biexciton complex (see chapter 5).

## 2.3 Coupled spin-valley effects in monolayer TMDCs

A considerable part of the research interest in monolayer TMDCs can be attributed to coupled spin-valley effects and the emergence of valley polarization in this class of materials [Xu14, Yu15a, Sch16]. In this context, a valley is a local minimum in the conduction band or a local maximum in the valence band. If an electron can be attributed to a specific valley in a system of two well-defined valleys, it acquires a so-called valley pseudospin. The valley pseudospin of an electron can be understood as an additional degree of freedom besides charge and spin.

In monolayer TMDCs, the optical transitions take place at the two inequivalent $K^+$ and $K^-$ points at the corners of the Brillouin zone, see Fig. 2.3(b), which represent the relevant two-valley system. As already outlined in section 2.1.2, for odd-layered 2H TMDC crystals, which have a broken inversion symmetry, the Kramers degeneracy, i.e. the energetic degeneracy of different spin states in a valley, is lifted. Therefore, a coupling of the spin- and valley degree of freedom emerges, where the spin configuration is directly linked to a certain valley. The coupling is further stabilized by the strong spin-orbit coupling in monolayer TMDCs, which leads to a sizable splitting of the valence bands. In this respect, excitonic transitions stemming from the energetically

upper (lower) valence band are denoted as A (B) excitons. The two valleys at the $K^+$ and $K^-$ points are energetically degenerate since they are linked by time-reversal symmetry. Figure 2.12 shows schematically the single-particle band structures of $MoX_2$ and $WX_2$ monolayers at the relevant K points, where the two highest valence bands and two lowest conduction bands are depicted. The splitting in $MoX_2$ compounds is assumed to be reversed with respect to $WX_2$ materials, as already discussed in section 2.1.2. Since optically allowed transitions have to be spin-conserving, the energetically lowest transition in $MoX_2$-based TMDCs is optically bright, whereas in $WX_2$-based TMDCs it is optically dark [Liu13, Kor14, Kor15, Zha15c]. Due to varying effective masses in the case of $MoX_2$ materials, the spin-split conduction bands are predicted to cross for large values of $k$, given the assumption of a constant effective mass for each conduction band respectively.

The most important consequence of the spin-valley locking in monolayer TMDCs is the possibility to selectively address and read out a valley polarization, i.e. a preferential occupation of a certain valley that was first theoretically predicted by Xiao *et al.* and Cao *et al.* [Xia12, Cao12]. Within this concept, a certain helicity of light can only couple to a specific valley, for instance $\sigma^+$ polarized light to the $K^+$ valley, as can also be seen in Fig. 2.12.

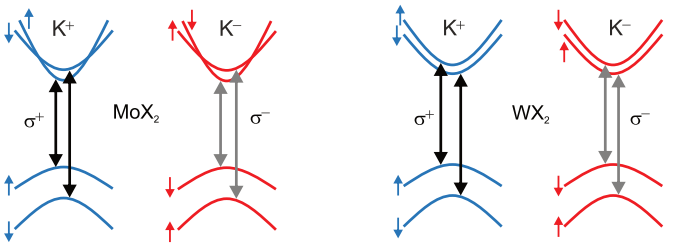


**Figure 2.12** | Schematic illustration of the band structure of monolayer $MoX_2$ and $WX_2$ TMDCs at the K points. The spin-valley locking gives rise to valley-dependent optical selection rules for circularly polarized light ($\sigma^+$, $\sigma^-$). Figure based on [Kor15].

Experimentally, the effect of valley polarization was confirmed by a variety of studies using helicity-resolved PL experiments [Mak12, Zen12, Cao12, Sal12, Jon13, Wan14]. A representative helicity-resolved PL measurement of the prototypical monolayer TMDC $WSe_2$ at a sample temperature of 4 K is shown in Fig. 2.13(a). Here, $\sigma^+$ polarized light was used to excite the sample. As can be seen, the $\sigma^+$ polarized component in emission (black line) emits stronger than the $\sigma^-$ polarized component (red line), clearly demonstrating valley polarization of the excitonic features. The overall degree

of valley polarization is defined as $P = (I_{\sigma^+} - I_{\sigma^-})/(I_{\sigma^+} + I_{\sigma^-})$, where $I_{\sigma^{+/-}}$ is the intensity of the respective polarization component of the emitted light. In steady-state PL measurements, polarization degrees close to unity have been observed [Mak12]. High degrees of valley polarization in a steady-state PL experiment do not necessarily have to result from long valley relaxation times. Instead, in a simplified picture the degree of polarization $P$ depends on the initially created polarization $P_0$, the exciton lifetime $\tau_{\mathrm{tot}}$ and the polarization decay time $\tau_{\mathrm{d}}$ via [Lag14]:

$$P = \frac{P_0}{1 + \tau_{\mathrm{tot}}/\tau_{\mathrm{d}}} \tag{2.3}$$

As already discussed in section 2.2, monolayer TMDCs usually exhibit ultra-short exciton lifetimes $\tau_{\mathrm{tot}}$ at low temperatures, mostly due to the very fast intrinsic radiative decay. Hence, high degrees of valley polarization in static PL measurements can be reached in principle even in the presence of very short polarization times $\tau_{\mathrm{d}}$. A notable exception is $MoSe_2$, where valley polarization can only be observed by exciting quasi-resonantly to the excitonic transition [Bar17b].

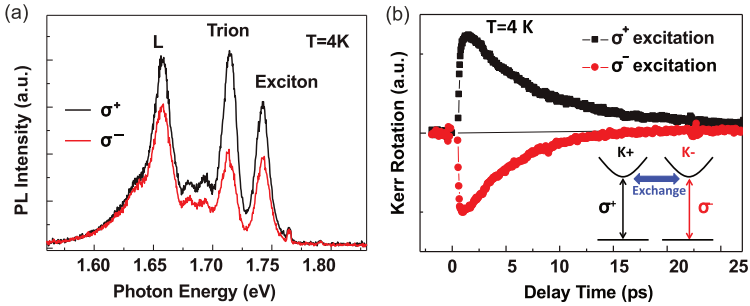


**Figure 2.13 |** (a) Helicity-resolved PL measurements of monolayer $WSe_2$ at 4 K using $\sigma^+$ polarized excitation. (b) Time-resolved Kerr rotation measurements of monolayer $WSe_2$ at 4 K. The inset depicts schematically the valley depolarization mechanism via long-range exchange interaction. Both figures taken from [Zhu14].

Direct access to the valley polarization dynamics in monolayer TMDCs is provided by helicity- and time-resolved PL measurements [Lag14] or pump-probe techniques such as time-resolved Kerr rotation [Ple14, Zhu14, Dal15, Yan17, Ple17] or helicity-resolved transient absorption spectroscopy [Mai14]. Typical values for valley depolarization times in these experiments were found to be in the picosecond range at low temperatures. Figure 2.13(b) shows time-resolved Kerr rotation measurements on monolayer $WSe_2$ at 4 K, which are sensitive to the spin-valley polarization of the absolute number

of polarized carriers [Bau94], yielding depolarization times of about 5 ps.
Based on the single-particle illustration of Fig. 2.12, the ultra-short depolarization times in monolayer TMDCs seem to be counter-intuitive at first glance, since the relaxation of initial valley polarization would require energetically unfavorable intervalley scattering with a simultaneous change of spin and momentum. However, this notion neglects the strong Coulomb interaction acting between electrons and holes giving rise to a long-range exchange interaction [Gla14, Yu14a, Yu14b]. Via this mechanism, an exciton with an electron in the $K^+$ valley can recombine and create an exciton with an electron in the $K^-$ valley, resulting in a very efficient loss of the initial polarization.

## 2.4 Breaking the valley degeneracy by external magnetic fields

As pointed out in section 2.3, the two valleys at the $K^+$ and $K^-$ points in a monolayer TMDC are linked by time-reversal symmetry resulting in an energetic degeneracy of the two optical transitions. To gain further control over the valley degree of freedom, it is therefore desirable to lift this energetic degeneracy by breaking time-reversal symmetry. This can be achieved by the application of an external magnetic field that is oriented perpendicular to the sample plane.

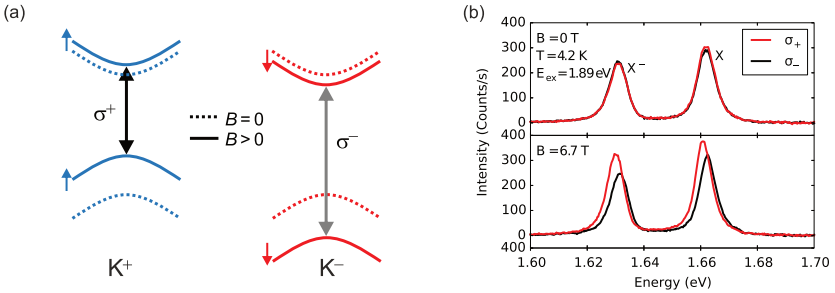


**Figure 2.14 |** (a) Breaking of the valley degeneracy in a monolayer TMDC by application of an external out-of-plane magnetic field. The energy of the transition at the $K^+$ point is lowered while it is increased at the $K^-$ point. (b) Magneto-PL measurements of monolayer $MoSe_2$ at 4 K in an out-of-plane magnetic field of 0 T and 6.7 T. Figure taken from [Mac15].

The effects of an out-of-plane magnetic field on the two valleys and the respective optical transitions are schematically depicted in Fig. 2.14(a). For a positive magnetic field ($B > 0$), the energy of the transition at the $K^+$ point decreases, whereas it increases

at the $K^-$ point. The expected effect of an external magnetic field is evidenced by experimental data of magneto-PL on monolayer TMDCs such as $MoSe_2$ as shown in Fig. 2.14(b). Here, the sample is illuminated with linearly polarized light, thereby populating both valleys equally. The PL emission from the sample, which consists of radiative recombination from excitons and trions, is subsequently analyzed in the basis of the respective $\sigma^+$ and $\sigma^-$ polarized components. In the case of $B = 0$ (upper panel of Fig. 2.14(b)), both valleys emit at the same energy since they are linked by time-reversal symmetry (see dashed line in Fig. 2.14(a)) resulting in identical emission of the two polarized components. However, for a positive out-of-plane magnetic field, the $\sigma^+$ ($\sigma^-$) component emits at a lower (higher) energy, as can be seen in the lower panel of Fig. 2.14(b). This observed energetic splitting $\Delta E$ is called valley Zeeman splitting. By using the equation

$$\Delta E = E^{\sigma^+} - E^{\sigma^-} = g\mu_B B, \tag{2.4}$$

where $E^{\sigma^\pm}$ are the emission energies of the respective polarized components, $\mu_B \approx 58$ µeV/T is the Bohr magneton and $B$ is the magnetic field one introduces a $g$ factor, which describes the susceptibility of the valley splitting to the external magnetic field. Furthermore, the lifting of the valley degeneracy can lead to a population imbalance between the two valleys and therefore to field-induced valley polarization. This is also visible in Fig. 2.14(b), where the energetically lower $\sigma^+$ component has a higher intensity than the energetically higher $\sigma^-$ component. A variety of recent magneto-PL experiments on monolayer TMDCs were able to demonstrate the emergence of a valley splitting, such as in $WSe_2$ [Aiv15, Sri15, Wan15a, Mit15], $WS_2$ [Sti16a, Ple16b, Kuh17], $MoS_2$ [Sti16a, Mit16] and $MoSe_2$ [Li14b, Mac15]. In these experiments, the observed $g$ factor was mostly found around a value of $-4$.

To understand the origin of the size and direction of the observed $g$ factor in monolayer TMDCs it is necessary to evaluate the behavior of the band structure in the vicinity of the K points in an external magnetic field. Generally, this can be achieved by an approach, where the $g$ factor is essentially determined by the three possible magnetic moments from the corresponding atomic shells, namely the spin moment, the orbital moment and the valley moment [Sri15, Aiv15]. Another theoretical access to the $g$ factor is provided by $k \cdot p$ perturbation theory, where the parametrization is found by tight-binding theory [Ryb17]. Within the course of this thesis, both approaches will be discussed in more detail to describe the behavior of interlayer excitons (chapter 4) and biexcitons (chapter 5) in an out-of-plane magnetic field respectively.

## 2.5 Van der Waals heterostructures

### General concept

Two-dimensional crystals usually have no dangling bonds and are therefore fully chemically saturated at the surface. The resulting weak forces acting between individual layers of van der Waals crystals enable the isolation and subsequent deterministic fabrication of heterostructures by a variety of experimental techniques. This concept of creating atomically thin, so-called van der Waals heterostructures [Gei13, Nov16], results in a large parameter space, where materials of varying functionalities can be easily integrated into one structure. As illustrated in Fig. 2.15, the choice of materials ranges nowadays from insulators such as hexagonal boron nitride over semimetals like graphene to semiconductors like the TMDCs. More recently, atomically thin superconductors such as $NbSe_2$ [Uge16] and two-dimensional ferromagnets [Gon17, Hua17] were successfully isolated and added to the library of available building blocks. The possibility of heterogeneous integration therefore creates hybrid systems, which promise novel physics and devices at the atomically thin limit.

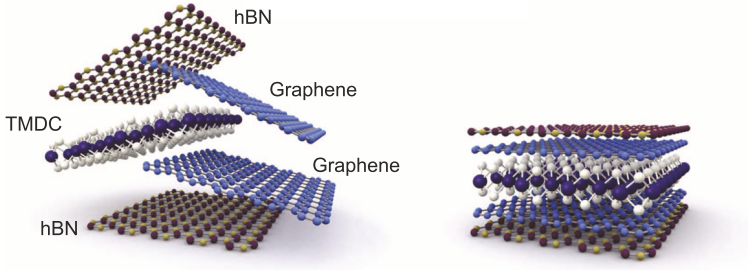


**Figure 2.15 |** Schematic illustration of a van der Waals heterostructure, where atomically thin crystals with different functionalities are combined within one structure. Figure taken from [Nov16] and slightly adapted.

The assembly of van der Waals heterostructures is considerably facilitated by the fact that the stacking of individual monolayers on top of each other is not restricted by crystal lattice matching conditions. This stands in marked contrast to epitaxially grown heterostructures such as GaAs or AlGaAs, where lattice matching at the interface is required. Furthermore, the twist angle between individual atomic layers arises as a novel degree of freedom in van der Waals heterostructures, which is not accessible in epitaxial systems.

### Fabrication and interfaces

Experimentally, van der Waals heterostructures are usually fabricated by handcraft using mechanical transfer approaches in combination with an optical microscope, where individual layers are stacked subsequently on top of each other [Dea10, Zom11, Wan13]. The heterostructures for this thesis were produced using the PDMS-based approach developed by Castellanos-Gomez *et al.* [CG14], which will be explained in more detail in section 3.2. For a summary of the different mechanical assembly techniques for van der Waals heterostructures, see [Fri18b]. Recently, the first fully automated assembly of van der Waals heterostructures consisting of up to 29 individual layers by means of a robot was reported [Mas18].
Even though van der Waals heterostructures are usually fabricated under ambient conditions, the interfaces between individual monolayers can be atomically sharp on a microscopic scale [Hai12]. This is demonstrated in Fig. 2.16, which shows a cross-sectional scanning tunneling electron microscopy (STEM) image of a heterostructure consisting of graphene and hBN.

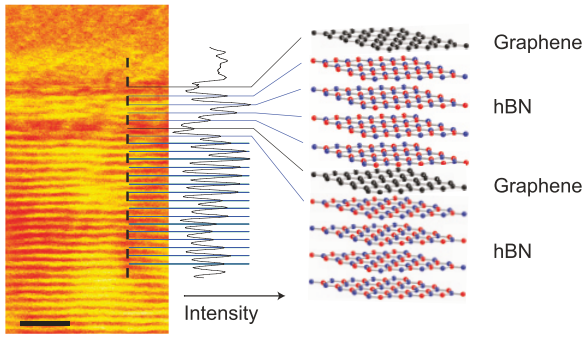


**Figure 2.16 |** Cross-sectional STEM image from a graphene/hBN heterostructure and averaged line scan of the intensity along the dashed black line, the scale bar is 2 nm. Figure taken from [Hai12] and slightly adapted.

Generally, it is assumed that adsorbates on the surface segregate into isolated pockets leading to the formation of pronounced bubbles and wrinkles. Current approaches to overcome these effects and to obtain atomically flat heterostructures on a large lateral scale include the fabrication in an inert atmosphere [Cao15], deterministic flattening of the structure by an AFM tip [Ros18] or thermal annealing (see chapter 4).

### Optoelectronic devices based on van der Waals heterostructures

The large variety of 2D materials combined with their high processability provides promising perspectives for engineering optoelectronic devices based on van der Waals heterostructures. In this respect, atomically thin TMDCs are particularly attractive building blocks due to their semiconducting behavior. Sparked by the first realization of a transistor with a monolayer TMDC as the conducting channel [Rad11], a plethora of optoelectronic devices has been realized in the ultimate thickness limit.
In two pioneering proof-of-principle works, the semiconducting properties of a TMDC were combined with ultra-thin graphene electrodes to fabricate a highly efficient photodetector [Yu13, Bri13]. Electron-hole pairs were initially created in the TMDC by an external light source and detected by transparent graphene electrodes as a photocurrent (see Fig. 2.17(a)).

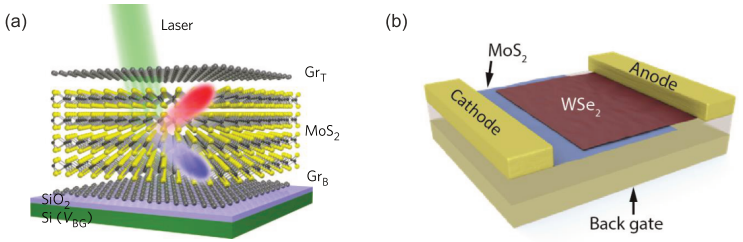


**Figure 2.17 |** (a) Schematic depiction of a photocurrent device consisting of multilayer $MoS_2$ sandwiched between monolayer graphene electrodes. Electrons (red) and holes (blue) are separated by the graphene electrodes leading to a photocurrent. Figure taken from [Yu13]. (b) Drawing of an atomically thin solar cell device consisting of a monolayer $WSe_2$ and $MoS_2$. Figure taken from [Fur14].

Moreover, the p-n-junction as the most fundamental constituent of optoelectronics was realized by different approaches involving 2D materials. The first demonstration of such a junction consisting of two monolayer TMDCs was shown by Lee *et al.* [Lee14], where two monolayer TMDCs ($MoS_2$ and $WSe_2$) with n- and p-doping respectively were stacked upon each other in a vertical van der Waals heterostructure. A schematic depiction of such a structure is shown in Fig. 2.17(b). Following studies confirmed this concept over the course of the last years with successful experimental demonstrations of photodetectors [Mas15, Lon16], solar cells [Fur14, LS14] and LEDs [Che14a, Wit15]. For a comprehensive treatment of optoelectronic devices based on van der Waals heterostructures see: [Fio14, Zha16, Pos16, Fri18a].

### Interlayer excitons in van der Waals heterostructures

Van der Waals heterostructures consisting of TMDCs can also give rise to the emergence of a novel excitonic complex, called an interlayer exciton (IEX), that is inaccessible in monolayer TMDC systems. To understand the behavior of charge complexes in the framework of a vertical heterostructure one has to take into account the band alignment of the two individual semiconductors, which can be provided by the so-called Anderson rule [Dav09]. Within this approximation, it is assumed that the electronic states between the different materials do not hybridize but can be derived from a consideration of the individual band edges. Following this rule the band edges of the conduction and valence bands of two semiconductors align according to their electron affinity $\chi$ and their bandgap. The electron affinity $\chi$ of a semiconductor is defined as the required energy to add an electron that is situated far away from the semiconductor to the crystal. The offset of the conduction bands $\Delta E_\mathrm{C}$ of two semiconductors A and B that constitute a vertical heterostructure then follows from the difference of their respective electron affinity $\Delta E_\mathrm{C} = \chi_\mathrm{A} - \chi_\mathrm{B}$. The offset of the valence bands is given by the bandgaps of the two semiconductors. Depending on the combination of electron affinity and band gaps of two semiconductors, three different types of band alignments result according to the Anderson rule, which are depicted in Fig. 2.18.

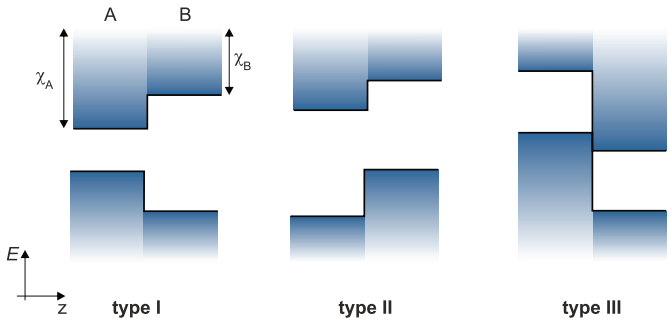


**Figure 2.18** | Band offset of two different semiconductors A and B according to the Anderson rule. Depending on the electron affinity $\chi_\mathrm{A}$ and $\chi_\mathrm{B}$ and the energetic edges of conduction band and valence band, three different types of band alignments emerge: type I, type II and type III.

In a type I structure, the conduction band of semiconductor A is energetically lower and the valence band energetically higher than for semiconductor B or vice versa. Type II band alignment is characterized by a situation, where the energetically favorable band extrema are located in different semiconductors. In Type III structures, the conduction

band of one semiconductor is energetically lower than the valence band maximum of the other.

Recent theoretical [Liu15, Lat17] and experimental works [Chi15, Hil16, Job16, Wil17] have shown that the Anderson rule is largely applicable for heterostructures consisting of monolayer TMDCs. At the K points, where the optical transitions usually take place, the coupling between the layers is weak compared to the energy mismatch resulting in a vanishing hybridization between the layers. Moreover it was predicted that vertical heterostructures between two different monolayer TMDCs show a type II band alignment within the concept of the Anderson rule [Kom13, Lia13, Ter13, Özç16].

As will be discussed in the following, this energetic configuration can give rise to the formation of interlayer excitons. Figure 2.19(a) schematically illustrates the energetic situation of a vertical TMDC heterostructure with two different TMDCs, where the bands have a type II alignment.

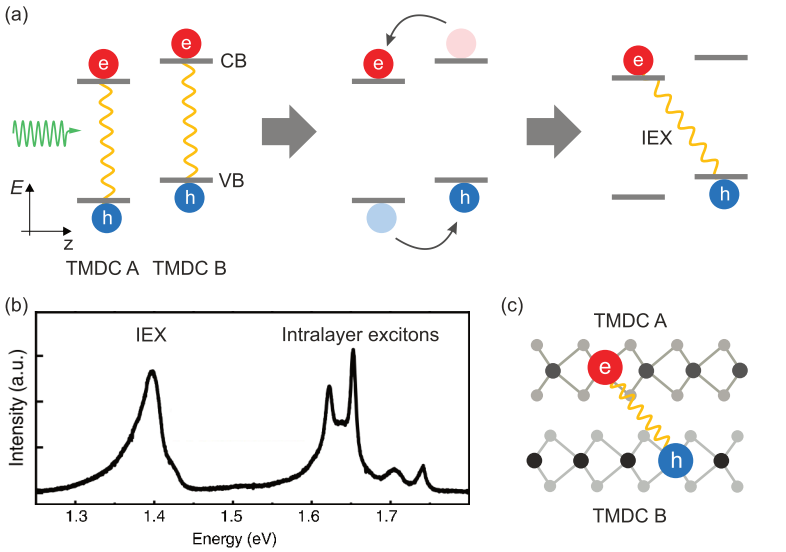


**Figure 2.19** | (a) Interlayer excitons in a type II TMDC heterostructure. First, electron-hole pairs are optically excited in the individual monolayers TMDC A/B. Subsequent charge transfer leads to a spatial separation of electrons and holes. Finally, the interlayer exciton is formed across the heterojunction. (b) PL spectrum of a $WSe_2/MoSe_2$ heterostructure at 4 K. Besides the emission from the individual monolayers (intralayer excitons) the energetically lowered interlayer exciton is visible. Figure taken from [Riv15]. (c) Schematic real space depiction of an interlayer exciton between two different TMDCs.

By optically exciting the heterostructure, electron-hole pairs are initially created in the respective monolayers. However, due to the type II band alignment it is favorable for holes in TMDC A and electrons in TMDC B to undergo a charge transfer, which was shown to occur on ultra-fast timescales in the sub-picosecond regime by using pump-probe experiments [Hon14, Ceb14, Pen16] and corroborated by theoretical considerations [Li17]. This also leads to a considerable quenching of the PL intensity from the individual monolayers of the heterostructure. Following this process, the electron-hole pairs are formed across the two different TMDCs, where electrons reside in TMDC A and holes in TMDC B giving rise to interlayer excitons. A schematic real space depiction of an interlayer exciton across two different TMDCs is given in Fig. 2.19(c).

From a fundamental point of view, interlayer excitons possess novel physical properties that are not accessible in bare monolayer excitonic systems. The separation of electrons and holes into two different layers gives rise to a permanent dipole moment oriented perpendicularly to the plane of the heterostructures. Hence, interlayer excitons are in principle sensitive to a manipulation by an external electric field along the axis of the dipole [Unu18]. The increased average distance of electrons and holes in the case of interlayer excitons also directly affects the radiative dynamics. Since the intrinsic radiative lifetime depends on the separation of electrons and holes, interlayer excitons are expected to show much longer lifetimes in comparison to excitons in monolayer systems.

Experimentally, interlayer excitons in TMDC heterostructures have been first observed in $WSe_2/MoS_2$ [Fan14] and $WSe_2/MoSe_2$ [Riv15] heterostructures. Figure 2.19(b) shows a representative PL spectrum on a $WSe_2/MoSe_2$ heterostructure taken from Rivera *et al.* [Riv15] at a sample temperature of 4 K. The recombination of intralayer excitons from the individual monolayers at the right side of the spectrum is strongly quenched due to the ultra-fast charge transfer but still discernible. At around 1.4 eV, the emission from the interlayer exciton is visible, which is spectrally separated from the intralayer emission. Following the above mentioned two pioneering works, signatures of interlayer excitons have been observed also in other material combinations based on monolayer TMDCs such as $MoS_2/WS_2$ [Ton14, Hil16], $MoSe_2/WS_2$ [Ceb15], $MoS_2/MoSe_2$ [Mou17] or $MoS_2/MoSe_2/MoS_2$ [Bar17a].

Chapter 3

# Experimental methods

## 3.1 Photoluminescence spectroscopy

### 3.1.1 Experimental setup

The setup used for performing PL measurements during the course of this thesis in Regensburg is schematically depicted in Fig. 3.1. It enables measurements with high spatial precision in the µm regime and at low temperatures down to 4 K.

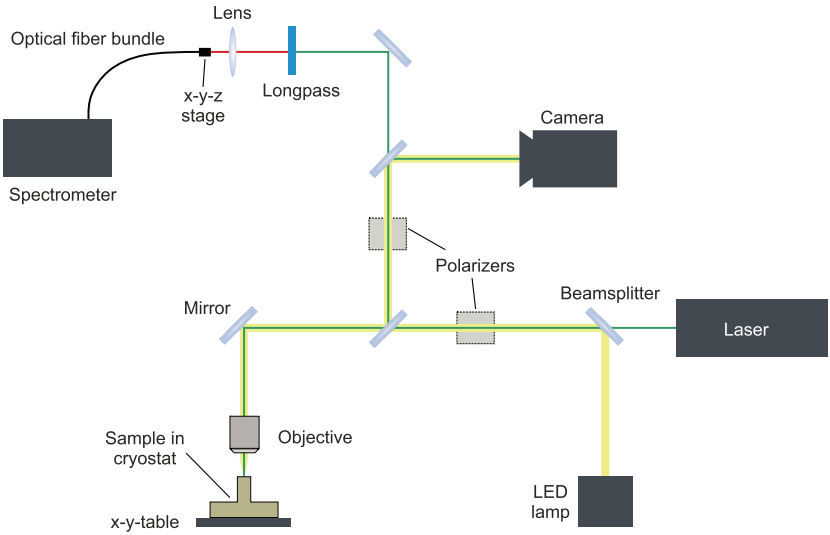


**Figure 3.1** | Schematic illustration of the optical setup for PL measurements.

A diode-pumped frequency-doubled continuous-wave laser with a wavelength of 561 nm or 532 nm is used as an excitation source. The laser light is guided via beamsplitters and a mirror through a long-working distance 100x objective (Nikon L Plan SLWD, NA 0.7) onto the sample. The spatial resolution of the setup, which is determined by the full width at half maximum (FWHM) of the spot size of the laser, amounts to about 1 µm. The sample is situated on an x-y-table driven by linear motors with a step size of about 100 nm. Optionally, for low-temperature measurements, the sample can be placed on the cold finger of a continuous-flow cryostat (CryoVac KONTI), which can be cooled down to 4 K by liquid helium. After interacting with the sample, the scattered signal together with the reflected laser light is guided through beamsplitters to a longpass filter, which filters out the scattered laser light. The remaining signal from the sample is focused via a lens of short focal length onto the entrance of an optical fiber bundle, which guides the light to the entrance of a spectrometer. The overall signal yield can be adjusted and improved by optimizing the position of the optical fiber bundle, which is fixed to an x-y-z-stage. The spectrometer (Princeton Instruments Acton SP2750) is equipped with three different diffraction gratings (150, 600 and 1800 lines/mm), which spectrally disperse the light onto a Peltier-cooled CCD chip. For PL measurements, a 150 lines/mm grating is mostly used due to the larger detectable energy range. For most experiments, an image of the relative position of the laser spot on the studied sample is required. Therefore, the white light of an LED lamp is guided through the same path as the laser and imaged onto a camera after being reflected by the sample. The resulting image on the camera can then be used for finding the respective sample position.

Measurements of valley polarization require the excitation of the sample via circularly polarized light and subsequent detection of the emitted signal in a circular basis. The additional optical elements for this experiment are indicated in Fig. 3.1 and can be placed optionally into the beam path. The beam emitted from the laser is first circularly polarized by a combination of a linear polarizer and a subsequent quarter-wave plate with a relative angle of $\pm 45°$. Guiding the emitted light from the sample through another quarter-wave plate and linear polarizer enables helicity-resolved measurements.

Spatial PL maps can be realized by scanning the sample with the x-y-table. For this, a predefined area is automatically scanned in defined step sizes employing a LabView software, where a PL spectrum at each measurement point is recorded. Using another LabView program, the recorded spectra are automatically fitted with a Gaussian fit function, which allows for the extraction of the total intensity, the spectral position and the FWHM for each data point of the PL map.

### 3.1.2 Magneto-PL at the HFML in Nijmegen

A substantial part of the experimental data presented in this thesis result from magneto-PL measurements on van der Waals heterostructures. These data were all collected at the High Field Magnetic Laboratory (HFML) in Nijmegen (The Netherlands), which is a user facility within the framework of the European Magnetic Field Laboratory. The setup in Nijmegen offers the possibility to conduct PL measurements in out-of-plane magnetic fields up to 30 T. The experimental setup is realized within two floors: The ground floor with the magnet chamber and the first floor, where most of the optical components are placed.

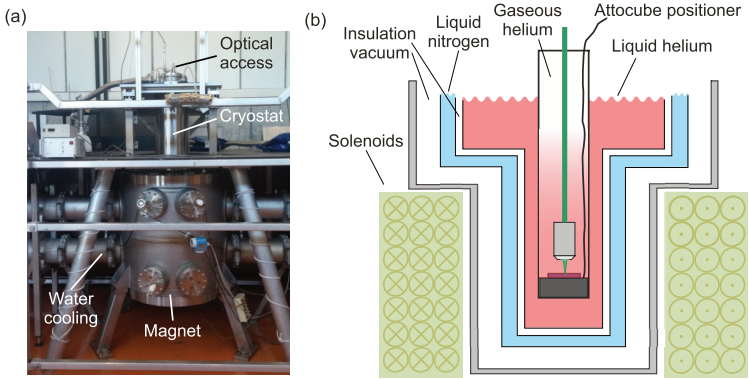


**Figure 3.2** | (a) Picture of the magnet facility (ground floor) at the HFML in Nijmegen, where all magneto-PL experiments presented in this thesis were performed. The temperature of the resistive 30 T magnet is regulated by an internal water cooling system. The upper part of the optical cryostat, which is placed within the magnet, is also visible. The laser beam from the optical setup upstairs enters the cryostat by the indicated optical access. (b) Schematic cross-section of the cryostat system at the HFML for optical measurements. Figure taken from [Ple16a] and slightly adapted.

Magnetic fields up to 30 T are realized by the construction of resistive magnets in the form of a so-called Bitter coil. Such a Bitter magnet is based on current-carrying conducting copper plates of circular shape and insulating spacer material arranged in a helical configuration [Her03]. The most crucial factor for reaching high fields is an efficient cooling system of the magnet since the applied currents of up to 20 kA lead to a significant heat loss. The cooling is realized by an internal water cooling system at the HFML by which the water is pumped in perpendicular direction through small openings in the Bitter magnet with a maximum flow of 140 liters/s. Nevertheless,

fields higher than 25 T can only be kept for a duration of about 10 – 15 minutes due to possible overheating of the system. The overall power consumption of the magnet system at the highest fields amounts to about 20 MW.
To perform the experiments at low temperatures, the sample is placed into a bath cryostat as it is shown in Fig. 3.2(b). The lower part of this cryostat, where the optical excitation takes place, is fitted into the bore of the magnet, which has a diameter of 50 mm. Within the bath cryostat, an outer chamber with liquid nitrogen surrounds the inner chamber filled with liquid helium, which are both separated by insulating vacuum. The sample itself is situated in a tube filled with gaseous helium serving as an exchange gas. An x-y-z system consisting of three attocube positioners placed on top of each other allows for positioning the sample with high precision.
In the upper floor, a similar optical setup compared to the one presented in section 3.1.1 and Fig. 3.1 is employed. Continuous-wave laser sources of different wavelengths (e.g. 532 nm, 561 nm or 640 nm) are available and can be coupled into the optical path. The beam is aligned through a hole in the ceiling between upper and lower floor over a distance of 5 m into the optical window of the cryostat (see Fig. 3.2(a)). Inside the tube of the cryostat the laser is focused onto the sample by a 40x objective to a spot size of about 4 µm. The scattered light from the sample is emitted back to the upper floor, where it is guided through a non-polarizing beam splitter, a longpass and subsequent lens into a spectrometer, in analogy to section 3.1.1. The spectrometer in Nijmegen offers three different diffraction gratings (300, 600 and 1200 lines/mm) depending on the required resolution and the CCD chip is cooled with liquid nitrogen.
Optionally it is also possible to carry out time-resolved magneto-PL measurements at the HFML facility. For this, the CW-laser is replaced by a pulsed diode laser with a pulse length of 80 ps and a wavelength of 690 nm, which is synchronized to an avalanche photodiode (APD). The PL signal emitted from the sample by using this excitation is filtered by a bandpass filter and the APD is employed to detect the PL intensity as a function of time.
Unlike the PL setup used in Regensburg, no direct imaging of the sample via a white-light source combined with a camera system is available in Nijmegen rendering the positioning on the sample with respect to the laser beam far more intricate. Nevertheless, it is possible to find the sample by imaging the scattered light of a Helium-Neon laser, which is reflected on the substrate, onto a wall. Thereby, the scattered light of the gold markers and the respective numbers on the substrate enable the orientation. This procedure takes place before the sample is mounted into the helium gas tube.

### 3.1.3 Streak camera system

Time-resolved PL measurements in Regensburg are carried out by using a streak camera in combination with a pulsed laser system. In principle, this setup is similar to the PL setup of section 3.1.1, apart from the laser source and the detection scheme. Short light pulses are provided by a FemtoFiberPro T-Vis (TOPTICA) fiber laser with a repetition rate of 80 MHz. In this system, an Erbium-doped fiber serves as the active medium, which is pumped by diodes. Short pulses in the femtosecond regime are initially created by passive mode-locking using a saturable absorber mirror within an oscillator. Subsequently, the pulses are transformed into a supercontinuum through a non-linear fiber and frequency doubled via second harmonic generation in a non-linear crystal. The angle of this crystal can be adjusted manually for tuning the wavelength range of the laser from 490 nm to 700 nm. The resulting pulses have a duration of about 200 fs and the maximum output power lies between 3 – 9 mW, depending on the wavelength.

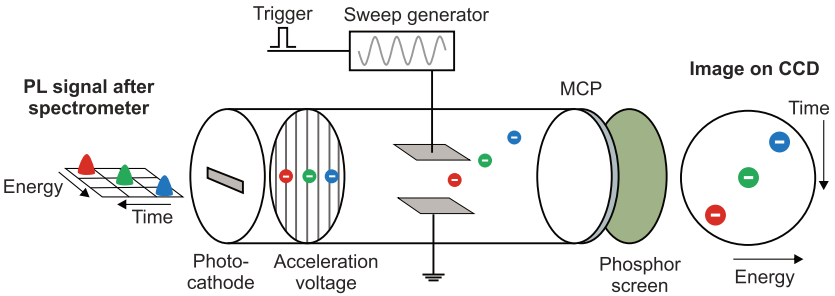


**Figure 3.3** | Operation principle of a streak camera system as described in the main text.

Due to the pronounced spectral sidelines of the resulting pulses, the laser first needs to be filtered by a bandpass of the desired wavelength, in order to perform PL experiments. In analogy to Fig. 3.1, the beam is then coupled into a 100x objective and focused onto the sample, which can be placed in a cryostat for measurements at low temperatures. The reflected PL signal is guided into a spectrometer and spectrally dispersed by a grating with 300 lines/mm. Now, the photons of the PL signal having a certain energy and a specific time delay with respect to the interaction of the excitation pulse with the sample enter the streak camera (Hamamatsu C5680) by a horizontal opening slit (see left side of Fig. 3.3). These photons hit a photocathode, which leads to the emission of electrons based on the photoelectric effect. The spatial and temporal distribution of

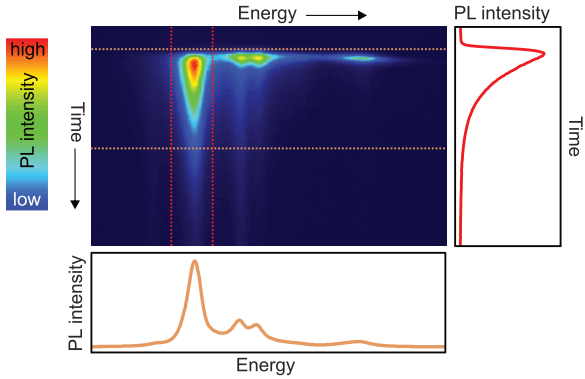


**Figure 3.4** | Example of a time-resolved PL image acquired with a streak camera. The sample under study is an hBN-encapsulated monolayer $WS_2$ measured at 4 K. The spectrum and the transient are extracted by integration of the indicated intervals.

the emitted electrons is highly correlated to the initial order of the photons due to the quasi-instantaneous nature of the photoelectric effect. The electrons are subsequently accelerated by an electric field and deflected by two horizontally aligned capacitor plates. Importantly, the oscillating deflecting voltage of sinusoidal shape is locked to the repetition rate of the laser (80 MHz) by electrical synchronization resulting in an oscillation period of 12.5 ns (so-called synchro-scan mode). Being triggered in the quasi-linear regime of the sinusoidal voltage, the electrons are deflected vertically with respect to their initial interaction time with the photocathode. The following multi-channel plate (MCP, see Fig. 3.3) serves as a secondary electron multiplier to optionally amplify the signal strength (gain). Finally, the electrons are converted back to photons by a phosphor screen and detected with a CCD camera. The vertical position of the signal on the CCD chip therefore directly corresponds to the initial temporal distribution of the photons, while the spectral information is resolved on the horizontal axis. A prototypical PL image obtained from the streak camera system is shown in Fig. 3.4.

The time resolution of the streak camera system is mainly determined by the amplitude of the deflection voltage. Depending on the selected time frame of the trigger signal, the resolution ranges from 2 ps (time range 1) to 11 ps (time range 4) corresponding to an available time window for the detection of 200 ps (time range 1) to 2.1 ns (time range 4). However, due to technical problems related to the triggering of the signal, only time range 2 – 4 were accessible for measurements during this thesis.

## 3.2 Sample fabrication

The weak van der Waals forces acting between the individual layers of a TMDC crystal (see section 2.1.1) enable the mechanical exfoliation down to the atomically thin limit. This concept was first demonstrated by the isolation of monolayer graphene [Nov04] and subsequently expanded to other layered crystals such as $MoS_2$ or $NbSe_2$ [Nov05b], which were successfully thinned down to a monolayer. For the present work, bulk crystals of different commercial sources were used as the starting material for exfoliation. The TMDCs studied during this thesis, $MoSe_2$, $WSe_2$ and $WS_2$ are based on artificial growth and the bulk crystals were purchased either from HQ Graphene (The Netherlands) or 2D Semiconductors Inc. (USA).

The original method for mechanical exfoliation is called Scotch-tape technique, where a bulk crystal is repeatedly cleaved using Scotch magic tape and subsequently pressed onto a substrate. With a certain chance, a flake with monolayer thickness can then be found on an arbitrary position. While the Scotch-tape technique is easy to learn and only requires a minimum amount of resources, it also comes with specific drawbacks. On the one hand, the producible monolayers applying this method are generally rather small ($\leq 100\,\mu m^2$). On the other hand and even more crucial for this thesis, the position where the flakes remain on the substrate cannot be controlled, rendering the deterministic fabrication of vertically stacked heterostructures virtually impossible.

To overcome these limitations, a modified exfoliation method was applied to fabricate samples during this thesis, which is called Polydimethylsiloxane (PDMS)-transfer and was proposed by Castellanos-Gomez *et al.* [CG14]. The general approach of this technique is schematically depicted in Fig. 3.5 and will be outlined in more detail in the following. First, a small piece of a transparent and viscoelastic PDMS film (GelFilm WF-20-X4, height 0.6 mm) is placed on a microscope slide, serving as a temporary substrate for the exfoliation. The cleaving of the bulk crystals is performed with a tape of lower adhesive force than Scotch-tape namely Nitto-tape (Nitto Denko Co., SPV 224P). After the exfoliated crystals have been put on the PDMS substrate, an optical microscope with a 10x objective is used to inspect the substrate for monolayer flakes of interest. This is facilitated by the high optical contrast of monolayer flakes, which enables their direct identification with the naked eye through the microscope (Fig. 3.5(a)). After a suitable flake has been found, the microscope slide is turned upside-down and mounted onto a x-y-z stage (Fig. 3.5(b)). From now on, the procedure takes place under an optical microscope with a 10x objective. A substrate of choice is fixed on a rotatable stage with double-sided tape. The x-y-z stage with the PDMS stamp is

now lowered onto the substrate and finally brought into direct contact (Fig. 3.5(c)). Afterwards, the PDMS film is slowly (5 – 15 min) released by using the z-component of the stage resulting in a mostly successful transfer (success rate ≈ 70 – 90 %) of the flake from the PDMS film to the substrate.

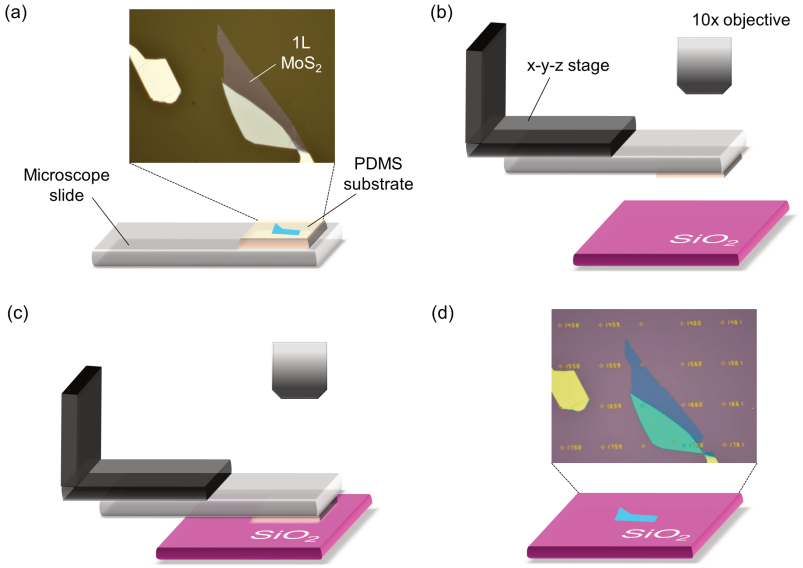


**Figure 3.5 |** Exfoliation and deterministic transfer of monolayer TMDCs using the PDMS transfer technique. (a) Using Nitto-tape, a monolayer TMDC is exfoliated onto a PDMS substrate, which itself sticks to a microscope slide. (b) The microscope slide is clamped into an x-y-z stage and positioned below the 10x objective of an optical microscope. (c) The flake is brought into contact with the $SiO_2$ substrate. (d) After slowly releasing the PDMS film, the monolayer TMDC remains on the substrate.

The working principle of this transfer method is based on the viscoelasticity of the PDMS film [Mei06, Fen07]. On short timescales, for instance during the exfoliation process, the film can be considered as an elastic solid. However, on long timescales it behaves like a liquid. Hence, during the slow lift-off of the PDMS, the TMDC flake experiences a lower adhesion force and therefore remains on the substrate.
The substrates used during the course of this thesis were 4.5 mm x 4.5 mm sized pieces of a $p^{++}$-doped silicon wafer with a capping layer of $SiO_2$ with a height of 285 nm. In analogy to the case of graphene [Bla07], the optical contrast of monolayer TMDCs is strongly enhanced by interference effects stemming from the specifically chosen height

of the $SiO_2$ layer [CG10]. Furthermore, a coordinate system on the substrate consisting of gold numbers and periodic crosses with lateral dimensions of 5 µm fabricated by optical lithography greatly facilitate the orientation (see Fig. 3.5(d)).
In contrast to the Scotch-tape technique, the PDMS transfer is highly suitable for the fabrication of vertical van der Waals heterostructures. Due to the high lateral positioning accuracy in the micrometer range, it is possible to deterministically stack several flakes on top of each other by repeating the transfer process. Examples of successfully produced heterostructures will be presented in chapter 4 and 5. Moreover, the mechanical exfoliation on the PDMS substrate employing Nitto-tape empirically results in larger monolayer flakes compared to the Scotch-tape technique.
By steadily optimizing the exfoliation process and simultaneously paying special attention to the surface quality of the cleaved crystals, ultra-large monolayers with lateral dimensions of around 50,000 µm$^2$ could be fabricated during this thesis. Examples are shown in Fig. 3.6, which represent arguably some of the largest samples worldwide produced by mechanical exfoliation based on the published literature at the present time.

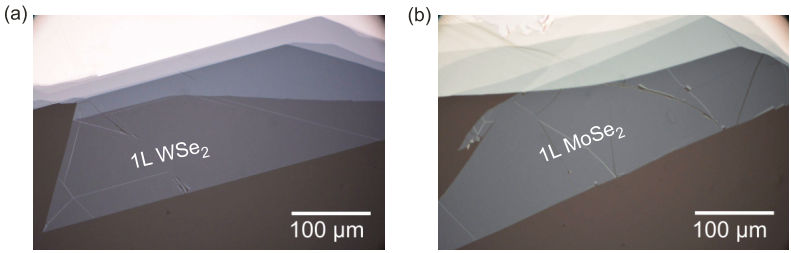


**Figure 3.6** | Examples of ultra-large monolayer flakes of (a) $WSe_2$ and (b) $MoSe_2$ on a PDMS substrate.

Samples of this extended lateral dimensions are a crucial requirement for optical experiments with a very large laser spot size and were provided within multiple collaborative efforts during this thesis [Poe15, Hao16, Lan16, Hao17a, Hao17b, Ste17, Lan18, Ste18]. Such conditions usually occur in experiments in the terahertz regime or in setups, where no magnification objective can be integrated for technical reasons.

Chapter 4

# Interlayer excitons in a two-dimensional heterostructure

## 4.1 Introduction

In this chapter, the remarkable physical properties of interlayer excitons arising from an atomically thin van der Waals heterostructure will be studied in detail. As discussed in section 2.5, experimental signatures of interlayer excitons have been observed for a variety of TMDC heterobilayer combinations. Within the course of this thesis, the focus will be put on the $WSe_2/MoSe_2$ system. Previous experimental results by Rivera *et al.* [Riv15, Riv16] demonstrated that the IEX PL in a $WSe_2/MoSe_2$ heterostructure is spectrally well-separated from the emission peaks of the excitons from the individual monolayer constituents (see Fig. 2.19), rendering this material combination especially appealing from a spectroscopic point of view.

While it is well established that the optical transitions in monolayer TMDCs take place at the respective K points of the conduction and valence band, the situation is less straightforward in the case of interlayer excitons. Therefore, we need to consider the configuration of interlayer excitons in momentum space in a $WSe_2/MoSe_2$ heterostructure. Recently, it was shown for instance that interlayer excitons in a $WSe_2/MoS_2$ heterostructure are formed through holes at the $\Gamma$ point and electrons at the K point and are therefore indirect in momentum space [Kun18]. However, in the case of interlayer excitons of a $WSe_2/MoSe_2$ structure, as studied here, experimental evidence suggests that the optical transitions result from electrons and holes at the K points of the constituent materials [Nay17]. Consequently, particular attention has to be payed to the twist angle of the heterostructure, as outlined in Fig. 4.1(a).

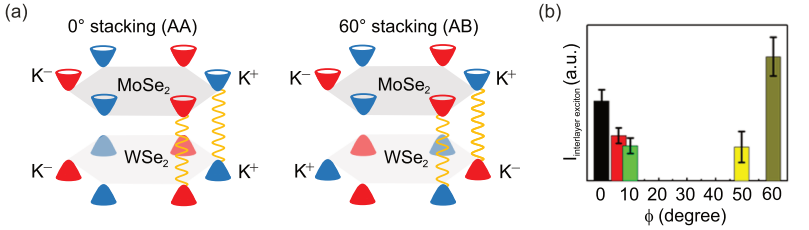


**Figure 4.1 |** (a) Schematic momentum space arrangement of the conduction and valence bands in a $WSe_2/MoSe_2$ heterostructure for 0° (AA stacking) and 60° (AB stacking) twist angle, where the optical transitions take place at the K points of the Brillouin zone. (b) PL intensity of interlayer excitons at room temperature in a $WSe_2/MoSe_2$ heterostructure as a function of the twist angle $\phi$ of the two monolayer materials. Figure taken from [Nay17] and slightly adapted.

Interlayer excitons in a $WSe_2/MoSe_2$ heterostructure stem from electrons of the conduction band in $MoSe_2$ and holes of the valence band in $WSe_2$. Assuming recombination at the K points, efficient radiative emission of interlayer excitons can only be expected for vanishing momentum mismatch between electrons and holes, which is fulfilled for stacking angles close to 0° (AA stacking) and 60° (AB stacking). This hypothesis was recently confirmed by a twist-angle dependent PL study on $WSe_2/MoSe_2$ heterostructures by Nayak *et al.* [Nay17], where PL from the interlayer exciton was only observable for stacking angles close to 0° and 60°, see Fig. 4.1(b). Importantly, a peculiar situation arises for an AB stacking of the heterostructure since in this case, optically allowed transitions occur between valleys of different index, in stark contrast to the scenario of monolayer systems.

Using an AB-stacked $WSe_2/MoSe_2$ heterostructure as a testbed, we will focus on two main aspects of interlayer exciton physics in the following. First, by employing steady-state and time-resolved PL measurements, we shed light on interaction effects and the dynamics of this novel excitonic species. The arising phenomena differ drastically from typical observations in monolayer systems and are direct evidence for the permanent dipole moment and the ultra-long lifetime of interlayer excitons. Second, probing interlayer excitons under the influence of a high magnetic field will provide crucial insights on the intricate valley physics of this system. The impact of the inter-valley transitions in our AB-stacked structure is directly visible in a strongly enhanced $g$ factor, giving rise to near-unity valley polarization of interlayer excitons at high magnetic fields. This part of the work has been published in [Nag17a] and [Nag17b].

## 4.2 Sample structure and fundamental optical properties

We start with a thorough principal characterization of the heterostructure under study. After fabrication, the $WSe_2/MoSe_2$ heterostructure is analyzed by PL spectroscopy at low temperatures. We observe the emergence of spectrally narrow and well-defined emission from interlayer excitons, which is further corroborated by photoluminescence excitation spectroscopy. Helicity-resolved PL measurements show pronounced valley polarization of the interlayer exciton that can be enhanced by quasi-resonant excitation.

### 4.2.1 Fabrication of a two-dimensional heterostructure

In the following, the fabrication of the $WSe_2/MoSe_2$ heterostructure using the approach discussed in section 3.2 will be presented. All experimental data in chapter 4 on interlayer excitons were obtained using this sample. Figure 4.2 shows the step-by-step procedure, which was performed under ambient conditions.
First, using Nitto-tape and a bulk $MoSe_2$ crystal from HQ graphene, a monolayer of $MoSe_2$ with a well-defined crystallographic axis is mechanically exfoliated on the PDMS film (see Fig. 4.2(a)). Using the PDMS-transfer technique, the monolayer is subsequently placed on the $SiO_2$ substrate as shown in Fig. 4.2(b). Now, the upper layer of the heterostructure, monolayer $WSe_2$ (Fig. 4.2(c)), which also has a recognizable crystallographic axis is mechanically exfoliated using bulk $WSe_2$ crystals from HQ graphene. In the final step, the $WSe_2$ monolayer is placed deterministically on top of the $MoSe_2$ monolayer. During the last transfer step, special care is taken to ensure a crystallographic alignment of the two monolayers, which is achieved by using the rotating stage of the transfer setup. Figure 4.2(d) shows the resulting vertical $WSe_2/MoSe_2$ heterostructure, where the white-framed area indicates the region of vertical overlap between monolayer $MoSe_2$ and $WSe_2$. It should be noted that the individual monolayers were not fully transferred, as can be seen for the case of monolayer $WSe_2$ (Fig. 4.2(b),(d)), where some parts of the flake did not remain on the $SiO_2$ substrate. However, in the region of the $WSe_2/MoSe_2$ heterostructure, the two materials have a continuous overlap.
In order to observe emission from interlayer excitons, a sufficient electronic interlayer coupling within the heterostructure is essential. However, due to the ambient fabrication conditions, a layer of undesirable adsorbates between the vertically stacked monolayers can occur, acting as an additional spacer. The detrimental effects of such a

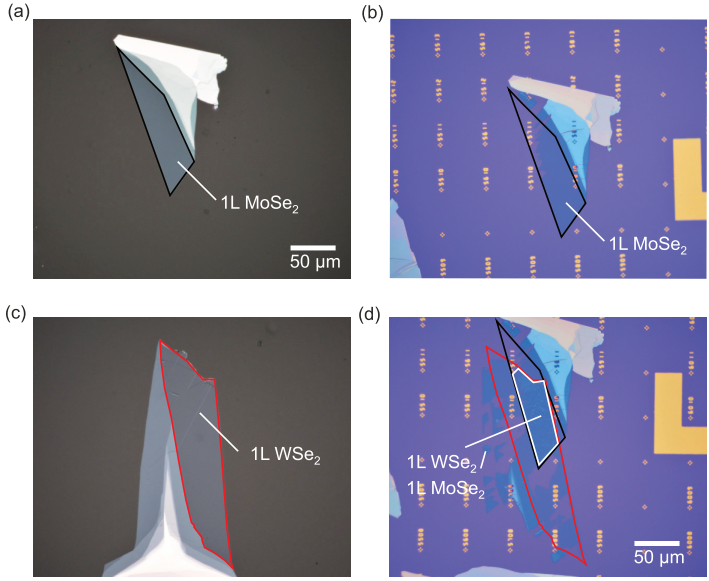


**Figure 4.2 |** Fabrication process of a two-dimensional $WSe_2/MoSe_2$ heterostructure. (a) Monolayer $MoSe_2$ on the PDMS film, the black-framed area indicates the monolayer region. (b) Monolayer $MoSe_2$ after transfer on the $SiO_2$ substrate. (c) Monolayer $WSe_2$ on the PDMS film, the red-framed area indicates the monolayer region. (d) $WSe_2/MoSe_2$ heterostructure on a $SiO_2$ substrate. The white-framed area depicts the region, where the two materials overlap vertically.

spacer could be observed in a specifically designed experiment [Fan14], where a monolayer of hBN was placed between a $MoS_2/WSe_2$ heterostructure resulting in a strong reduction of the interlayer exciton signal. A feasible approach to effectively enhance the contact of the heterojunction is provided by thermal annealing [Ton14, Kun18]. For this, the sample is put under vacuum and heated up to temperatures ranging from 120 C° to 500 C° [Fri18b]. During annealing, the mobility of the adsorbates is increased, leading to a segregation into small local pockets and consequently to a reduction of the overall layer spacing [Uwa15]. Therefore, the emergence of small bubbles and wrinkles on a heterostructure can be principally considered as an indication of sufficient interaction between the layers.

In the case of the sample used for this thesis, no annealing was initially required since the heterostructure showed clear signs of good contact between the layers as indicated by the emerges of large bubbles. This assessment was corroborated by the observation

of pronounced interlayer exciton emission right after fabrication. However, approximately 6 months after fabrication of the sample, the obtainable signal in the region of the heterostructure mostly vanished. Therefore, to recover the signal, the sample was initially flushed with both hydrogen and argon gas and subsequently annealed in high vacuum at a temperature of 150 C° for five hours, following the approach from [Kun18]. After the procedure, the signal from the interlayer exciton could be observed again with the same magnitude as before, clearly evidencing the positive effects of annealing on the interaction between the layers.

### 4.2.2 Determination of the twist angle via SHG

The twist angle between the two individual monolayers of the $WSe_2/MoSe_2$ heterostructure has direct implications for the physical properties of the system. As discussed in the introduction of this chapter, radiative recombination of interlayer excitons in a $WSe_2/MoSe_2$ heterostructure is only allowed for twist angles close to 0° or 60°. Furthermore, the stacking configuration (AA or AB) is expected to influence the behavior of interlayer excitons in an out-of-plane magnetic field, which will be elaborated in section 4.4.

Previous works have demonstrated that second harmonic generation (SHG) spectroscopy is a highly suitable tool to determine the crystallographic orientation of monolayer TMDCs [Mal13, Li13, Zen13, Hsu14, Jan15]. In this context, one has to consider the two relevant crystallographic orientations in a hexagonal honeycomb lattice, namely the armchair and the zigzag direction as schematically depicted in Fig. 4.3(a). In summary, a total of six armchair and six zigzag directions can be found in the respective lattice.

A comprehensive derivation of SHG in monolayer TMDCs and its peculiar dependence on the crystal directions can be found for instance in [Moo15b, Ple16a]. Briefly, it can be shown, using the crystal symmetry and the nonlinear susceptibility tensor $\chi^{(2)}$ that the polarization vector of the second harmonic emission rotates by twice the angle to the armchair direction and in opposite rotation direction with respect to the polarization of an incident electric field $E(\omega)$. This leads to a parallel (perpendicular) response of the second harmonic emission with respect to the incident polarization if the incident polarization is aligned with the armchair (zigzag) directions of the crystal. Therefore, by selecting either the SHG intensity parallel ($I_{||}$) or perpendicular ($I_{\perp}$) to the polarization direction of the incident electric field, it is possible to determine the crystallographic orientation using

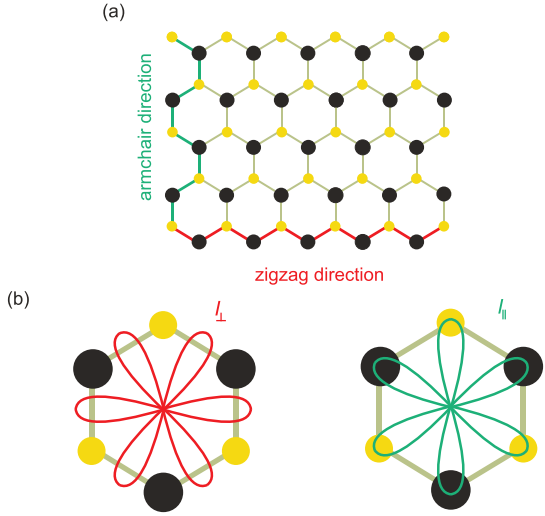


**Figure 4.3 |** (a) Schematic top view of a TMDC lattice with the indicated armchair (green) and zigzag (red) crystal directions. (b) Polar plot of the perpendicular ($I_\perp$) and parallel ($I_{||}$) components of the total second harmonic intensity. The relative orientation of the components with respect to the crystal is visualized by the hexagonal cell of a monolayer TMDC.

$$I_\parallel \propto \cos^2(3\theta) \qquad (4.1)$$
$$I_\perp \propto \sin^2(3\theta),$$

where $\theta$ is the angle between the incident laser polarization and the armchair direction of the crystal. These relations are further illustrated in Fig. 4.3(b), which shows the polar plots of the parallel and perpendicular components of the overall second harmonic intensity in relation to the crystal lattice. Rotating the excitation polarization by 360° results in six lobes for the armchair ($I_{||}$) and zigzag ($I_\perp$) direction of the crystal. Importantly, due to the phase-insensitivity of the SHG intensity measurement, the crystallographic directions can only be determined with an arbitrariness of 60°, as the monolayer follows a threefold symmetry while either six lobes for the armchair or the zigzag direction arise in the SHG measurement.

Based on these theoretical considerations we now determine the crystallographic alignment of the $WSe_2/MoSe_2$ heterostructure under study by means of SHG spectroscopy.

The buildup of the respective setup and the SHG characterization of the sample using this technique for the course of this thesis were conducted by Fabian Mooshammer.

The measurement is performed in a setup similar to the one presented in section 3.1.1 with a few modifications. Being a nonlinear process, second harmonic generation scales quadratically with the incident laser intensity. Therefore, for the excitation of the sample, a pulsed Titanium:sapphire laser with 100 fs pulses at a central wavelength of 810 nm and a repetition rate of 80 MHz is used, reaching a peak power of over 6 kW. The laser pulses are focused on the sample by a 40x objective. In order to separate the SHG signal from the near-infrared laser beam, the reflected signal is guided onto a cold mirror, which is only reflective for wavelengths shorter than 500 nm. Further suppression of the laser beam is obtained by a shortpass. The remaining SHG signal is subsequently coupled into a grating spectrometer and detected with a CCD camera. To determine the armchair directions of the crystals in polarization-resolved measurements, the laser light is linearly polarized and the reflected light analyzed by the same polarizer, hence selecting the parallel signal component ($I_{\parallel}$) of the SHG. In order to achieve angular resolution, the sample is rotated by a mechanical stage in consecutive steps of 5°, to avoid the pronounced polarization anisotropy of the beamsplitters. Figure 4.4(a) shows the second harmonic intensity of the parallel component of the $WSe_2$ (red) and $MoSe_2$ (black) monolayers in a polar plot. The data is fitted with $I_{\parallel}=C\cdot\cos^2(3\theta+\theta_0)$. This procedure yields a relative stacking angle $\phi$ between the two monolayers of either $6° \pm 1°$ (AA-like stacking) or $54° \pm 1°$ (AB-like stacking). While we can conclude from the polarization-resolved SHG measurement that the monolayers show good alignment with respect to each other, no distinction between the AA and AB stacking can be made at this point.

To resolve the stacking of the studied heterostructure, it is necessary to study the SHG intensity of the heterostructure and relate it to the SHG intensity of the monolayers. Following a vectorial superposition of the contributing electric fields from the individual monolayers, the SHG intensity of the heterostructure can be written as [Hsu14]

$$I_{\mathrm{HS}} = I_{\mathrm{MoSe_2}} + I_{\mathrm{WSe_2}} + 2\sqrt{I_{\mathrm{MoSe_2}} I_{\mathrm{WSe_2}}}\cos(3\phi), \tag{4.2}$$

where $I_{\mathrm{HS}}$, $I_{\mathrm{MoSe_2}}$, and $I_{\mathrm{WSe_2}}$ are the SHG intensities in the heterostructure region, the monolayer $MoSe_2$ and the monolayer $WSe_2$, respectively.

Hence, for a stacking angle of $\phi = 0°$ the SHG signal on the heterostructure $\mathrm{I_{HS}}$ is maximal due to a constructive interference of the two individual fields, whereas for $\phi = 60°$ the signal is minimal due to destructive interference. It should be noted that

the intensity of the SHG is strongly enhanced if the excitation wavelength of the laser is in the vicinity of the energy of an excitonic resonance in the respective monolayer [Mal13]. Due to the unequal energies of these resonances in $MoSe_2$ and $WSe_2$, we usually have $I_{WSe_2} \neq I_{MoSe_2}$ for a given excitation wavelength.
Figure 4.4(b) shows a spatial scan of the heterostructure, where the total SHG intensity is recorded for each position and overlaid on the image of the sample. For this measurement, the sample is excited using circularly polarized light without any polarization analysis in detection.

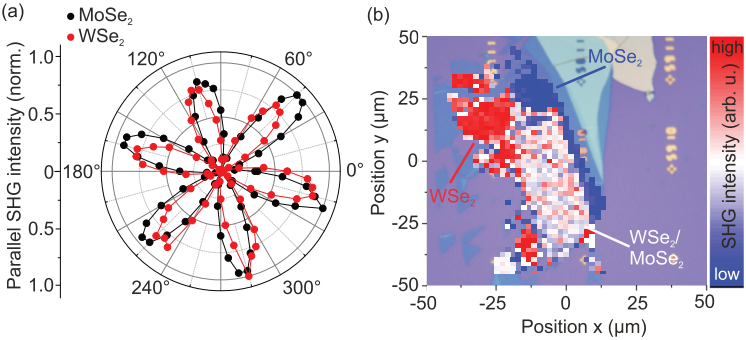


**Figure 4.4** | (a) Angle-dependent intensity of the parallel component of the SHG of the $MoSe_2$ and $WSe_2$ monolayers, indicating the armchair directions of the crystals. (b) Area scan of the sample, where the total recorded SHG intensity is shown for each data point in a false color plot combined with an optical image of the heterostructure. In the region of the heterostructure, destructive interference of the total SHG signal with respect to the individual monolayers can be observed.

Clearly, in the region of vertical overlap of the two layers (white region), we find pronounced destructive interference of the total SHG signal as it is smaller than the aggregated signal of the individual monolayers. Therefore, we can conclude that the heterostructure under study has an AB-like stacking configuration with a relative angle of $54° \pm 1°$. As mentioned previously, such a well-aligned sample is a crucial prerequisite for efficient radiative recombination of interlayer excitons in a $WSe_2/MoSe_2$ heterostructure, which will be discussed in the following section.

### 4.2.3 Photoluminescence characteristics

After the successful determination of the twist angle and the resulting stacking configuration, this section will cover general photoluminescence characteristics of the interlayer exciton that emerges in the heterostructure. As discussed in section 2.5, the expected band alignment in TMDC heterostructures is usually of type II nature, which is a prerequisite for the formation of interlayer excitons. To understand the emergence of interlayer excitons in an AB-stacked $WSe_2/MoSe_2$ heterostructure, we need to consider the specific alignment of the spin-split conduction and valence bands of the respective materials as shown in Fig. 4.5(a).

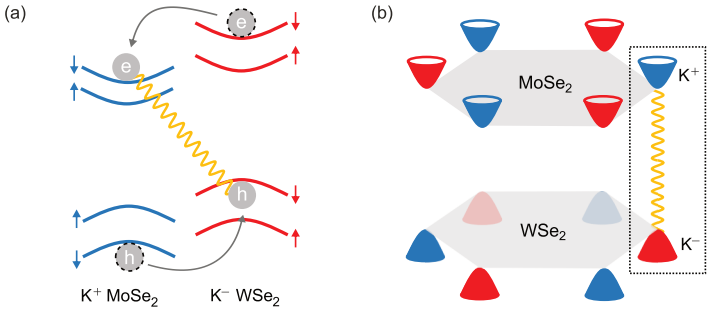


**Figure 4.5 |** (a) Type II band alignment of the spin-split conduction and valence bands of $MoSe_2$ and $WSe_2$ in an AB-stacked heterostructure. After photoexcitation of the monolayers, the electron-hole pairs undergo relaxation and energetically favorable spin-conserving charge transfer leading to the formation of an interlayer exciton across the two materials. (b) Momentum space arrangement of the relevant band extrema in the AB-stacked $WSe_2/MoSe_2$ heterostructure giving rise to an intervalley interlayer exciton.

The excitation from a laser initially creates electron-hole pairs in the individual monolayers, which subsequently undergo ultra-fast charge transfer, in this case the electrons from $WSe_2$ to $MoSe_2$ and the holes from $MoSe_2$ to $WSe_2$. The indicated specific positions of electrons and holes in the conduction and valence bands after excitation and the resulting interlayer exciton follow from two considerations. First, efficient charge transfer between the different materials is only expected if it is spin-conserving [Yu15b, Riv16]. Second, also the radiatively allowed recombination of the interlayer exciton can only take place if it conserves spin. Therefore, the interlayer exciton in an AB-stacked $WSe_2/MoSe_2$ heterostructure is composed of an electron from the upper conduction band in $MoSe_2$ at the $K^+$ point and a hole from the highest valence band in $WSe_2$ at the $K^-$ point (and by time-reversal symmetry, also from $K^-$ in $MoSe_2$ to

$K^+$ in $WSe_2$), as indicated in Fig. 4.5(a). The overall arrangement of the band extrema that contribute to the formation of the interlayer exciton in momentum space is depicted in Fig. 4.5(b). Importantly, the AB stacking of the heterostructure enables radiatively-allowed interlayer excitons that form between valleys of different index. Following these general considerations, we now return to the specific heterostructure (Fig. 4.6(a)) that was fabricated to study fundamental characteristics of the PL of interlayer excitons throughout the course of this thesis.

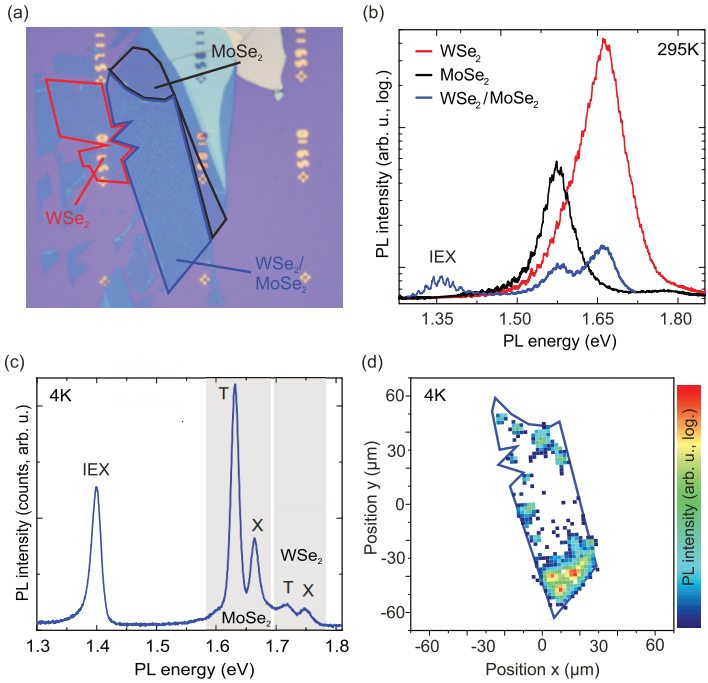


**Figure 4.6 |** (a) Image of the $WSe_2/MoSe_2$ heterostructure under study. The blue-framed area depicts the region, where the two materials overlap. (b) PL spectra at room temperature of the three different regions of the heterostructure. (c) PL spectrum on the heterostructure at 4 K. The emission from the interlayer exciton is energetically separated from the recombination of excitons (X) and trions (T) of the individual monolayer materials. (d) PL scan of the heterostructure at 4 K showing the spatial distribution of interlayer exciton emission across the sample.

As can be seen, the sample allows us to address and compare the spectral response of three different regions, namely monolayer $WSe_2$ (red-framed), monolayer $MoSe_2$ (black-

framed) and the $WSe_2/MoSe_2$ heterostructure (blue-framed). Steady-state PL spectra at room temperature of these three regions are presented in Fig. 4.6(b) on a logarithmic scale. The emission from monolayer $WSe_2$ and $MoSe_2$ shows the well-known pronounced peaks at the excitonic resonance at energies of about 1.65 eV ($WSe_2$) and 1.55 eV ($MoSe_2$) [Ton13]. On the heterostructure (blue spectrum), however, the PL characteristics deviate distinctively. First, the emission at the energies of $WSe_2$ and $MoSe_2$ is strongly quenched with respect to the intensity of the individual monolayers. This observation can be explained by considering the charge transfer process across the heterostructure. As it was shown, this process takes places on ultra-fast timescales, providing an efficient relaxation channel for the initially photo-excited electron-hole pairs [Hon14, Ceb14, Pen16]. Hence, the emission from the individual monolayers in the heterostructure will be suppressed. Second, and more importantly, at the low-energy side of the spectrum at around 1.35 eV, a novel feature emerges that is not present in the monolayer systems. In line with previous reports on a $WSe_2/MoSe_2$ heterostructure [Riv15, Riv16, Ros17], this peak is attributed to the radiative recombination of interlayer excitons. Note that the observable substructure of the IEX at room temperature results from etaloning effects of the back-illuminated CCD camera in the infrared range.

Cooling the sample down to 4 K strongly reduces the inhomogeneous broadening of the PL peaks and gives access to the different excitonic features, as can be seen in Fig. 4.6(c), which shows a spectrum recorded on the heterostructure. The emission stemming from the individual monolayers ($WSe_2$ and $MoSe_2$) now consists of two separate peaks, which can be related to the recombination from neutral excitons (X) and trions (T). The IEX peak is energetically well separated from the peaks of the individual monolayers and the linewidth of the IEX is strongly reduced with respect to the emission at room temperature amounting to about 20 meV. To acquire an understanding of the spatial distribution of the PL emission of the IEX across the heterostructure region, a PL scan of the sample at 4 K is performed. Figure 4.6(d) shows the extracted PL intensity of the IEX for each data point of the scan on a logarithmic scale. The emission is not spatially uniform over the whole heterostructure (blue frame) but rather concentrated on a larger region at the bottom. Presumably, in the regions without IEX emission, the coupling between the two monolayers is not strong enough to allow for efficient interaction. Nevertheless, the area of continuous IEX emission ($\approx 20 \times 30\,\mu m$) is by far sufficient to perform reliable PL experiments in the µm-regime.

### 4.2.4 Photoluminescence excitation spectroscopy

To further strengthen the assignment of the observed PL emission at around 1.4 eV to the interlayer exciton, photoluminescence excitation (PLE) measurements are performed. In such an experiment, the excitation wavelength of the laser is continuously tuned across the resonances of the individual monolayers and the intensity of the IEX is recorded for each excitation energy. Experimentally, this is achieved by using a similar setup as described in section 3.1 but with a tunable CW-Titanium:sapphire laser system. The emitted PL from the sample is coupled into a grating spectrometer and detected using a liquid-nitrogen-cooled CCD. Figure 4.7(a) shows the resulting PL intensity of the IEX as a function of the excitation energy, which is varied in 2 nm steps from about 1.54 eV (805 nm) to 1.73 eV (715 nm). The incident laser power is 100 µW and the sample was kept at a temperature of 4 K. As can be clearly seen, the IEX PL intensity is strongly enhanced at excitation energies of about 1.65 eV and 1.73 eV. For an excitation with energies below 1.6 eV, the emission from the IEX vanishes.

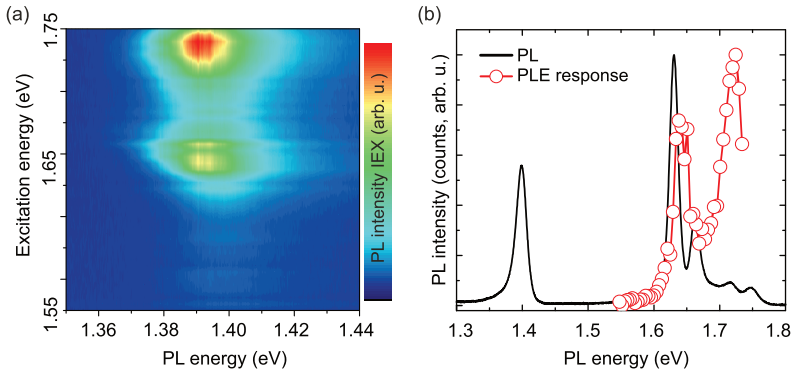


**Figure 4.7 |** (a) PLE plot of the IEX PL intensity depending on the excitation energy of the laser, clearly showing the two resonances of the IEX PL intensity at the energies of $MoSe_2$ (1.65 eV) and $WSe_2$ (1.73 eV). (b) The PL of the IEX (black line) in conjunction with the spectrally integrated PLE response (red connected dots).

The enhancement of the IEX PL at energies of about 1.65 eV and 1.73 eV can be directly related to the main excitonic resonances of $MoSe_2$ and $WSe_2$ as it is shown in Fig. 4.7(b). Here, the spectrally integrated PLE response of the IEX is superimposed on the PL spectrum measured on the heterostructure. Once the laser energy matches an absorption maximum of one of the two respective monolayers, the formation of interlayer excitons is strongly favored. Consequently, for excitation energies smaller

than the resonance of $MoSe_2$, no absorption can occur and therefore also no emission from the IEX as evidenced in the measurement. Hence, the PLE spectrum provides further evidence for the interlayer nature of the IEX peak, resulting from the charge transfer across the $WSe_2/MoSe_2$ interface. The observation of two resonances also largely precludes an alternative interpretation of the low-energy feature in which an intralayer exciton is bound to a defect in one of the two monolayers. Such a process would likely result only in resonances related to one of the corresponding layers, but not to both of the monolayers.

### 4.2.5 Valley polarization of interlayer excitons

For monolayer TMDCs, the creation and observation of valley polarization in helicity-resolved optical experiments is a well-established concept by now (see section 2.3). In the following, it will be shown that this notion can be extended to interlayer excitons in a $WSe_2/MoSe_2$ heterostructure, as it was first demonstrated by Rivera *et al.* [Riv16].

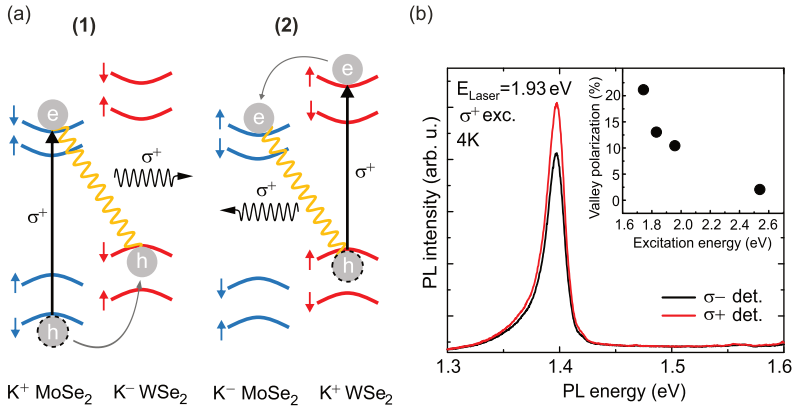


**Figure 4.8 |** (a) Schematic illustration of the two spin-allowed pathways leading to polarized emission in an AB-stacked $WSe_2/MoSe_2$ heterostructure for the case of $\sigma^+$ polarized excitation. $\sigma^+$ polarized light can couple to the $MoSe_2$ B exciton (1) in the $K^+$ valley and the $WSe_2$ A exciton in the $K^+$ valley (2). Spin-conserving interlayer hopping of the hole in $MoSe_2$ (1) or the electron in $WSe_2$ (2) leads to interlayer excitons, which radiatively recombine under the emission of $\sigma^+$ polarized light. (b) Helicity-resolved PL spectra of the interlayer exciton with a laser energy of 1.93 eV and $\sigma^+$ polarized excitation. The inset shows the degree of valley polarization of the IEX in dependence of the excitation energy.

To understand the emergence of valley polarization for interlayer excitons in an AB-stacked $WSe_2/MoSe_2$ heterostructure, we have to consider the optical selection rules for

polarized excitation and emission as shown in Fig. 4.8(a) for the case of $\sigma^+$ polarized excitation.

Following the selection rules presented in section 2.3, $\sigma^+$ polarized light can couple to the B exciton transition of $MoSe_2$ in the $K^+$ valley (scenario (1) in Fig. 4.8(a)) and to the A exciton transition of $WSe_2$ in the $K^+$ valley (scenario (2) in Fig. 4.8(a)). Due to the small momentum mismatch in the studied AB-stacked heterostructure, the holes from $MoSe_2$ and the electrons from $WSe_2$ subsequently undergo efficient spin-conserving interlayer hopping to the energetically favorable valence band of $WSe_2$ and conduction band of $MoSe_2$, respectively [Riv16]. Finally, the interlayer exciton can radiatively recombine in both scenarios under the emission of $\sigma^+$ polarized light. An additional possibility to observe valley-polarized interlayer excitons could stem from the excitation of A excitons in $MoSe_2$ as it was also observed in the PLE measurements in the previous section. However, this process would involve an additional thermal excitation of electrons to the upper conduction band of $MoSe_2$ including a spin-flip, which is mostly suppressed at the nominal sample temperature of 4 K.

Figure 4.8(b) shows a helicity-resolved steady-state PL spectrum of the IEX from the heterostructure under study at a sample temperature of 4 K. The excitation laser is $\sigma^+$ polarized and has an energy of 1.93 eV. As can be seen, the PL intensity in detection is higher for the $\sigma^+$ polarized component, giving rise to a valley polarization of about 10 %. The inset of Fig. 4.8(b) depicts the obtainable degree of polarization as a function of different excitation energies. While for highly non-resonant excitation (2.54 eV), no discernible valley polarization is observed, a laser energy of 1.72 eV results in a polarization of more than 20 %. The lack of valley polarization at high excess energies was also frequently observed in monolayer TMDCs and can be attributed to fast depolarization mechanism after excitation [Kio12, Sal12, Kio16]. The comparatively high degree of valley polarization at a laser energy of 1.72 eV can most likely be related to the quasi-resonant excitation of the A exciton of $WSe_2$ at this energy (scenario (2)) in Fig. 4.8(a)), leading to an efficient injection of polarized carriers.

As discussed in section 2.3, the long-range exchange interaction is the major source of valley depolarization in monolayer TMDCs. Due to the tightly bound excitons in these materials, the mechanism is very efficient and leads to ultrafast valley depolarization times on the order of picoseconds. Following this notion, longer valley depolarization times can be expected for interlayer excitons. Due to the spatial separation of electrons and holes across the two monolayer TMDCs, the electron-hole wave function overlap should be reduced and consequently the long-range exchange interaction suppressed. Indeed, Rivera *et al.* [Riv16] have observed valley lifetimes of interlayer excitons in

a $WSe_2/MoSe_2$ heterostructure in the nanosecond regime, exceeding typical values of monolayer TMDCs by orders of magnitude. However, an experimental confirmation of the time-resolved results by Rivera *et al.* [Riv16] during the course of this thesis was precluded by technical difficulties.

## 4.3 Interaction effects and dynamics of interlayer excitons

Following the PL characterization of interlayer exciton emission in a $WSe_2/MoSe_2$ heterostructure in the previous section, we now focus on interaction effects and the dynamics of this excitonic species. Novel insights will be obtained by examining the PL emission under the influence of different temperatures, excitation densities and a thorough analysis of the time-resolved emission behavior of interlayer excitons. As we will see, the spectral properties of interlayer excitons differ drastically in comparison to their intralayer counterparts. All experiments in section 4.3 have been carried out with a pulsed laser as the excitation source unless otherwise noted. This section follows the presentation of [Nag17b], where the results were published.

### 4.3.1 Diffusion in an inhomogeneous potential landscape

We start by analyzing the main characteristics of interlayer exciton emission for different sample temperatures in steady-state PL measurements. Figure 4.9(a) shows a temperature series of normalized PL spectra obtained on the heterostructure, which allows us to track the evolution of intensities, the peak positions and the spectral widths of both the interlayer and intralayer excitons at the same time. At a sample temperature of 4 K, the PL emission from the interlayer exciton dominates the spectrum while the intralayer exciton emission is suppressed. For higher temperatures up to 60 K, the relative emission strength from $MoSe_2$ and $WSe_2$ increases with respect to the interlayer exciton.
Fig. 4.9(b) illustrates the PL intensities of $MoSe_2$, $WSe_2$ and the IEX, which are normalized to the maximum PL intensity within the studied temperature range. As can be clearly seen, the emission from $MoSe_2$ and $WSe_2$ behave drastically different as the temperature is increased up to 200 K. While the PL yield of $MoSe_2$ steadily decreases with temperature, the opposite is the case for $WSe_2$. This contrasting behavior directly follows from the different sign of the conduction band splitting of $MoSe_2$ and $WSe_2$ as presented in section 2.1.2 and is in line with recent experimental observa-

tions [Zha15c, Wan15c, Aro15a]. In the case of $WSe_2$, where the sign of the splitting is negative and consequently the ground state optically dark, the PL yield increases with temperature due to thermally activated emission from the energetically unfavorable upper conduction band, which hosts the spin-allowed transition. As the ground state of $MoSe_2$ is optically bright due to the positive sign of the conduction band spin splitting, the PL yield decreases with temperature [Aro15b].

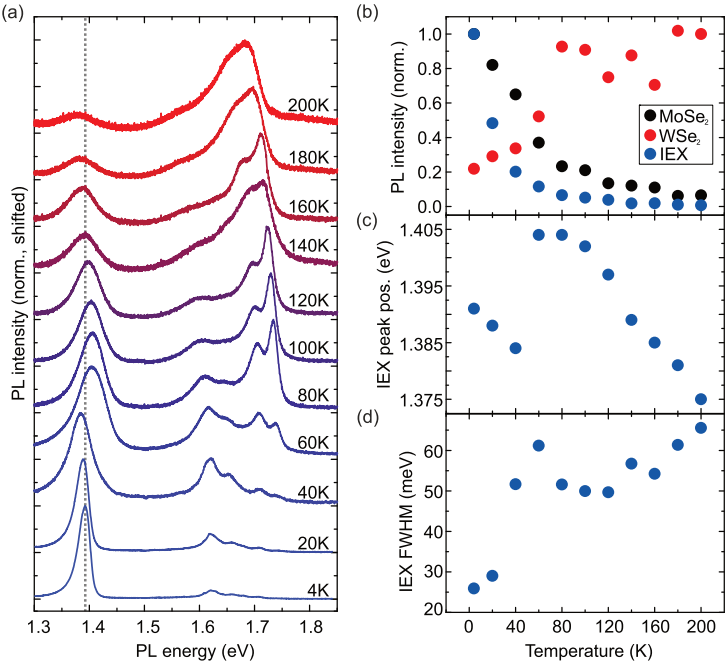


**Figure 4.9** | (a) Normalized PL spectra with fixed excitation power measured on the $WSe_2/MoSe_2$ heterostructure as a function of temperature. The vertical line indicates the peak position of the IEX at 4 K. (b) Normalized PL intensity of the IEX and the intralayer $MoSe_2$ and $WSe_2$ emission as a function of temperature. (c) Peak position of the IEX as a function of temperature. (d) Spectral linewidth of the IEX as a function of temperature.

We proceed by analyzing the peak position (Fig. 4.9(c)) and spectral width (Fig. 4.9(d)) of the interlayer exciton as a function of temperature. Clearly, both properties show a non-monotonic behavior as a function of temperature. The IEX peak redshifts about 10 meV between 4 K and 40 K with increasing temperature and then undergoes a rapid blueshift of more than 20 meV as the temperature rises from 40 K to 60 K. From

60 K to 200 K the peak position of the IEX undergoes a continuous redshift of about 30 meV. At the same time, the spectral width of the IEX peak almost doubles while the temperature is increased from 20 K to 40 K, has a maximum at 60 K and remains nearly unchanged in the range from 80 K to 120 K. Increasing the temperature further up to 200 K results in a steady increase of the linewidth.
Remarkably, in comparison to the IEX, both the peak position and the FWHM of the intralayer excitonic features of $MoSe_2$ and $WSe_2$ behave distinctively different and in line with the typical behavior of semiconductors. This is evidenced in Fig. 4.10, which shows data of the neutral exciton. The data in Fig. 4.10 is not obtained on the heterostructure but on isolated $MoSe_2$ and $WSe_2$ monolayers to facilitate data acquisition since the intralayer PL is strongly quenched at low temperatures on the heterostructure. Nevertheless, the intralayer PL shows generally the same behavior on the heterostructure region. As shown in Fig. 4.10(a), the FWHM of both features steadily increases in the investigated temperature range from around 15 meV to 30 – 40 meV. Such a monotonic broadening of the spectral linewidth is commonly observed for intralayer excitons in monolayer TMDCs and is mostly induced by increased exciton-phonon scattering with rising temperatures [Sel16].

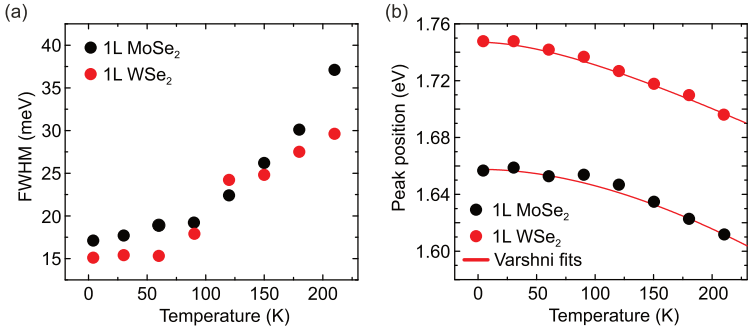


**Figure 4.10 |** (a) Spectral linewidth (FWHM) of the emission from the neutral exciton of $MoSe_2$ (black dots) and $WSe_2$ (red dots) as a function of temperature. (b) Peak position of the neutral exciton for $MoSe_2$ and $WSe_2$ as a function of temperature. The red line indicates a Varshni fit to the data.

The peak position of the neutral exciton of $MoSe_2$ and $WSe_2$ decreases continuously in the temperature range from 4 K to about 200 K (see Fig. 4.10(b)). This is a well-known phenomenon in semiconductors stemming from the thermal expansion of the crystal lattice, which is accompanied by a change of the band structure as well as the strength of the electron-phonon coupling. A possible phenomenological description

of the temperature dependence of the bandgap was proposed by Y.P. Varshni by the following formula [Var67]:

$$E_g(T) = E_g(0) - \frac{\alpha T^2}{T + \beta} \ . \tag{4.3}$$

Here, $E_g(T)$ is the energy of the band gap, $E_g(0)$ the energy of the bandgap at 0 K and $\alpha$ and $\beta$ fit constants. As can be seen in Fig. 4.10(b), the function by Varshni provides a reasonable fit to the experimentally obtained transition energies of the neutral exciton. At this point, we aim to understand why the peak position and the FWHM of the IEX behave in such stark contrast to the intralayer excitons of $MoSe_2$ and $WSe_2$. A so-called s-shape of the excitonic emission energy as we observe it for the IEX peak in conjunction with a drastic increase of the linewidth of the emission is reminiscent of the temperature-dependent PL spectra in bulk semiconductors and quantum well systems, which are subject to a significant amount of disorder [Sko86, Rub05, Rub07, Imh10, Imh11]. In such systems, local minima of the potential landscape can lead to trapping of excitons at low temperatures. Once the temperature rises, the diffusivity of excitons increases via phonon-assisted hopping, allowing the excitons to diffuse to energetically reduced trap states. The scenario of a locally inhomogeneous potential landscape is further depicted in Fig. 4.11(a).

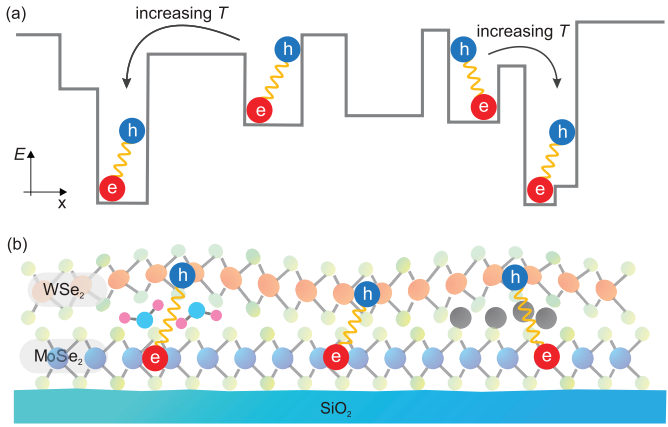


**Figure 4.11 |** (a) Disorder-induced excitonic potential landscape. Increasing the temperature allows excitons to diffuse to energetically lower states. (b) Schematic illustration of a heterostructure, where adsorbates between the two TMDC monolayers lead to a spatially inhomogeneous potential landscape and a modulation of the exciton binding energy.

Given the fabrication process used for the two-dimensional heterostructure in this thesis, it is very likely that interlayer excitons are subject to a significant amount of disorder. As Fig. 4.11(b) illustrates, the ambient conditions during the sample fabrication lead to the inclusion of adsorbates in between the layers and consequently to a strong variation of the potential landscape. Additionally, the modulation of the distance between the layers entails a spatial modification of the electron-hole distance and correspondingly the IEX binding energy.

Within this framework, we can now understand the anomalous behavior of the peak position and the FWHM of the IEX as a function of temperature (Figs. 4.9(c),(d)). Temperature-activated diffusion of the interlayer exciton within the inhomogeneous potential landscape results in an initial, pronounced redshift of the PL peak position from 4 K to 40 K as local and global minima of the potential become energetically accessible (see Fig. 4.11(a)) [Bar98, Tar01]. At the same time, the drastic increase of the FWHM of the IEX emission peak within this temperature range follows from the broader distribution of possible photon energies as the carriers can recombine radiatively from a higher number of localized sites. Between 40 – 60 K, the thermal energy is sufficient to promote carriers to higher-lying states, leading to a blue-shift of the PL maximum and the FWHM reaches a local maximum. As the temperature is further increased, the excitons are entirely delocalized and the continuous redshift of the IEX emission follows from the bandgap reduction of the constituent monolayers (see Fig. 4.10(b)). In this temperature regime, the increasing FWHM of the IEX peak stems from the phonon-induced broadening, which is also the dominant mechanism in monolayer TMDCs (Fig. 4.10(a)). Additional evidence for the presented interpretation will be provided by measurements of the temperature-dependent PL lifetime of the IEX in section 4.3.3.

### 4.3.2 Dipolar exciton-exciton interaction

As we have seen in the last section, the PL emission from interlayer excitons in a 2D heterostructure can show pronounced differences compared to the emission from intralayer excitons in monolayer materials. In the following, steady-state power-dependent PL measurements will further strengthen this notion and reveal exciton-exciton mechanisms of interlayer excitons that are not present in TMDC monolayer systems.

Figure 4.12(a) shows power-dependent PL measurements from 2 – 200 µW excitation power using pulsed excitation on the region of the heterostructure at 4 K, which allows us to track the spectral evolution of the IEX and $MoSe_2$ features simultaneously. As

presented in Fig. 4.12(b) and (c) respectively, the peak positions of the IEX and the neutral exciton feature of $MoSe_2$ show a markedly different behavior in the investigated excitation power range. Strikingly, while the peak position of the IEX exhibits a blueshift with increasing power by up to 10 meV and saturates at high excitation powers ($> 90\,\mu W$), the intralayer exciton emission of $MoSe_2$ shifts by less than 1 meV in the entire investigated excitation power range.

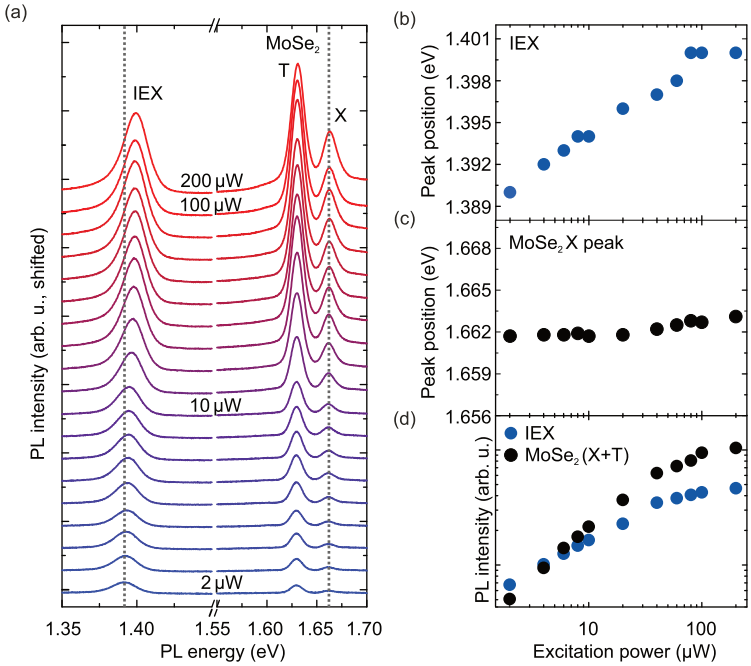


**Figure 4.12 |** (a) Power-dependent PL spectra measured on the heterostructure at 4 K. The vertical lines indicate the spectral position of the IEX peak and the X peak of $MoSe_2$ at an excitation power of 2 µW. (b) Peak position of the IEX peak as a function of excitation power. (c) Peak position of the $MoSe_2$ X peak as a function of excitation power. (d) Integrated PL intensity of IEX (blue dots) and intralayer $MoSe_2$ (black dots) emission from exciton (X) and trion (T) as a function of excitation power at 4 K.

The slope of the blueshift of the IEX in Fig. 4.12(b) is sublinear, which indicates that the effective IEX PL lifetime decreases with increasing power. Higher excitation powers imply an increased electron-hole pair density in both TMDC monolayers, which enables additional intralayer exciton recombination and lowers the efficiency of the

formation of interlayer excitons. This interpretation is confirmed by comparing the total PL intensity of the IEX and both excitonic features of $MoSe_2$ as presented in Fig. 4.12(d). At low excitation powers, the PL intensity from the IEX is clearly higher than the emission stemming from $MoSe_2$. However, the intralayer emission from $MoSe_2$ surpasses the IEX emission for excitation powers higher than 6 µW. As the excitation power is further increased, the PL from the IEX clearly saturates with respect to the $MoSe_2$ emission, implying that the recombination pathway for intralayer exciton recombination becomes more efficient with increasing electron-hole pair density.
In order to understand the pronounced blueshift of the IEX peak, we need to consider the spatial arrangement of interlayer excitons in real space and compare it to the scenario for excitons in monolayer TMDCs as it is schematically illustrated in Fig. 4.13.

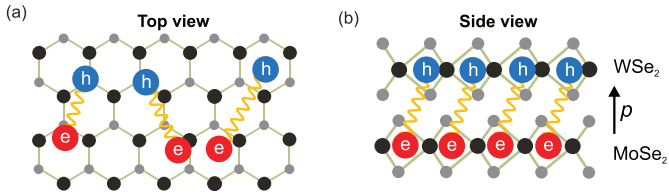


**Figure 4.13 |** Schematic illustration of the spatial arrangement of excitons for the case of (a) excitons in monolayer TMDCs and (b) spatially separated interlayer excitons in a 2D heterostructure, including the induced dipole moment $p$.

In a monolayer TMDC, the excitons are quasi free to move over the whole lattice plane even for elevated excitation densities (Fig. 4.13(a)). However, the situation is different for interlayer excitons in a TMDC heterostructure as illustrated in Fig. 4.13(b). Here, due to the type II band alignment and the resulting charge transfer process, electrons and holes are spatially separated into the two different layers. This leads to the emergence of a permanent dipole moment $p$ perpendicular to the heterostructure plane. Consequently, by increasing the exciton density in the heterostructure, the interlayer excitons will experience a repulsive dipole-dipole interaction as it was also theoretically described [Lai09] and experimentally observed for the case of indirect excitons emerging in GaAs-based double quantum well systems [But99]. Due to this repulsive mechanism, the energy of the interlayer exciton is reduced with increasing exciton density. This, in turn, manifests itself in an increase of the optical bandgap and consequently in a blueshift of the PL emission as evidenced in Fig. 4.12(b).

### 4.3.3 Photoluminescence dynamics

So far, the spectral analysis of the IEX feature was limited to steady-state PL measurements. Additional insight will be gained by probing the dynamics of the interlayer exciton in time-resolved experiments, which is the topic of the current section.
Due to the increased spatial separation of electrons and holes, interlayer excitons are expected to possess drastically longer lifetimes in comparison to excitons in monolayer TMDCs. In a first measurement, we access the PL dynamics of the IEX at a sample temperature of 4 K by using the setup provided by the HFML facility in Nijmegen without magnetic field (see section 3.1.2). Here, a pulsed diode laser (pulse length 80 ps, wavelength 690 nm, average power 18 µW, repetition rate 2.5 MHz) is synchronized to an avalanche photodiode (APD) and the PL emitted from the sample under this excitation is coupled into a monochromator set to the emission energy of the IEX of around 1.4 eV. Figure 4.14 shows the resulting PL trace of the interlayer exciton.

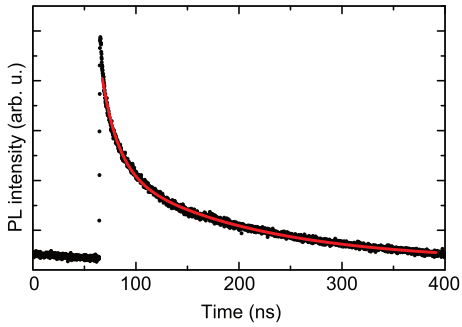


**Figure 4.14** | Time-resolved PL trace of the IEX (black dots) measured at 4 K using a pulsed diode laser and an avalanche photodiode. The red solid line is a biexponential decay function fitted to the data.

Intriguingly, the measured PL lifetime of the IEX is in the nanosecond regime as expected due to the increased electron-hole separation and in line with previous time-resolved studies on interlayer excitons in a $WSe_2/MoSe_2$ heterostructure, which were also recorded employing a spectrally integrating APD [Riv15, Riv16]. Using a biexponential fit function to extract the PL lifetime from the trace in Fig. 4.14, we obtain values of 16 ns ± 0.2 ns and 138 ns ± 2 ns for the fast and slow component of the decay, respectively. Alternatively, we can extract the $1/e$ constant of the PL decay of the interlayer exciton, which amounts to 40 ns.
At this point we can recapitulate that the PL lifetime of the IEX at 4 K indeed exceeds

measured lifetimes of intralayer excitons in monolayer TMDCs (see section 2.2) by orders of magnitude. However, since the time-resolved measurement with an APD is only sensitive to the overall PL intensity, no information on the spectral evolution of the PL decay can be extracted. For a more thorough understanding of the intricate interaction effects of interlayer excitons, such data can be crucial. Therefore, in a next step, we now investigate the PL dynamics of the IEX in a streak camera setup (see section 3.1.3), which provides time- and spectrally-resolved PL measurements at the same time.

Figure 4.15(a) shows a streak camera image of the IEX at 4 K on the heterostructure, which is excited with a pulsed fiber laser (pulse length 180 fs, wavelength 560 nm, average power 250 µW, repetition rate 80 MHz) and detected in the synchro-scan mode in time range 4. Interestingly, directly after excitation the PL is energetically broadened and exhibits a blueshift in comparison to emission at later times.

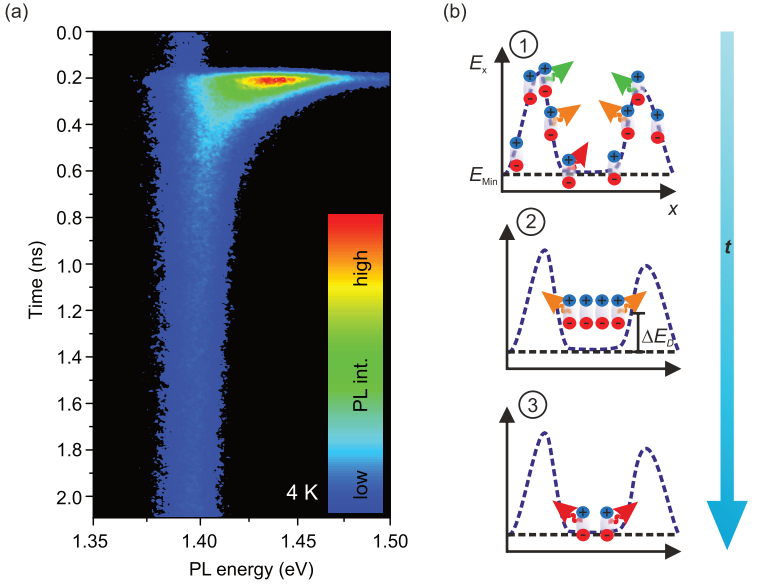


**Figure 4.15 |** (a) False-color streak camera image of the time-resolved PL spectrum of the IEX measured at 4 K. (b) Schematic illustration of interlayer exciton dynamics as a function of time, based on a three-step process, see main text for details.

The charge carriers then undergo an energetic relaxation leading to a very long-lived, spectrally narrow tail of the PL emission. Importantly, the lifetime of the PL emission

is longer than the available measurement window (2 ns) of the synchro-scan mode of the streak camera. As can be seen in the upper part of Fig 4.15(a), we even observe emission from the IEX before the arrival of the pump pulse, which implies that the PL lifetime of the IEX exceeds the 12.5 ns time window between subsequent excitation pulses given by the repetition rate of the laser of 80 MHz. The observation of PL lifetimes of the IEX in the multi-nanosecond regime in the streak camera setup is in full agreement to the previously presented data in the APD setup.

However, by using the streak camera system we now have access to the spectral evolution of the PL decay of interlayer excitons at low temperatures. In the following, we qualitatively explain these dynamics based on a three-step process by taking into account both the diffusion of the IEX in the inhomogeneous potential landscape (see also Fig. 4.11) and the repulsive interaction as depicted in 4.15(b). First (step 1), pulsed laser excitation leads to the creation of interlayer excitons across the entire heterostructure, which is characterized by an inhomogeneous potential landscape. Here, the total energy $E_{\mathrm{x}}$ of the interlayer exciton depends on the position $x$, where the minimal energy $E_{\mathrm{min}}$ is given by the minimal interlayer distance. Subsequently, interlayer excitons will diffuse to the local potential minima and partly radiatively recombine. This leads to the initial, spectrally broad emission of the PL decay as excitons at different positions within the potential landscape recombine. Second (step 2), the remaining interlayer excitons are trapped within the local potential minima and cool down towards the lattice temperature via phonon emission. In principle, this process results in a reduction of the inhomogeneous broadening of the PL emission as can also be seen in Fig. 4.15(a). However, at this point we also have to take into account the dipole-dipole interaction of interlayer excitons as discussed in section 4.3.2. Hence, the interlayer exciton is blueshifted by a density-dependent term $\Delta E_{\mathrm{D}}$. Finally (step 3), the exciton density decreases further, resulting in a reduction of repulsive interaction $\Delta E_{\mathrm{D}}$ and consequently to a decrease of the IEX PL energy towards the potential minimum characterized by $E_{\mathrm{min}}$.

In the next step, we will study the temperature dependence of the PL dynamics of the interlayer excitons. The obtained results will further support our understanding of the anomalous behavior of the peak position and the FWHM of the interlayer exciton in the steady-state PL measurements from section 4.3.1. The streak camera images of the PL decay of the interlayer exciton at a sample temperature of 20 K and 40 K are presented in Fig. 4.16(a) and (b), respectively. Similar to the behavior that we observe for 4 K, the spectra at both temperatures show an initially blueshifted and spectrally broad PL emission directly after excitation, which cools down to lower energies subse-

quently. Remarkably, the total lifetime of the PL emission drastically decreases with higher temperatures. In Fig. 4.16(c), the extracted total PL lifetime as a function of temperature is presented.

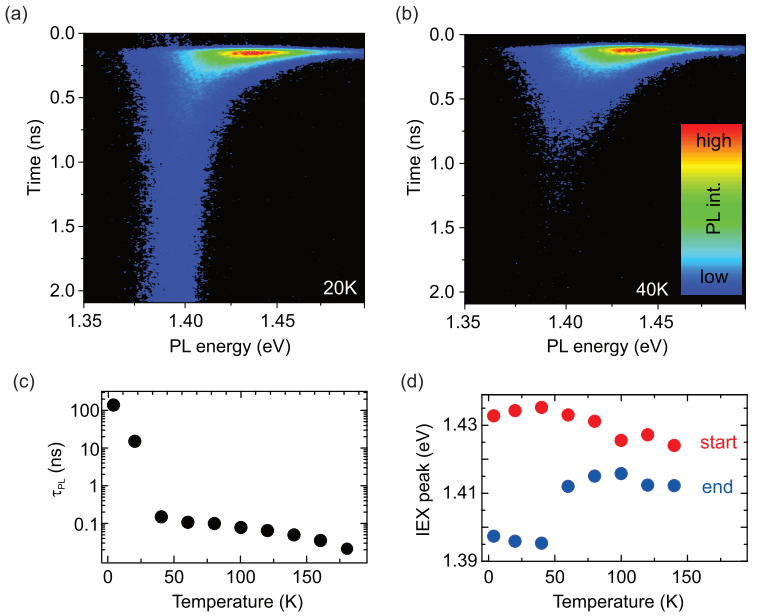


**Figure 4.16 |** False-color streak camera images of the IEX PL decay for (a) 20 K and (b) 40 K. (c) PL lifetime of the IEX as a function of temperature. The decay time at 4 K is extracted from the APD measurement. All other times are measured in the streak camera setup. (d) Spectral peak position of the IEX at the start and the end of a time-resolved PL trace as a function of temperature.

Note here that the decay time at 4 K provided in Fig. 4.16(c) is the long-lived component of the PL trace measured with the APD setup as such long times significantly exceed the available time window of the streak camera system. All other PL lifetimes measured at temperatures higher than 4 K in Fig. 4.16(c) are determined using the streak camera system. As can be seen, the total PL lifetime drastically drops with increasing temperature. Interestingly, by comparing the PL yield of the IEX from steady-state PL measurements under pulsed excitation (Fig. 4.9(b)) with the measured total PL lifetime as a function of temperature (Fig. 4.16(c)), we find that the pronounced reduction of the PL lifetime between 4 K and 40 K is not accompanied by

an accordingly drastic reduction of PL yield. As a consequence, the change of the PL yield of the IEX with temperature cannot solely follow from thermally activated non-radiative decay channels or Auger-type recombination. Compared to the temperature dependence of the total PL lifetime in monolayer TMDCs after non-resonant excitation, which usually rises with increasing temperature [Kor11], the observed drastic reduction of the IEX PL lifetime deserves further study. A possible explanation for this behavior, as also observed by Rivera *et al.* [Riv16], could be the momentum-indirect nature of the IEX. As shown in section 4.2.2, the $WSe_2/MoSe_2$ heterostructure under study is not perfectly aligned but has an stacking angle of $54° \pm 1°$. Therefore, the extrema of conduction and valence bands will exhibit a certain momentum mismatch in $k$-space. Consequently, a phonon-assisted process is required for radiative recombination of the IEX to obey momentum conservation. With increasing temperature, such a process becomes more probable, resulting in shorter PL lifetimes of the interlayer exciton. An additional contribution to this effect could stem from a thermal excitation of carriers to the upper conduction band of $MoSe_2$ with rising temperature from which interlayer excitons can recombine efficiently (see Fig. 4.5).

We continue our analysis of the temperature-dependent PL dynamics of the IEX by examining the peak position of the IEX at the start and close to the end of the overall PL lifetime. The analysis is performed by setting a temporal window with a width of 100 ps at the onset of the PL emission (start position) and at a later time after excitation, where the PL mostly decayed but still allows a reasonable extraction of the peak position (end position). The temporal window of the end position shifts to smaller time values with increasing temperature due to the overall reduction of the IEX PL lifetime. Figure 4.16(d) presents the results of this analysis. As can be seen, the IEX emission exhibits a large energy difference of more than 30 meV between start and end times for temperatures between 4 K and 40 K. Raising the temperature to 60 K leads to a strong reduction of this difference to less than 20 meV, which is further decreased as the temperature continues to rise. This implies that the available time window for diffusion and the accompanying energy relaxation of interlayer excitons is limited by the strong reduction of the PL lifetime with increasing temperature. Based on these observations we obtain additional insights into the anomalous temperature-dependent behavior of the steady-state PL emission of the IEX as shown in Fig. 4.9(c) and (d). Within the temperature range of 4 – 40 K, the IEX lifetime drastically decreases, which results in a reduction of the time-averaged interlayer exciton density for a constant excitation power. Hence, the repulsive exciton-exciton interaction is reduced, further contributing to the redshift of the steady-state PL emission in this temperature range

(Fig. 4.9(c)). For higher temperatures, the IEX PL lifetime becomes so short that the diffusion of interlayer excitons into the local energy minima is largely suppressed. This leads to an increase of the spectral linewidth of the PL (Fig. 4.9(d)) due to PL emission from energetically unfavorable regions of the inhomogeneous potential landscape.
Finally, we shed more light on the repulsive dipole-dipole interaction of interlayer excitons by studying the excitation power dependence of time-resolved PL traces at a fixed sample temperature of 4 K. Two representative streak camera images are pre-

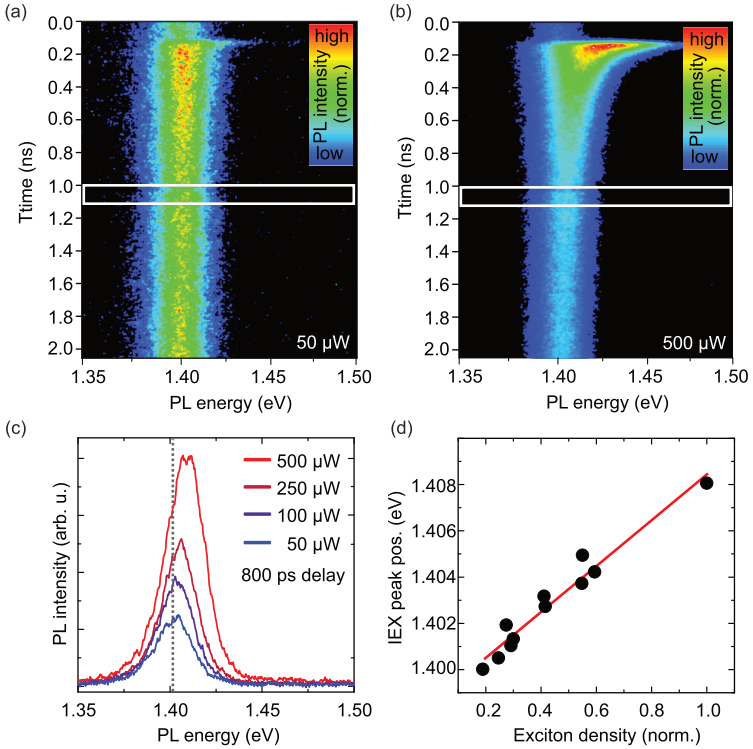


**Figure 4.17** | False-color streak camera images of time-resolved PL spectra of the IEX at 4 K with (a) 50 µW and (b) 500 µW excitation power. The white frame indicates the employed time window to obtain the spectra in (c). (c) PL spectra from time-resolved PL measurements extracted 800 ps after excitation at 4 different excitation powers measured at 4 K. (d) IEX peak position as a function of normalized exciton density, which was extracted from the spectra in (c), see main text for details. The red line serves as a guide to the eye.

sented in Fig. 4.17(a) and (b) with an average excitation power of 50 µW and 500 µW

respectively. Note that the PL intensity of the IEX in the two images is not directly comparable since it was normalized for each image individually. As can be clearly seen, the streak camera images at the two different excitation conditions reveal strikingly different decay dynamics of the interlayer exciton. For 50 µW excitation power, almost no time-dependent energy relaxation of interlayer excitons is discernible and the IEX PL intensity before the excitation pulse is of the same order of magnitude as after the excitation. In the case of 500 µW excitation power, the PL shows a pronounced redshift during the first 500 ps after arrival of the excitation pulse in combination with a significant reduction of the PL intensity. From this we can generally conclude that the peak position of the IEX strongly depends on the employed excitation power throughout the entire investigated time window, an observation we have already made in steady-state PL measurements in section 4.3.2.

To analyze this dependency for time-resolved PL spectra in more detail, we assume that the PL emission intensity is proportional to the exciton density for a sufficiently long time delay (after 800 ps) after laser excitation. Using a time window of 100 ps (see Fig. 4.17(a) and (b)) for temporal averaging, we then extract PL spectra at three different delay times after excitation (800 ps, 1.3 ns and 11.8 ns) for four different excitation powers (50 µW, 100 µW, 250 µW and 500 µW). Figure 4.17(c) shows the extracted PL spectra at a delay time of 800 ps for four different excitation powers, where we clearly observe a blueshift of the IEX PL peak position with increasing excitation density. In order to relate now the IEX peak position in time-resolved measurements with the exciton density, we deduce the PL intensity and the PL peak position for all 12 time delay/excitation power combinations and normalize the intensities to the value obtained for the shortest time delay (800 ps) and the highest excitation power (500 µW). The results of this procedure are shown in Fig. 4.17(d), where it can be seen that the peak position of the IEX increases with the exciton density and the overall blueshift amounts to about 10 meV. In contrast to the sublinear behavior observed in the steady-state PL power series (see section 4.3.2), the increase of the IEX peak position with excitation power in the time-resolved measurements follows a linear relation.

At this point, we can compare the blueshift of the IEX peak position of the power-dependent steady-state PL measurements with the time-resolved PL measurement. Remarkably, by combining both observations we find a tuning range of at least 20 meV for the PL emission of interlayer excitons due to the repulsive dipole-dipole interaction. As proposed by Butov *et al.* [But99] this energetic blueshift can be used to estimate a lower boundary of the maximum interlayer exciton density $n_{\mathrm{IEX}}$ by a basic plate capacitor model. However, according to Laikthman and Rapaport [Lai09] this approximation

is only valid if two conditions are met. First, the interlayer exciton density $n_{\mathrm{IEX}}$ has to be substantially smaller than the squared interlayer distance $d$, namely $n_{\mathrm{IEX}}d^2 \ll 1$. Second, the thermal wave vector $k_T$ of the IEX, given by $k_T = \sqrt{2Mk_bT}/\hbar$, where $M = m_e + m_h$ needs to be smaller than the inverse of the average exciton-exciton distance, therefore $(k_T)^2 \gg n_{IEX}$. Assuming a temperature of 4 K and $m_e = 0.56\,m_0$, $m_h = 0.35\,m_0$ ([Kor15]), we find $k_T \approx 10^6\,\mathrm{cm}^{-1}$. Returning to the plate capacitor formula, the density of interlayer excitons $n_{\mathrm{IEX}}$ can be written as [But99]:

$$n_{\mathrm{IEX}} = \frac{\Delta E_D \epsilon_r \epsilon_0}{4\pi e^2 d} \tag{4.4}$$

We assume $\epsilon_r = 4.5$ [Kum12], an interlayer distance $d = 1\,\mathrm{nm}$, and a power-induced energy shift $\Delta E_{\mathrm{D}} = 20\,\mathrm{meV}$, which corresponds to the maximum energy difference of the IEX peak position observed in the steady-state and time-resolved power-dependent measurements. Since the energy value in the time-resolved measurements is extracted 800 ps after excitation, it represents a conservative lower bound of the maximum blueshift. Provided these assumptions, we obtain $n_{\mathrm{IEX}} \approx 4 \cdot 10^{10}\mathrm{cm}^{-2}$ as a lower boundary of the interlayer exciton density in our PL experiments. This value also fulfills both conditions given by Laikthman and Rapaport [Lai09] since $n_{\mathrm{IEX}}d^2 \approx 4 \cdot 10^{-4} \ll 1$ and $(k_T)^2 \approx 10^{12}\,\mathrm{cm}^{-2} \gg 4 \cdot 10^{10}\mathrm{cm}^{-2}$.

In conclusion, the presented steady-state and time-resolved PL measurements illustrate the unusual physical properties of interlayer excitons. The multi-nanosecond lifetimes of the IEX at low temperatures are in stark contrast to the ultra-short lifetimes of excitons in monolayer TMDCs and follow from the increased electron-hole separation. As a function of excitation power and temperature, we observe unusual energetic shifts of the IEX PL emission, which also drastically differ from the behavior of excitons in monolayer TMDCs. It is shown that the main mechanisms behind these observations are the interlayer exciton diffusion in an inhomogeneous potential landscape combined with the dipolar repulsive interaction of interlayer excitons at elevated densities. An effective reduction of the observed disorder potential in our sample can be expected by applying novel fabrication techniques in future studies. One possibility to overcome this issue is the preparation of the sample in an inert atmosphere to prevent the inclusion of adsorbates [Cao15]. Alternatively, the sample can be protected from the environment by encapsulation in hexagonal boron nitride, an approach which will be discussed in more detail in chapter 5 for the case of monolayer $WS_2$.

## 4.4 Interlayer excitons in high magnetic fields

After studying the interaction effects and dynamics of interlayer excitons in the previous sections, we now turn to measurements of interlayer excitons under the influence of an out-of-plane magnetic field. Previous works on monolayer TMDCs demonstrated the lifting of the valley degeneracy by application of an external magnetic field, as it was discussed in section 2.4. Hence, magneto-PL can provide access to critical information of excitonic species such as the $g$ factor or the field-induced valley polarization, rendering a comparable study on interlayer excitons highly desirable. As we will see in the following, the AB stacking configuration of the studied heterostructure and the resulting intervalley transitions will have pronounced effects on the properties of interlayer excitons in an out-of-plane magnetic field. This section follows the presentation of [Nag17a], where the results were published. All data presented in this chapter were acquired at the HFML facility in Nijmegen (see section 3.1.2).

### 4.4.1 Magnetic splitting of intralayer excitons

We start our analysis on the evolution of the neutral exciton peak (X) of $WSe_2$ in a magnetic field. The established framework in this section for intralayer excitons will then be applied to our observations on interlayer excitons. Figure 4.18 shows a magnetic field series from 0 T to 30 T in 1 T steps of PL spectra taken on the area of the $WSe_2/MoSe_2$ heterostructure at a sample temperature of 4 K. As can be seen, the large spectral window of the PL spectra allows us to study the evolution of both interlayer and intralayer excitons simultaneously in an external magnetic field. Importantly, the sample is excited by a linearly polarized CW-laser ($\lambda = 640\,\text{nm}$), populating both valleys equally initially. The emitted PL is detected in a circularly polarized basis with $\sigma^-$ (Fig. 4.18(a)) and $\sigma^+$ (Fig. 4.18(b)) components.
The emission stemming from the neutral exciton X of $WSe_2$ is discernible at the right side of the polarization-resolved spectra. At $B = 0$, the peak energies are identical due to the valley degeneracy. For $B > 0$, the energy of the $\sigma^+$ transition decreases, whereas the energy of the $\sigma^-$ transition increases, giving rise to a finite valley splitting $\Delta E = E^{\sigma^+} - E^{\sigma^-}$ between the two transitions. This is further depicted in Fig. 4.19(a), where the extracted peak positions of both polarization components in detection are plotted in dependence of the magnetic field. The peak positions are obtained by using a Gaussian fit function. At the maximum field of 30 T, the valley splitting reaches a value of about 6.4 meV. This can also be seen in Fig. 4.19(b), where the extracted valley splitting as a function of magnetic field is presented. Clearly, the data follows a linear

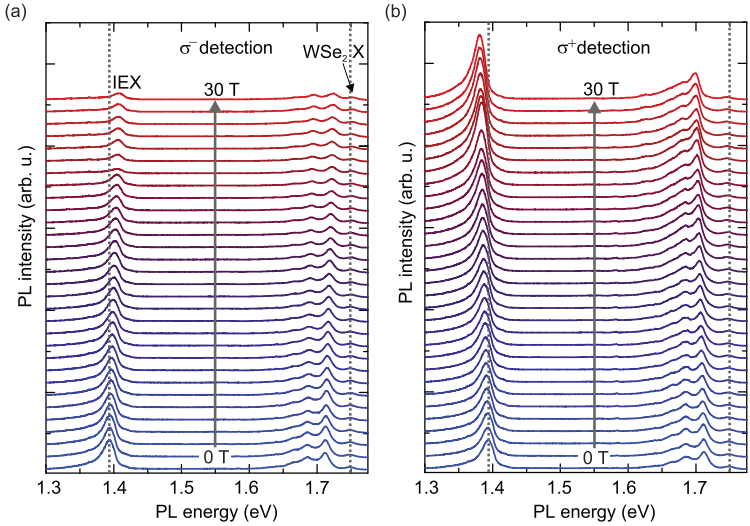


**Figure 4.18 |** Evolution of PL spectra taken on the $WSe_2/MoSe_2$ heterostructure at 4 K for magnetic fields between 0 T and 30 T in 1 T steps under linearly polarized excitation and (a) $\sigma^-$ polarized and (b) $\sigma^+$ polarized detection. The dashed lines indicate the spectral position of the interlayer exciton and the neutral exciton of $WSe_2$ at 0 T respectively.

trend as also indicated by the fit line in the plot. The respective $g$ factor can be deduced by resorting to equation 2.4 from section 2.4, which reads $\Delta E = E^{\sigma^+} - E^{\sigma^-} = g\mu_B B$. Using the slope of the linear fit we can extract a $g$ factor of the neutral exciton of $WSe_2$ of $-3.7 \pm 0.1$.

This value for the $g$ factor is in qualitatively good agreement to previous magneto-PL studies on monolayer $WSe_2$, which yielded values of $-4.37 \pm 0.15$ [Sri15], $-1.9 \pm 0.2$ [Aiv15], $-4.0 \pm 0.5$ [Mit15] and $-3.7 \pm 0.2$ [Wan15a] for the neutral exciton $g$ factor. To understand the magnitude of the magnetic coupling of monolayer TMDCs, we resort to a semiquantitative model, which describes the effects of an external out-of-plane magnetic field on the energy levels by three contributions, namely the spin, the atomic orbitals and the so-called valley magnetic moment [Aiv15, Sri15]. As shown in Fig. 4.20, the relevant optical transitions in monolayer $WSe_2$ take place between the conduction and valence band in the $K^+$ ($K^-$) valley, leading to $\sigma^+$ ($\sigma^-$) polarized emission in detection. Importantly, the optically allowed transitions considered here are valley conserving, due to the requirement of momentum conservation. This is further illustrated in the schematic Brillouin zone in Fig. 4.20.

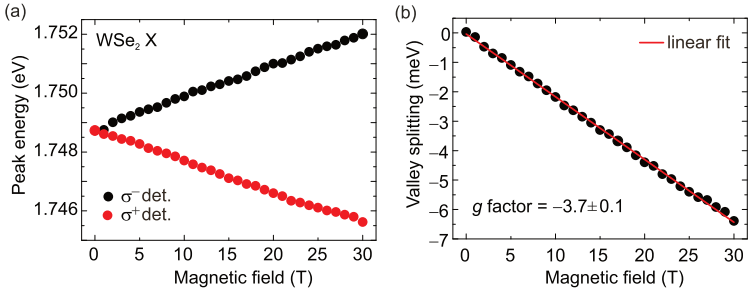


**Figure 4.19** | (a) Emission energies of the $\sigma^+$ and $\sigma^-$ transitions of the neutral exciton of $WSe_2$ in detection as a function of magnetic field. (b) Corresponding valley splitting in dependence of magnetic field. The solid red line indicates a linear fit to the data.

The dashed lines in Fig. 4.20 show the situation for $B = 0$. Here, the two optical transitions are energetically degenerate due to time-reversal symmetry. Consequently, we do not observe a valley splitting in this case in the experiment as evidenced in Fig. 4.19(b).

We now turn to the situation for $B > 0$ within the discussed framework. The first possible contribution to the energetic shift is the magnetic moment originating from the bare spin, which is given by $\Delta_S = 2s_z\mu_B B$ with $s_z = \pm\frac{1}{2}$. However, optical transitions in monolayer TMDCs are only allowed between states of the same spin. Hence, the Zeeman shift due to the magnetic moment from spin does not lead to a net energetic difference between the two transitions since the edges of the conduction and valence band shift equally, which can also be seen by the evolution of the black arrows, indicating the spin contribution, in Fig. 4.20. The second contribution to the overall energetic shift stems from the magnetic moment $m$ of the atomic orbitals (black-framed arrows in Fig. 4.20). Since the valence band edges are mostly $d$-orbitals with $m = 2$ in the $K^+$ valley and $m = -2$ in the $K^-$ valley, a total magnetic-field-dependent shift of $\Delta_O = -2\tau\mu_B B$ in the valence band results, where $\tau \pm 1$ is the index for the $K^\pm$ valley respectively. On the other hand, the conduction band edges are mostly composed of $d$-orbitals with $m = 0$ and therefore do not carry a magnetic moment from the atomic orbitals. As a result, by adding up the contributions from the valence bands in the $K^+$ and $K^-$ valley, we obtain an overall energetic splitting due the atomic orbital magnetic moment of $-4\mu_B B$. The third contribution results from the self-rotation of the Bloch wave packets, which gives rise to a magnetic moment, called the valley magnetic moment [Aiv15] (grey arrows in Fig. 4.20). As it was shown

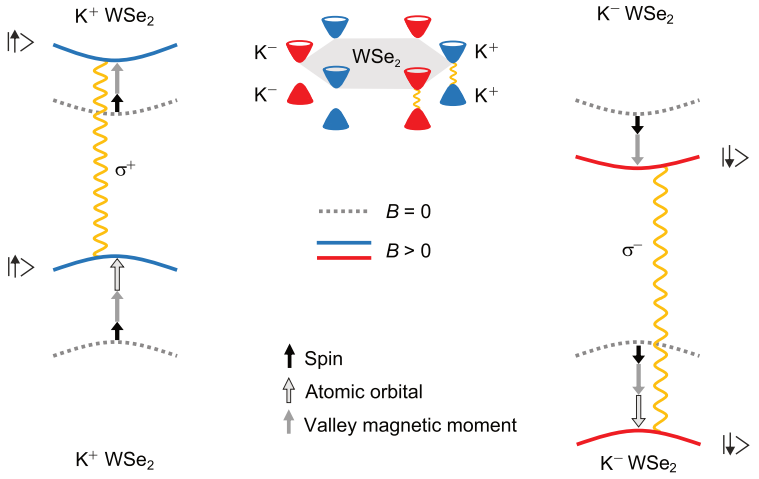


**Figure 4.20 |** Expected band evolution of monolayer $WSe_2$ in an out-of-plane magnetic field considering three different magnetic moments emerging from spin (black arrows), the atomic orbitals (black-framed) and the valley magnetic moment (grey). At $B = 0$ (dashed grey line), the energies between the different valleys are degenerate due to time-reversal symmetry. Arrows indicate spin-up and spin-down states. The schematic Brillouin zone depicts the optically relevant transitions, which take place between valleys of the same index. Figure based on the illustration from [Aiv15].

for the case of monolayer graphene [Xia07] and later extended to monolayer TMDCs [Xia12], a finite value of the so-called Berry curvature $\Omega(k)$, i.e. $\Omega(k) \neq 0$, implying a self-rotation of the Bloch wave packet at a wave vector $k$, leads to a magnetic moment $m_\tau$. The sign of this valley magnetic moment depends on the respective valley due to the broken inversion symmetry in the monolayer case [Yao08]. In the low-energy limit, the valley magnetic moment for the conduction- and valence band edges can be written as $m_{\tau,i} = \frac{m_0}{m_i}\tau\mu_B$, where $m_i$ is the effective mass of electrons ($i = e$) in the conduction band and holes ($i = h$) in the valence band [Aiv15]. As a result, the energetic splitting due to the valley magnetic moment $\Delta_V$ is defined as $\Delta_V = -\tau\mu_B \left(\frac{m_0}{m_e} - \frac{m_0}{m_h}\right) B$. In a monolayer TMDC, the valley magnetic moments in the conduction and valence band have the same orientation since the optical transitions are valley conserving. Therefore, a finite splitting $\Delta_V$ only emerges in the case of unequal effective masses of electrons and holes.

At this point, the two relevant contributions from the atomic orbitals and the valley magnetic moment can be summarized to the total expected energetic splitting $\Delta E^{1L}$

in a monolayer TMDC, as follows:

$$\Delta E^{1L} = E^{\sigma^+} - E^{\sigma^-} = -\left(4 - 2\left(\frac{m_0}{m_e} - \frac{m_0}{m_h}\right)\right)\mu_B B. \tag{4.5}$$

In a basic scenario, we can assume $m_e \approx m_h$ for the effective masses in a monolayer TMDC, leading to an expected field-induced magnetic shift of a monolayer TMDC of $\Delta E^{1L} \approx -4\mu_B B$. The value of $-4$ for the $g$ factor based on these theoretical considerations is in good agreement to our experimental observation of $g = -3.7 \pm 0.1$ of monolayer $WSe_2$. Taking calculated effective masses for electrons ($m_e = 0.28\, m_0$) and holes ($m_h = 0.36\, m_0$) in monolayer TMDCs from the $k \cdot p$ calculations by Kormányos *et al.* [Kor15], we obtain an estimated $g$ factor of about $-2.4$, in larger deviation to our experimental observation.

We conclude here that the observed $g$ factor of $-3.7 \pm 0.1$ from the intralayer neutral excitonic resonance of monolayer $WSe_2$ on the studied $WSe_2/MoSe_2$ heterostructure is generally in line with recent reports, which studied a bare $WSe_2$ monolayer system [Sri15, Aiv15, Mit15, Wan15a]. By using the proposed model system from the literature, which describes the energetic splitting by taking into account three contributions of the magnetic moment, reasonable agreement can be achieved between experiment and theory by assuming equal effective masses of electrons and holes. However, stronger deviations between the experimental and theoretical $g$ factor emerge if we resort to calculated effective masses for electrons and holes. One possibility to improve the agreement is to calculate the valley magnetic moment for a finite momentum spread of the exciton in $k$-space as proposed by Srivastava *et al.* [Sri15]. The strong spatial confinement of excitons in monolayer TMDCs ($a_B \sim 1\,\mathrm{nm}$) translates into a considerable momentum spread on the order of $\sim \hbar/a_B$. By calculating the valley magnetic moment within this larger $k$-space extension of the exciton, the authors were able to theoretically adjust the $g$ factor to the one obtained in the experiment.

### 4.4.2 Giant magnetic splitting, near-unity valley polarization and dynamics of interlayer excitons

We now turn to the polarization-resolved PL measurements of the interlayer exciton in an out-of-plane magnetic field up to 30 T. The evolution of the interlayer exciton for both polarizations can be seen on the left side of the spectra in Fig. 4.18(a) and (b) respectively and in more detail in Fig. 4.21(a). Here, the intensity of the $\sigma^+$ and $\sigma^-$ polarized emission components of the IEX is plotted on a logarithmic scale for clarity.

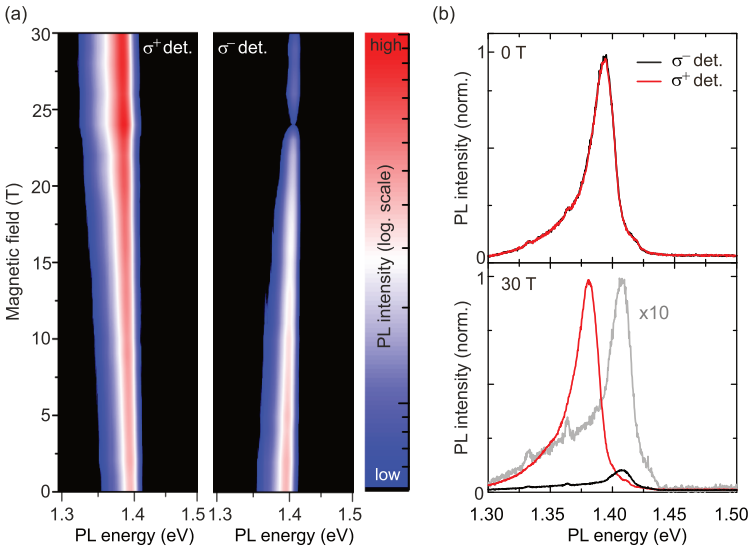


**Figure 4.21 |** (a) False-color illustration of the $\sigma^+$ and $\sigma^-$ polarized emission of the interlayer exciton PL as a function of the out-of-plane magnetic field up to 30 T. The sample is excited with linearly polarized light. The PL intensity is plotted on a logarithmic scale to improve the clarity of the presentation. (b) Comparison of polarization-resolved PL spectra of the interlayer exciton at 0 T and 30 T. The emission from both polarizations is identical at 0 T due to the valley degeneracy. At 30 T, the degeneracy is lifted, leading to a pronounced peak splitting of about 26 meV and a strongly polarized emission stemming almost exclusively from the $\sigma^+$ transition.

In analogy to the intralayer transition of $WSe_2$ in the previous section, the energy of the $\sigma^+$ polarized component decreases monotonically, while it increases for the $\sigma^-$ polarized transition for rising magnetic fields. Furthermore, we observe a strong dependence of the interlayer exciton PL intensity on the detected polarization in the magnetic field.

As can be seen in Fig. 4.21(a), the intensity of the $\sigma^-$ transition is suppressed with increasing magnetic field whereas it drastically increases for the $\sigma^+$ component. To further illustrate our observations, Fig. 4.21(b) shows polarization-resolved PL spectra of the interlayer exciton for the two limiting cases of the experiment, $B = 0\,\mathrm{T}$ and $B = 30\,\mathrm{T}$. Due to the linearly polarized excitation, the two circularly polarized emission peaks are of same energy and intensity for $B = 0\,\mathrm{T}$, as both degenerate valleys are populated equally. For $B = 30\,\mathrm{T}$, however, the energy splitting between the two valley configurations amounts to about 26 meV, exceeding the splitting of about 6.4 meV of the neutral exciton of $WSe_2$ by far. Moreover, the PL emission from the interlayer exciton at high fields stems almost exclusively from the $\sigma^+$ transition, while the emission from the $\sigma^-$ transition is strongly suppressed.

To further analyze the data, we extract the peak positions of the interlayer exciton for both polarizations by a Gaussian fit function and calculate the resulting valley splitting $\Delta E^{\mathrm{IEX}} = E^{\sigma^+} - E^{\sigma^-}$, which is shown in Fig. 4.22(a).

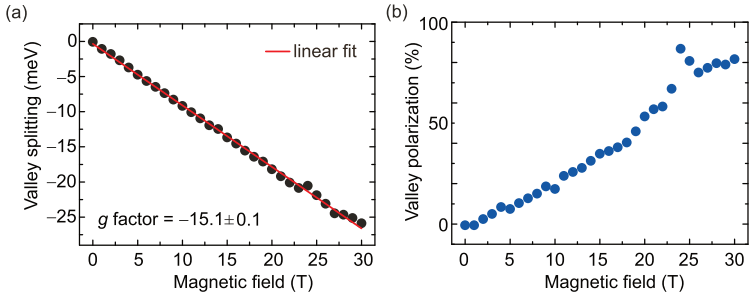


**Figure 4.22 |** (a) Valley splitting of the interlayer exciton as a function of magnetic field. The red solid line is a linear fit to the data, corresponding to a $g$ factor of the interlayer exciton of $-15.1 \pm 0.1$ (b) Magnetic-field induced valley polarization of the interlayer exciton.

Clearly, the valley splitting of the interlayer exciton follows a linear trend with increasing magnetic field, allowing us to deduce a $g$ factor of the interlayer exciton, $g^{\mathrm{IEX}} = -15.1 \pm 0.1$ by fitting the data using the linear relation $\Delta E^{\mathrm{IEX}} = E^{\sigma^+} - E^{\sigma^-} = g^{\mathrm{IEX}} \mu_B B$. The field-induced degree of valley polarization of the interlayer exciton, defined by $P = (I_{\sigma^+} - I_{\sigma^-})/(I_{\sigma^+} + I_{\sigma^-})$ is presented in Fig. 4.22(b). As also visible in Fig. 4.21(b), it is strictly zero for $B = 0\,\mathrm{T}$ and reaches values of more than 80 % for the highest fields up to 30 T. Given the fact that both valleys are initially equally populated, such an overall high degree of field-induced polarization is particularly remarkable. We note here that at a magnetic field of around 24 T, both the valley splitting and the

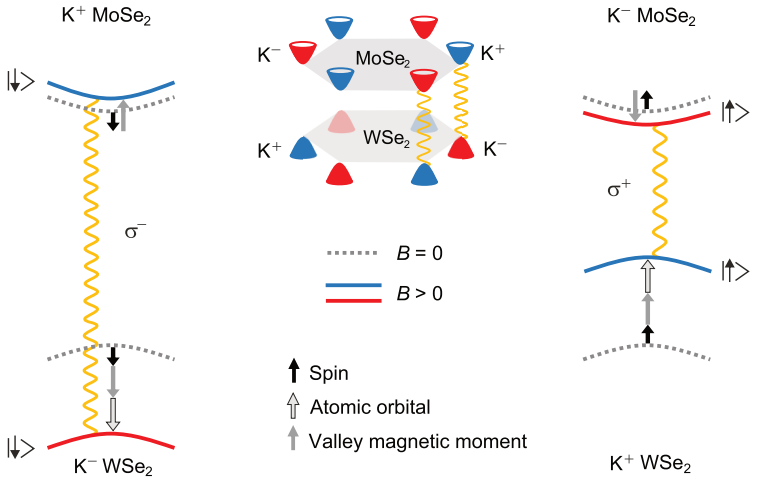


**Figure 4.23** | Expected evolution of the transitions of the interlayer exciton in an AB-stacked $WSe_2/MoSe_2$ heterostructure with positive applied magnetic field taking into account three different magnetic moments emerging from spin (black arrows), the atomic orbitals (black-framed) and the valley magnetic moment (grey). The dashed lines show the situation for $B = 0$ T. The schematic Brillouin zone depicts the optically allowed inter-valley transitions of interlayer excitons in an AB-stacked heterostructure.

field-induced valley polarization show a slightly anomaly, which will be discussed in more detail later in the chapter.

Intriguingly, the determined value of the interlayer exciton $g$ factor of $-15.1 \pm 0.1$ strongly deviates from typical $g$ factors of excitons in monolayer TMDCs, which are mostly found to be around $-4$, as also evidenced in the previous section for the case of the neutral exciton of monolayer $WSe_2$. In the following, we show that this anomalously high $g$ factor of the interlayer exciton can be understood within the same framework as discussed for monolayer systems. As we will see, the spin-allowed intervalley transitions of the interlayer exciton in the studied AB-stacked heterostructure are largely responsible for this intricate phenomenon.

The pertinent theoretical framework is depicted in Fig. 4.23. As indicated by the schematic Brillouin zone, and as also discussed in section 4.2.3, the optically allowed transitions of interlayer excitons in an AB-stacked heterostructure take place between valleys of different index, for instance between the conduction band in the $K^+$ valley of $MoSe_2$ and the valence band in the $K^-$ valley of $WSe_2$. Both the magnetic moments stemming from spin and the atomic orbitals behave identically for intra- and interlayer

excitons. The optical transitions of interlayer excitons are spin-conserving between the conduction and valence band. Hence, the spin magnetic moment does not contribute to the energetic splitting of the respective resonances (see parallel evolution of the black arrows in Fig. 4.23). In the same vein, the magnetic moments from the atomic orbitals are zero in the conduction band and $m = 2$ for the $K^+$ valley and $m = -2$ for the $K^-$ valley, leading to an overall splitting between the valley-selective transitions of $-4\mu_B B$ based on these two contributions. The valley magnetic moment, however, behaves strikingly different in an AB-stacked heterostructure in comparison to a monolayer system. As we saw in the previous section, it is defined by $m_{\tau,i} = \frac{m_0}{m_i}\tau\mu_B$ and its sign consequently depends on the index of the valley. In the case of a monolayer TMDC, the optical transitions are valley-conserving. Thus, the valley magnetic moments of conduction and valence band have the same sign and only contribute to the overall energy shift, if the effective masses of electrons and holes are different (see Fig. 4.20). In stark contrast to that, the optical transitions of interlayer excitons in an AB-stacked heterostructure take place between valleys of different index. Therefore, the contributions from the valley magnetic moment have the opposite sign for the conduction and valence bands and consequently add up, as can be seen by the grey arrows in Fig. 4.23. This antiparallel evolution of the valley magnetic moments is the main magnetic property of interlayer excitons in an AB-stacked heterostructure. As can be derived from Fig. 4.23, it leads to a strong increase (decrease) of the $\sigma^-$ ($\sigma^+$) transition energy in a positive applied magnetic field and consequently to a larger $g$ factor in comparison to the monolayer system. We can quantify the expected total valley-selective splitting of the interlayer exciton $\Delta E^{\mathrm{IEX}}$ with the same formalism as in the previous section, taking into account the different signs of the valley magnetic moments:

$$\Delta E^{\mathrm{IEX}} = E^{\sigma^+} - E^{\sigma^-} = -\left(4 + 2\left(\frac{m_0}{m_e} + \frac{m_0}{m_h}\right)\right)\mu_B B. \tag{4.6}$$

Inserting calculated values for the effective masses of electrons in the upper conduction band of $MoSe_2$ ($m_e = 0.57\,m_0$) and the valence band of $WSe_2$ ($m_h = 0.36\,m_0$) by Kormányos *et al.* [Kor15] we obtain $g^{\mathrm{IEX}} = -13.1$ for the $g$ factor of the interlayer exciton based on the proposed model system in close agreement with the value from the experiment of $g^{\mathrm{IEX}} = -15.1 \pm 0.1$. Hence, the peculiar momentum space configuration in an AB-stacked heterostructure, which is not attainable in a pure monolayer system, gives rise to a drastic increase of the $g$ factor.

The external out-of-plane magnetic field can also be used to manipulate the PL lifetime of the interlayer exciton. Figure 4.24 shows PL decay traces of the interlayer exciton

for 0 T and 28 T on a logarithmic scale, which are obtained by resorting to a pulsed laser diode ($\lambda = 690$ nm), which is synchronized to an avalanche photodiode. In this measurement, the sample is excited linearly and analyzed without polarized detection.

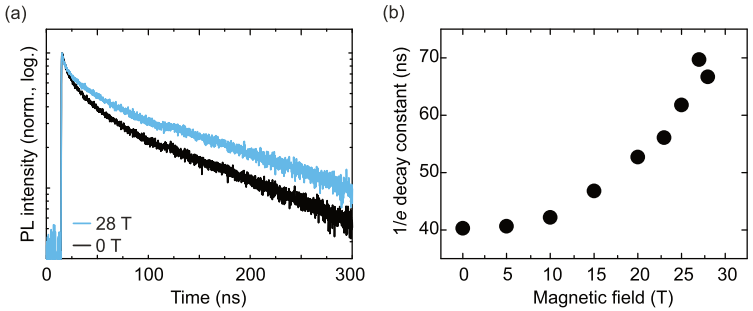


**Figure 4.24 |** (a) Time-resolved PL traces of the interlayer exciton at $B = 0$ T and $B = 28$ T. (b) $1/e$ decay constant of the interlayer exciton PL decay as a function of magnetic field.

It is worth mentioning at this point that due to the strong field-induced valley polarization of the interlayer exciton (see Fig. 4.22(b)), the PL decay observed at 28 T is strongly $\sigma^+$ polarized. Applying an external magnetic field therefore allows us to create valley-polarized interlayer excitons, which are sustainable over hundreds of nanoseconds. Clearly, the lifetime of the interlayer exciton PL increases with rising magnetic field strength. This is further illustrated in Fig. 4.24(b), where the $1/e$ decay constant of the interlayer exciton PL is plotted against the applied external magnetic field. As can be seen, the lifetime of the interlayer exciton can be increased from 40 ns at $B = 0$ T to about 70 ns at the highest fields. We can possibly understand this observation in the context of earlier studies on GaAs-AlGaAs quantum wells [But98, But99], which discussed the effects of an external magnetic field on the radiative recombination dynamics of interlayer excitons. The application of an out-of-plane magnetic field leads to an increasing effective mass of the interlayer exciton, implying a reduced localization area in real space. The resulting smaller wave function overlap then leads to a lower oscillator strength of the interlayer exciton and consequently to longer recombination times.

After providing a reasonable model system to understand the high $g$ factors of interlayer excitons in the studied heterostructure and discussing the influence of the magnetic field on the PL lifetimes, we now briefly revisit the already mentioned slight anomaly in the data in Fig. 4.22. As can be seen, both the energetic splitting and the field-induced valley polarization deviate from the overall trend at a magnetic field of around

$B = 24\,\mathrm{T}$. With a high certainty, we can exclude external factors from the setup such as an instability of the magnet at a certain field for two reasons. First, the observed effect could be reproduced during various measurement runs with different excitation conditions, and also for several samples in subsequent visits to the HFML. Second, no similar deviation of the data was observed for the other excitonic features stemming from the monolayer systems during the same measurement, which can be seen for instance in the data of Fig. 4.19 for monolayer $WSe_2$.
One possible scenario to explain this effect could be a level crossing of the two spin-split conduction bands of $MoSe_2$ at a certain magnetic field. This could either imply a crossing of the bands within the same valley or an inter-valley crossing of the lower conduction band of the $K^+$ valley with the higher conduction band of the $K^-$ valley of $MoSe_2$. The expected evolution of both conduction bands in $MoSe_2$ in an out-of-plane magnetic field is shown in Fig. 4.25.

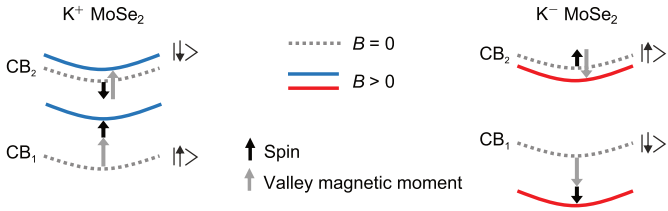


**Figure 4.25 |** Expected band evolution of the two spin-split conduction bands ($CB_1$ and $CB_2$) in monolayer $MoSe_2$ with positive applied magnetic field. The shift of the energy levels by an out-of-plane magnetic field results from the magnetic moment of spin (black arrows) and the valley magnetic moment (grey arrows). The indicated energetic shifts are not to scale with respect to the size of the conduction band splitting.

We can neglect the contribution from the atomic orbital magnetic moment as the conduction bands mostly comprise of $d$-orbitals with $m = 0$. An intra-valley crossing of the conduction bands would occur if the energetic separation of both bands in either the $K^+$ or $K^-$ valley reaches a value near 0. This is not possible for the conduction band in the $K^-$ valley since the overall splitting increases at a positive magnetic field, as visible in Fig. 4.25. For the $K^+$ valley, the splitting decreases in a positive magnetic field and the field-induced change can be written as $\Delta E_{\mathrm{intra}} = 2 s_z \mu_B B + 2 s_z \mu_B B$. At $B = 24\,\mathrm{T}$ this yields a decrease of the splitting of about $\Delta E_{\mathrm{intra}} \approx 2.8\,\mathrm{meV}$. To calculate a possible inter-valley crossing between the upper conduction band in the $K^-$ valley and the lower conduction band in the $K^+$ valley, we only need to consider the energetic contribution from the valley magnetic moments, as the spin contributions cancel out.

We can then write the field-induced change at $B = 24\,\mathrm{T}$ as $\Delta E_{\mathrm{inter}} = 2\frac{m_0}{m_e}\mu_B B$ which results in $\Delta E_{\mathrm{inter}} \approx 4.9\,\mathrm{meV}$ given $m_e = 0.57\,m_0$ from Kormányos *et al.* [Kor15].
However, the conduction band splitting of $MoSe_2$ was found to be in the range of 20 – 30 meV by theoretical and experimental works as shown in Tab. 2.1, exceeding both the values of $\Delta E_{\mathrm{intra}} \approx 2.8$ meV and $\Delta E_{\mathrm{inter}} \approx 4.9\,\mathrm{meV}$ at $B = 24\,\mathrm{T}$ by far. Based on these considerations, we can rule out a level crossing in the conduction band of $MoSe_2$ as the reason for the anomalous peak in our data. Thus, further studies are necessary to elucidate the origin of this peculiar feature.
Overall, the presented magneto-PL measurements on the studied $WSe_2/MoSe_2$ heterostructure illustrate the remarkable physical properties of interlayer excitons in a van der Waals heterostructure. Most importantly, the AB stacking of the heterostructure enables optically allowed inter-valley transitions, which are not accessible in monolayer systems. In such a configuration, the contributions from the valley magnetic moment add up, resulting in a strong enhancement of the overall magnetic response. As a consequence, the experimentally determined $g$ factor of the interlayer exciton of $-15.1 \pm 0.1$ by far exceeds the $g$ factor of the neutral exciton of $WSe_2$ ($-3.7 \pm 0.1$) that we could observe in the same experiment. At the same time, the ultra-long lifetimes, combined with the large $g$ factor, lead to a pronounced field-induced valley polarization of the interlayer exciton, reaching near-unity values for the highest fields around 30 T. The lifetime of the interlayer exciton could be almost doubled by the application of an external magnetic field, giving rise to strongly polarized emission at high magnetic fields. Hence, AB-stacked TMDC heterostructures provide a unique platform to access novel optical transitions between valleys of different index and to engineer significantly higher $g$ factors as compared to excitons in monolayer systems.

Chapter 5

# Biexcitons in hBN-encapsulated monolayer $WS_2$

## 5.1 Introduction

The previous chapter reported new insights on interlayer excitons in heterostructures consisting of two different TMDCs. In this chapter, we will study another fascinating type of excitons accessible in van der Waals heterostructures, namely biexcitons that emerge from an hBN-encapsulated monolayer of $WS_2$. As already briefly outlined in section 2.2, several experimental works have observed biexciton emission in monolayer TMDCs. From a fundamental point of view, these many-body states are of particular interest due to their cascaded photon emission, which is accompanied by entangled photon generation [Ben00, You06, He16a]. Consequently, biexcitons could possibly serve as a testbed for future quantum optics experiments. Nevertheless, several key questions with respect to the nature of this many-body state are open. A very important aspect in this respect is the composition of biexcitons in momentum space. As will be specified later in this chapter, the valley-contrasting band structure in monolayer TMDCs allows a variety of possible biexciton configurations, where the prevalent composition is not clear a priori.

However, more detailed spectroscopic studies on biexcitons in TMDCs answering these questions can be strongly impeded by the large spectral linewidth of this feature. As an example, Fig. 5.1(a) shows the first observation of biexciton emission in monolayer $WS_2$, which was reported by Plechinger *et al.* [Ple15]. As can be seen in Fig. 5.1(b), a biexciton feature (XX) with a characteristic superlinear emission dependence (see section 2.2) clearly emerges for high excitation densities. However, the peak is only

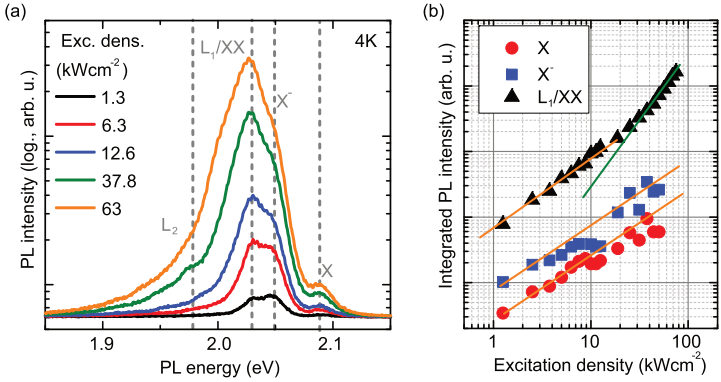


**Figure 5.1** | (a) Power-dependent PL spectra on monolayer $WS_2$ at a sample temperature of 4 K. (b) Double-logarithmic representation of the integrated PL intensities of the exciton (X), the trion ($X^-$) and the $L_1$/XX peak. The orange (green) solid lines indicate a linear (quadratic) dependency on the excitation density. Both figures taken and slightly adapted from [Ple15].

visible as a shoulder of the overall PL signal and thus spectrally not separated from the other excitonic features. Given these unfavorable spectroscopic properties, this sample system is not very suitable for more advanced studies of biexcitons in TMDCs, such as magneto-PL, which require the resolution of subtle energetic shifts.

A highly promising approach to overcome these issues is provided by the encapsulation of the monolayer TMDC between two thin sheets of hBN. This method was first pioneered for monolayer graphene, where it could be shown that the encapsulation with hBN results in a strongly increased mobility of graphene in transport measurements [Dea10]. Recently, the concept of encapsulation was successfully transferred to monolayer TMDCs as evidenced by several experimental spectroscopic studies [Wan16b, Cad17, Aja17, Man17, Wie17, Wan17b]. Figure 5.2 shows representative data by Cadiz *et al.* [Cad17], where the influence of hBN-encapsulation on optical spectra of the four most prominent TMDCs at a sample temperature of 4 K is examined.

In the upper panel, the monolayer TMDC is placed on $SiO_2$, whereas in the lower panel it is encapsulated with hBN. It could be consistently observed that the inhomogeneous broadening of the spectral line is strongly reduced by the surrounding hBN, resulting in linewidths of excitonic features down to 1.5 meV in monolayer $MoSe_2$ [Shr18]. In this situation, the linewidth of the peak approaches the limit of homogeneous broadening and is thus mostly determined by the radiative lifetime of the respective optical transi-

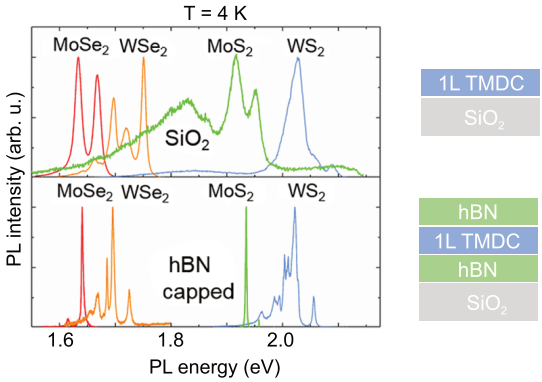


**Figure 5.2 |** Low-temperature PL spectra for monolayer TMDCs on a $SiO_2$ substrate (upper panel) and hBN-encapsulated monolayer TMDCs (lower panel). The encapsulation with hBN leads to a drastic reduction of the spectral linewidth of all excitonic feature. Figure taken and adapted from [Cad17].

tion. So far, the underlying mechanisms for the favorable impact of hBN-encapsulation on the optical properties of TMDCs are not fully understood. Possible contributions arise from the fact that the TMDC is protected from detrimental doping and local electric field fluctuations from the substrate [Cad17].

In this chapter, we will use an hBN-encapsulated monolayer of $WS_2$ as a platform to study the optical properties of biexcitons with hitherto inaccessible spectral quality. The linewidth of the observed superlinear biexciton feature is drastically reduced by the encapsulation and reaches values of less than 5 meV at low temperatures. The assignment of the biexcitonic emission in the sample is further supported by temperature-dependent and time-resolved PL measurements. Following the initial optical characterization, the well-separated biexciton peak allows us to study the energetic evolution of this many-body state in an out-of-plane magnetic field for the first time. The observed peculiar polarization behavior of the biexciton strongly deviates from the exciton peak and can be explained by taking into account the Zeeman contributions from all excitonic constituents. Most importantly, our analysis provides direct insight on the hybrid bright-dark momentum space configuration of this many-body state in monolayer $WS_2$. This part of the work has been published in [Nag18].

## 5.2 Sample structure and optical characterization

In this section the fabrication of the sample under study and the subsequent optical characterization will be presented. Power-dependent steady-state PL measurements reveal the emergence of spectrally narrow biexciton emission in the region of the van der Waals heterostructure. This attribution is further corroborated by a temperature-dependent steady-state PL study and time-resolved PL measurements.

### 5.2.1 Encapsulation of monolayer $WS_2$ with hBN

In order to encapsulate a monolayer of $WS_2$ with thin flakes of hBN ($\approx 10-20\,\mathrm{nm}$), we again utilize the PDMS transfer approach (section 3.2), as it was also performed to fabricate the $WSe_2/MoSe_2$ heterostructure in chapter 4. All experimental studies presented in this chapter were conducted on the sample shown below. Figure 5.3 shows the step-by-step procedure of the encapsulation. As a first step, a thin layer of hBN, which was initially exfoliated on a PDMS film, is transferred onto the $SiO_2$ wafer (Fig. 5.3(a)). The bulk hBN crystal itself was provided by the group of Kenji Watanabe and Takashi Taniguchi from the National Institute for Materials Science in Japan.

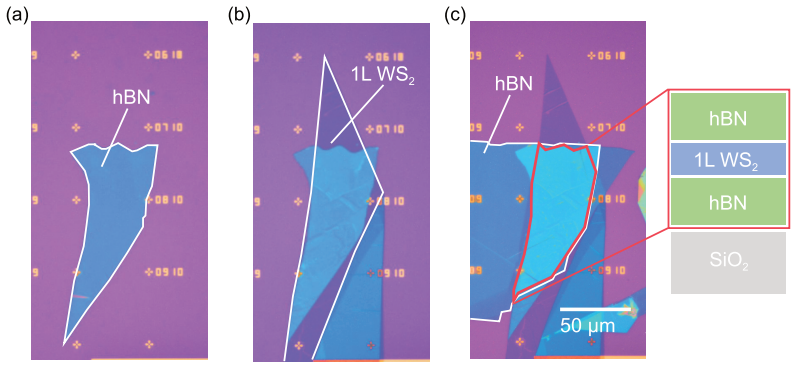


**Figure 5.3 |** Fabrication process of an hBN-encapsulated monolayer $WS_2$. (a) Thin sheet of hBN on a $SiO_2$ substrate after transfer from the PDMS film, serving as the lower layer for the encapsulation. (b) Monolayer $WS_2$ after transfer onto the thin sheet of hBN. (c) Completed heterostructure, where the upper thin sheet of hBN was placed on top of the structure from (b). The red-framed area marks the region, where the monolayer $WS_2$ is fully encapsulated by hBN.

Next, a monolayer of $WS_2$ is transferred on top of the underlying hBN sheet, as shown in Fig. 5.3(b). In the final step, the second thin sheet of hBN is transferred on top

of the two underlying layers, resulting in an encapsulation of the monolayer $WS_2$ in the red-framed area of Fig. 5.3(c). For this sample, no annealing was required to enhance the coupling between the layers since it provided high spectral quality right after fabrication (see section 5.2.2).

### 5.2.2 Identification of biexciton emission

After the successful fabrication of the hBN-encapsulated $WS_2$ monolayer, we now optically study the sample by power-dependent steady-state PL measurements. Figure 5.4 shows steady-state PL spectra at a sample temperature of 4 K for two different excitation powers (100 µW and 1000 µW) on the heterostructure using a CW-laser with a photon energy of 2.21 eV.

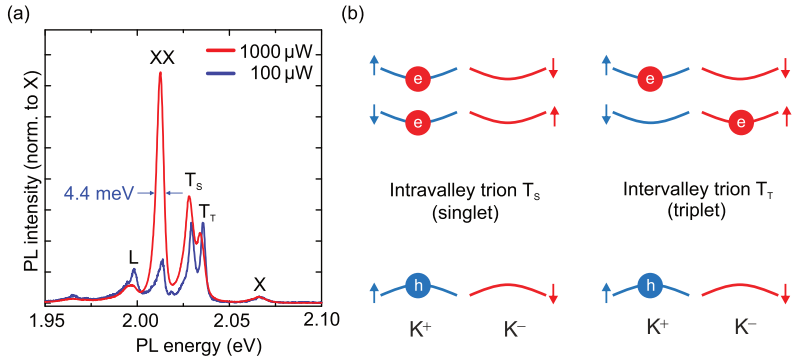


**Figure 5.4 |** (a) Steady-state PL spectra on the heterostructure at 4 K for 100 µW (blue) and 1000 µW (red) excitation power. Both spectra are normalized to the PL intensity of the neutral exciton (X). (b) Schematic illustration of the two different trion configurations (singlet and triplet) that can arise in $WS_2$ in the $K^+$ valley. The situation for the $K^-$ valley follows from time-reversal symmetry (not shown here).

Remarkably, the linewidth of all excitonic features is drastically reduced for both excitation powers in comparison to typical low-temperature spectra of $WS_2$ without hBN-encapsulation (see Fig. 5.1). This observation is in very good agreement with recent reports on hBN-encapsulated TMDC monolayers, as previously discussed in the introduction of this chapter, and is a direct evidence for the favorable quality of our sample. We first focus our analysis on the PL spectrum in Fig. 5.4(a) that is obtained with an excitation power of 100 µW (blue line). At an energy of 2.067 eV, we can identify the emission stemming from the neutral exciton (X) and at energies of 2.030 eV and

2.036 eV we observe a splitting of the trion emission, due to the formation of two different trion species $T_S$ and $T_T$. Such a trion fine structure has been previously observed in $WSe_2$ [Jon15, Cou17] and $WS_2$ [Ple16c] monolayers and arises from the peculiar conduction band structure in tungsten-based monolayer TMDCs. As schematically depicted in Fig. 5.4(b) for the case of the $K^+$ valley, the bright neutral exciton state consists of a hole from the highest valence band and an electron from the upper conduction band. With respect to the trion, the residual electron can be either situated in the same valley as the exciton forming a singlet state ($T_S$) or in the other valley resulting in a triplet configuration ($T_T$). The energetic splitting between these two states results from the intervalley Coulomb exchange interaction of the residual electron in the case of the triplet trion. Here, all three constituent particles possess the same spin orientation, thus rendering this configuration energetically more unfavorable. Recent theoretical calculations predict a value for the trion splitting induced by the exchange interaction for the closely related monolayer $WSe_2$ of around 6 meV [Yu14a], which is in excellent agreement to our observation. Additionally, at an energy of 1.998 eV, we observe emission which is usually attributed to the recombination of carriers localized at defects (L) [Ple15].

We now turn to the spectrum in Fig. 5.4(a), which is acquired with an excitation power of 1000 µW (red line). Importantly, both spectra in Fig. 5.4 are normalized to the respective intensity of the neutral exciton X. The PL intensity of both trion emission features scales mostly like the intensity of the exciton and the intensity of the defect state L saturates in relation to the neutral exciton, as expected for higher excitation densities. Most importantly, we observe a novel feature emerging at an energy of 2.012 eV at this excitation power. Compared to the other excitonic emission peaks, the peak clearly exhibits a superlinear behavior. At this point, we attribute this peak to the emission of biexcitons (XX), following very similar observations in recent literature for $WSe_2$ [You15] and $WS_2$ [Ple15, Sha15]. The ultra-narrow linewidth of the biexciton of 4.4 meV clearly demonstrates the positive effects of the hBN-encapsulation on the overall spectral quality. The binding energy of the biexciton, which can be determined as the energetic difference between the X and XX features, amounts to about 55 meV. While variational calculations by You *et al.* [You15] theoretically provide binding energies of biexcitons in the range of 50 – 60 meV and are thus in very good agreement to our observation, several recent theoretical calculations predict much lower values for the biexciton binding energy of around 20 meV [Zha15b, Kyl15, Szy17]. A possibility to resolve this apparent discrepancy is given by attributing the observed feature to a charged biexciton within an alternative scenario, which will be elaborated in section 5.4.

Nevertheless, for the moment we will continue by assuming a charge-neutral biexciton (XX).

Further insight on the specific intensity increase of the biexciton peak is given in Fig. 5.5(a), where spectra normalized to the PL intensity of the respective maximum peak for different excitation powers are shown. Clearly, one can observe that the intensity of the biexciton feature grows superlinearly with respect to the other excitonic peaks.

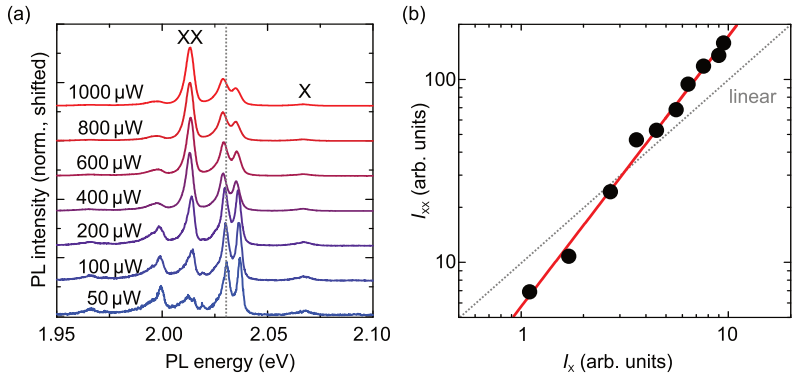


**Figure 5.5 |** (a) Power-dependent PL spectra for excitation powers from 50 – 1000 µW at 4 K. The spectra are normalized for each excitation power to the peak with the highest PL intensity. The dashed line indicates the energetic position of the singlet trion at 50 µW. (b) Intensity of the biexciton (XX) as a function of the intensity of the neutral exciton (X) on a double logarithmic representation. The dashed line depicts a linear relation between the two intensities. The red line represents a power law fit with $I_{XX} \sim (I_X)^{\alpha}$ with $\alpha = 1.48$.

This is further depicted in Fig. 5.5(b), where the intensity of the biexciton ($I_{XX}$) is brought into relation with the intensity of the neutral exciton ($I_X$) by a power law of the form $I_{XX} \sim (I_X)^{\alpha}$, see section 2.2. Here, a linear relation between the two intensities ($\alpha = 1$) is indicated by the grey dashed line. Fitting the data yields a value for $\alpha$ of 1.48. Based on a rate equation model for the exciton and the biexciton and assuming full thermal equilibrium between the two states, one would expect a strictly quadratic dependency of the biexciton emission ($\alpha = 2$) [Kim94]. However, recent experiments on biexcitons in monolayer TMDCs have regularly observed values for $\alpha$ smaller than 2, which was attributed to a lack of full equilibrium between the two states [You15, He16b, Kim16].

The observation of a superlinear evolution of the PL intensity with rising excitation power is already a very strong hint that the feature at an energy of 2.012 eV in the spectrum has a biexcitonic origin. This assessment is further strengthened by

a temperature-dependent PL series at high excitation power, as shown in Fig. 5.6(a). Here, using an excitation power of 400 µW, we track the evolution of the PL spectra from a sample temperature of 4 K to 100 K. The XX peak is discernible up to a temperature of 100 K, which allows us to clearly separate this feature from low-energetic defect states (L). As can be seen in the temperature series, the emission from the defect states completely vanishes for temperatures higher than 60 K due to their small activation energy, in line with similar temperature-dependent PL studies on monolayer TMDCs [Ple15, Wan14, God16, Hua16].

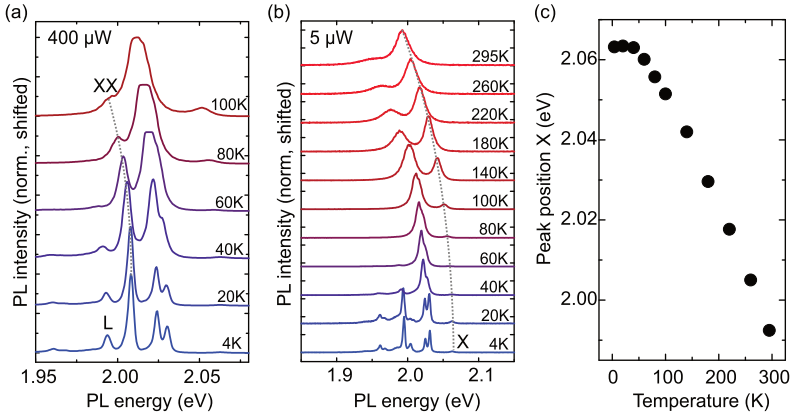


**Figure 5.6 |** (a) Temperature-dependent PL spectra from 4 K to 100 K for an excitation power of 400 µW. The dashed line indicates the energetic position of the XX feature. (b) Temperature-dependent PL spectra from 4 K to 295 K for an excitation power of 5 µW. The dashed line indicates the energetic position of the X peak. (c) Energetic peak position of the neutral exciton as a function of temperature.

Figure 5.6(b) illustrates a PL temperature series with an excitation power of 5 µW from 4 K to 295 K. While we cannot observe the XX feature due to the low excitation density regime, this series allows us to track the spectral evolution of the neutral exciton X over the whole temperature range. The respective peak position of X as a function of temperature is plotted in Fig. 5.6(c). Later in this chapter, we will use this data to roughly estimate the power-induced heating of the crystal lattice.

### 5.2.3 Time-resolved dynamics of biexcitons

The presented power-dependent steady-state PL measurements of the hBN-encapsulated $WS_2$ monolayer in the previous section have allowed us to confirm the emergence of a

spectrally narrow biexciton feature. To further examine the biexciton state, we now investigate its dynamics by time-resolved PL. The measurements are conducted with the streak camera system in Regensburg combined with the same pulsed laser system as in chapter 4 (pulse length 180 fs, photon energy 2.21 eV, repetition rate 80 MHz). In Figs. 5.7(a),(b), the measured PL decay of the sample at a sample temperature of 4 K is presented for an excitation power of (a) 40 µW and (b) 5 µW respectively.

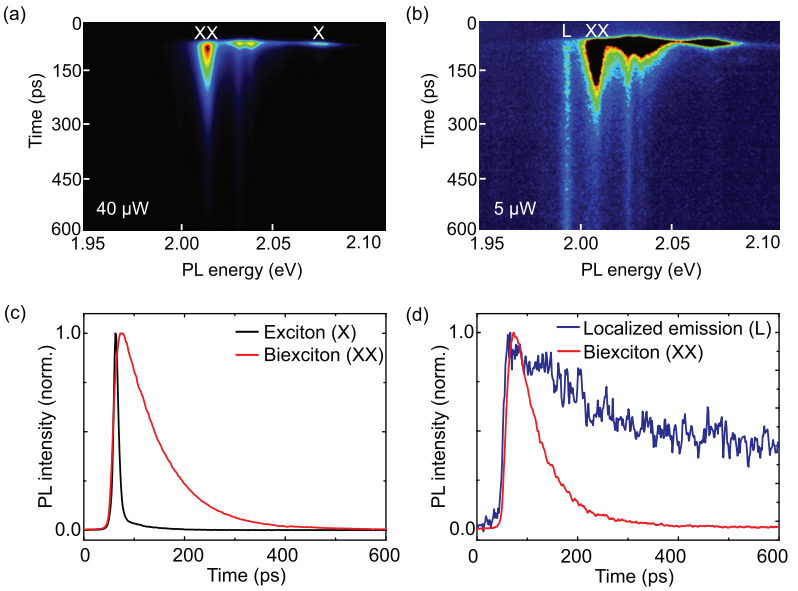


**Figure 5.7** | (a) False-color streak camera image of the PL decay measured on the hBN-encapsulated $WS_2$ monolayer at a temperature of 4 K and an average excitation power of 40 µW. (b) Same as (a) but with an excitation power of 5 µW. (c) Normalized time-resolved PL traces of the XX and X features extracted from (a). (d) Normalized time-resolved PL traces of the XX and the L features extracted from (b).

The extracted PL traces from the measurement under 40 µW excitation power are shown in Fig. 5.7(c). Qualitatively we can already infer that the decay of the biexciton occurs on far longer time scales than the neutral exciton. Fitting the decay of the biexciton with a single exponential decay yields a decay time of 83 ps, whereas the decay of the neutral exciton cannot be reasonably resolved within our system resolution of 10 ps. While we cannot provide a comprehensive explanation for the different decay dynamics of excitons and biexcitons at this point, a possible contribution to the longer

decay of the biexciton could be understood by the model proposed by Citrin [Cit94] for the scenario of biexcitons in GaAs/$Al_xGa_{1-x}As$ quantum wells. Here, within an excitonic molecule model, the radiative decay of the biexciton $\tau_{\mathrm{rad}}^{\mathrm{XX}}$ is related to the radiative decay of the exciton $\tau_{\mathrm{rad}}^{\mathrm{XX}}$ as $\tau_{\mathrm{rad}}^{\mathrm{XX}} = \mu\tau_{\mathrm{rad}}^{\mathrm{X}}$, where $\mu$ is a factor, which depends on the interexcitonic separation $d$ within the biexciton and the wave vector of light $q$ inside a monolayer by $\mu \sim (qd)^{-2}$. Based on the theoretical estimation by You *et al.* [You15], we assume $d \approx 4-5\,\mathrm{nm}$, which results in $\mu \sim 10^2$. Given typical radiative decay times of neutral excitons in the range of 1 ps, this estimation yields $\tau_{\mathrm{rad}}^{\mathrm{XX}} \sim 100\,\mathrm{ps}$ for the biexciton decay in reasonable agreement with our experimental observation.

In Fig. 5.7(d) we compare the extracted PL traces of the biexciton and the localized emission for an excitation power of 5 µW, where both features can be readily identified. Using a single exponential decay function, we obtain a decay time of the biexciton of 58 ps at this excitation power and a decay time of 256 ps for the L peak. We note that a single exponential fit does not fully capture the long-lived dynamics of the L peak. Very long decay times of the L peak at 4 K in monolayer TMDCs have been regularly observed in other studies [Wan14, You15, Ple16a]. Hence, this observation further indicates the different nature of the two low-energetic features (L and XX) and provides additional evidence for our attribution of the biexciton feature.

Taken together, the power dependence and the temperature series in steady-state PL combined with the time-resolved measurement allow us to attribute the superlinear peak as a function of excitation density to emission from biexcitons. Moreover, in line with recent observations, the encapsulation of the monolayer $WS_2$ drastically reduces the spectral broadening of all excitonic features. The resulting spectrally ultra-narrow biexciton peak of about 4.4 meV thus represents a highly suitable testbed for further spectroscopic studies of this many-body state as presented later in the chapter.

### 5.2.4 Biexcitons in momentum space

Following the initial optical characterization of the sample and the subsequent identification of biexciton emission, we now consider the structure of biexcitons in momentum space, which is crucial for a more thorough understanding of this many-body state. In monolayer TMDCs, optically bright excitons consist of electrons and holes, which are both situated either in the $K^+$ or $K^-$ valley. However, in the case of biexcitons, the situation in momentum space is more intricate. A many-body state consisting of two excitons gives rise to a variety of different possible configurations, which are illustrated schematically in Fig. 5.8. Here, the highest valence band and the two lowest

spin-split conduction bands of monolayer $WS_2$ together with a total of four possible different biexciton states are shown. The ground state ($XX_1$) consists of two excitons, where the respective electrons are situated in the lowest conduction band. While this arrangement is energetically the most favorable, it is optically dark as the intravalley electron-hole transitions are spin-forbidden in this case. Hence, we can rule out the $XX_1$ state to be responsible for the observed biexciton emission in our experiment. It is worth pointing out that the scenario of an optically dark biexciton ground state results from the negative sign of the conduction band splitting of tungsten-based TMDCs. In contrast, in molybdenum-based TMDCs, in which the conduction band splitting is positive, the $XX_1$ state is expected to be optically bright.

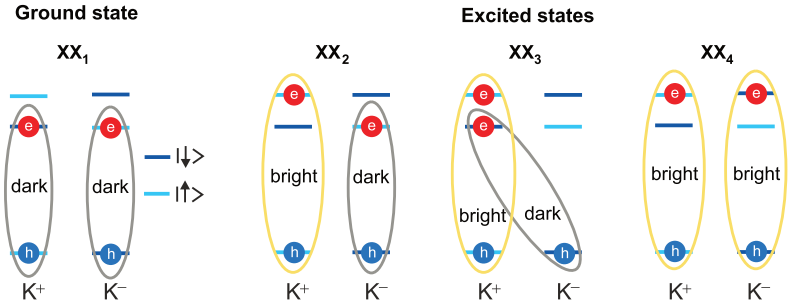


**Figure 5.8 |** Four different configurations of biexcitons in monolayer $WS_2$. The ground state ($XX_1$) is optically dark due to spin-forbidden transitions. Both excited states $XX_2$ and $XX_3$ consist of one bright exciton and one dark exciton, which is either spin-forbidden ($XX_2$) or indirect in momentum space ($XX_3$). The excited state $XX_4$ consists of two bright excitons.

Following these considerations it is reasonable to assume that the biexciton in our experiment stems from one of the excited states $XX_2$, $XX_2$ or $XX_4$ in Fig. 5.8. The $XX_2$ and $XX_3$ complexes are both of hybrid nature as they consist of one bright electron-hole pair, which can recombine by the emission of a photon, and one dark electron-hole pair that is optically inactive. We also take into account the highly excited state $XX_4$, which consists of two bright excitons, even though it is very probable that this state is energetically higher than $XX_2$ and $XX_3$ and thus less stable.

On the basis of the performed experiments so far, we are not able to identify the relevant biexciton configuration in our sample. However, as we will demonstrate in the following section, probing the biexciton feature in magneto-PL will allow us draw conclusions on the valley configuration of the biexciton in $WS_2$, inferring that it consists of a bright exciton in one valley and an intravalley dark exciton in the other valley ($XX_2$ state).

## 5.3 Biexcitons in high magnetic fields

In this section, we will examine the complex behavior of biexcitons in an hBN-encapsulated $WS_2$ monolayer under the influence of an external magnetic field up to 30 T. All experimental data from this section was acquired at the HFML in Nijmegen. The theoretical framework was elaborated and provided within a collaborative effort by Mikhail Durnev and Mikhail Glazov from the Ioffe Institute in St. Petersburg.

### 5.3.1 Zeeman splitting and inverted polarization

We start by analyzing the spectral evolution of the biexciton and the neutral exciton peak in an out-of-plane magnetic field up to 30 T. The sample is excited using linearly polarized light (photon energy 2.21 eV), populating both valley configurations equally, and the emitted PL is analyzed in a circularly polarized basis. In analogy to the magneto-PL study on interlayer excitons in chapter 4, this approach allows us to resolve the magnetic splitting and to quantify the field-induced degree of polarization.

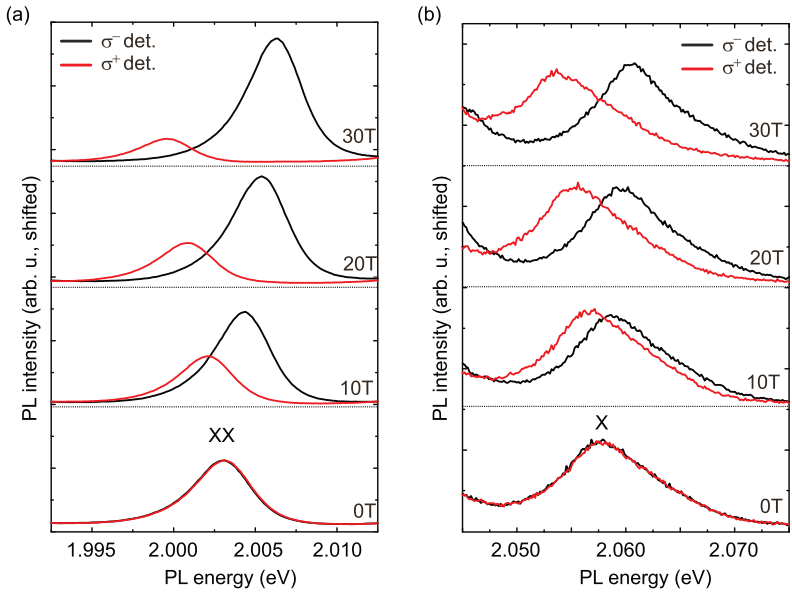


**Figure 5.9 |** Magneto-PL spectra of the (a) XX peak and (b) X peak for $\sigma^-$ and $\sigma^+$ polarized detection after linearly polarized excitation for various out-of-plane magnetic fields up to 30 T.

Fig. 5.9 (a) and (b) show the $\sigma^+$ and $\sigma^-$ polarized components of the biexciton and the exciton emission for magnetic fields from 0 T to 30 T in 10 T steps at a sample temperature of 4 K and an excitation power of 1000 µW. At a magnetic field of 0 T, neither XX nor X peak possess any energetic splitting or any field-induced polarization, as expected due the valley degeneracy. For $B > 0$ T, however, the polarized components exhibit an energetic separation, which amounts to about 6.7 meV for the highest fields of 30 T. Intriguingly, the intensities of the respective polarized components of the X and XX feature behave strikingly different. While the exciton is mostly unpolarized even at high fields, the biexciton emission shows a clear polarization, where the intensity of the energetically higher component in emission ($\sigma^-$ for $B > 0$) is strongly increased with respect to the lower-energy component.
To quantify our observations, we first calculate the energetic splitting of the $\sigma^\pm$ polarized emission peaks of exciton and biexciton from the experimental data, which is illustrated in Fig. 5.10(a).

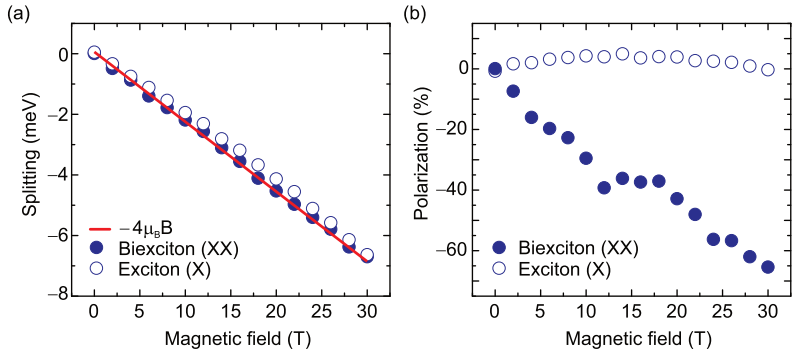


**Figure 5.10 |** (a) Energetic splitting of the X peak (open circles) and the XX peak (filled circles) as a function of magnetic field. The solid red line indicates a linear dependence with a $g$ factor of −4. (b) Field-induced polarization of the exciton and the biexciton.

In analogy to the experiments in chapter 4, we can relate the energetic splitting to the $g$ factor by $\Delta E = E^{\sigma^+} - E^{\sigma^-} = g_S \mu_B B$, where $\mu_B \approx 58\,\mu\text{eV/T}$ is the Bohr magneton, $B$ is the magnetic field, and $g_S$ is the spectroscopic $g$ factor. The spectroscopic $g$ factor $g_S$ refers to the state that we observe in emission. The reason for introducing this distinction, in contrast to chapter 4, will be explained shortly below. Using this definition we obtain a spectroscopic $g$ factor of the neutral exciton of $g_S^X = -3.8 \pm 0.1$, which is in very good agreement to previous magneto-PL measurements of the exciton in monolayer $WS_2$ [Sti16a, Ple16b, Kuh17]. The spectroscopic $g$ factor of the biexciton

is very similar and amounts to $g_S^{XX} = -3.8 \pm 0.1$. This is very reasonable since the radiative recombination of the biexciton is identical to the optically bright exciton.
The corresponding field-induced polarization, $P = (I_{\sigma^+} - I_{\sigma^-})/(I_{\sigma^+} + I_{\sigma^-})$ is shown in Fig. 5.10(b). For the neutral exciton, it remains mostly constant around 0 %, implying that no discernible population imbalance for this feature can be achieved even in high magnetic fields. However, the emission of the biexciton is strongly polarized and reaches values close to −70 % at 30 T. In stark contrast to our observation in chapter 4 for interlayer excitons, the component that emits at higher energy ($\sigma^-$) is favored in emission, resulting in a so-called inverted polarization of the XX peak.

### 5.3.2 The concept of the spectroscopic and total $g$ factor

We can tentatively understand the absence of field-induced polarization of the exciton resonance as a result of the ultra-short, $< 10$ ps, lifetime that was determined in section 5.2.3 for this feature. Combined with the off-resonant excitation conditions in the experiment, the excitons are likely to be far from a quasi-equilibrium within this short period of time and thus not able to relax to the energetically favorable state. However, the emergence of an inverted polarization of biexcitons, where the state emitting at higher energy is more populated, is, at first glance, puzzling. In fact, due to their longer lifetime of about 80 ps (see section 5.2.3) one could expect a thermalization of biexcitons over the Zeeman-split states and anticipate that the lower-energy component in emission will be stronger in intensity. This notion however neglects the fundamental concept that the population distribution of excitonic complexes between energetically separated states in a magnetic field is determined by the change of the total energy of the state and not only of the species that is responsible for the observed emission feature. Recently, this approach was successfully applied to explain the behavior of charged excitons in CdTe quantum wells in magneto-PL studies [Ast05, Bar11].
Hence, to incorporate this concept to our observations on biexcitons, we will resort to two different $g$ factors, namely the spectroscopic $g$ factor $g_S$ and the total $g$ factor $g_T$. The spectroscopic $g$ factor $g_S$ that was already used above is only related to the energy of the emitting state. In contrast to that, the total $g$ factor $g_T$ takes into account the Zeeman shifts of all constituents of the biexciton and therefore describes the total energy of the composite exciton state. Consequently, the relative population of an excitonic state between energetically split levels is given by the total $g$ factor. By assuming quasi-equilibrium, we can express the ratio of the two intensities $I_{\sigma^+}/I_{\sigma^-}$ in a straightforward model by means of a Boltzmann distribution as

$$\frac{I_{\sigma^+}}{I_{\sigma^-}} = exp\left(-\frac{g_T \mu_B B}{k_B T}\right), \tag{5.1}$$

where $T$ is the effective temperature of the biexciton gas and $k_B$ is the Boltzmann constant. Crucially, from this we expect an inverted polarization behavior, where $I_{\sigma^-} < I_{\sigma^+}$ holds, if the total $g$ factor is positive, i.e. $g_T > 0$.
At this point it is important to realize that the total $g$ factor can only deviate from the spectroscopic $g$ factor if the excitonic complex consists of more than two constituents. For the case of an exciton we always have $g_S = g_T$ since the emitting state is the same as the total excitonic complex. This is also the reason why the concept of two different $g$ factors was not relevant in the discussion of the magneto-PL data in chapter 4, as the interlayer exciton also consists only of two constituents. However, for many-body states such as the biexciton, the total $g$ factor can differ from the spectroscopic $g$ factor since it takes also into account the energies of the non-emitting complexes. Indeed, we will demonstrate in the following that this situation emerges for biexcitons in monolayer $WS_2$. Due to the presence of a dark exciton within this many-body state, the total energy can differ from the emission energy. As a consequence, this will allow us to explain the anomalous inverted polarization in a magnetic field and to reveal the momentum space configuration of the biexciton in our sample.

### 5.3.3 Theoretical framework of the $g$ factor components

Before we theoretically analyze the total $g$ factor of the different biexciton complexes from section 5.2.4, we introduce the relevant framework to describe the $g$ factors of the individual conduction and valence bands in this chapter. In a first step, this will also allow us to deduce a theoretical estimation of the spectroscopic $g$ factor and to compare this value to our experimental observation in section 5.3.1. In chapter 4, the $g$ factor was determined in an atomistic viewpoint by the individual contributions arising from the spin magnetic moment, the atomic orbitals and the valley magnetic moment. In this chapter however, based on the collaboration with Mikhail Durnev and Mikhail Glazov, we use an alternative approach, where the $g$ factors are calculated by $k \cdot p$ perturbation theory, which allows one to relate the $g$ factor with the band structure parameters of the respective monolayer TMDC. Specifically, we resort to calculated values provided by Rybkovskiy *et al.* [Ryb17], where the parametrization of the multiband $k \cdot p$ Hamiltonian was determined by decomposing tight-binding models in the vicinity of the $K^+$ and $K^-$ points. The Zeeman Hamiltonian for an electron in the conduction band c or valence band v reads then [Ryb17]:

$$H_{\mathrm{c,v}} = \frac{1}{2}\mu_B B(g^{\mathrm{orb}}_{\mathrm{c,v}}\tau_z + g^{\mathrm{sp}}_{\mathrm{c,v}}\sigma_z). \tag{5.2}$$

Here, $g^{\mathrm{sp}}$ is the spin contribution ($\sigma_z = \pm 1$ is the spin index) and $g^{\mathrm{orb}}$ describes the orbital contributions ($\tau_z = \pm 1$ is the valley index) to the energetic splitting. Note here that the so-called orbital contribution within this approach combines the two magnetic moments (orbital and valley) of the atomistic approach presented in chapter 4. The spin contribution $g^{\mathrm{sp}}$ is set to the vacuum value of 2 for both conduction and valence bands since it is mostly not affected by the crystal environment. For the orbital contributions $g^{\mathrm{orb}}$ of conduction and valence band, Rybkovskiy *et al.* [Ryb17] provide values of $g^{\mathrm{orb}}_{\mathrm{v}} = 3.96$ and $g^{\mathrm{orb}}_{\mathrm{c}} = 0.11$ for the case of monolayer $WS_2$. Based on these values, we can now calculate the spectroscopic $g$ factor of the optically bright exciton and biexciton using the following relation:

$$g^{\mathrm{XX}}_{\mathrm{S}} = g^{\mathrm{X}}_{\mathrm{S}} = g^{\mathrm{orb}}_{\mathrm{c}} + g^{\mathrm{sp}}_{\mathrm{c}} - g^{\mathrm{orb}}_{\mathrm{v}} - g^{\mathrm{sp}}_{\mathrm{v}}\,. \tag{5.3}$$

By inserting the values provided above we obtain a theoretical value of $g_{\mathrm{S}}$ for both exciton and biexciton of $g^{\mathrm{X}}_{\mathrm{S,th}} = g^{\mathrm{XX}}_{\mathrm{S,th}} = -3.85$, which is excellent agreement to our experimental observation of $g^{\mathrm{X}}_{\mathrm{S}} = -3.8 \pm 0.1$ and $g^{\mathrm{XX}}_{\mathrm{S}} = -3.9 \pm 0.1$.

### 5.3.4 The hybrid composition of biexcitons in momentum space

We now turn to the analysis of the total $g$ factor of the different possible biexciton configurations that were outlined in section 5.2.4. The $XX_1$ state will be neglected in the following since it is optically dark. Based on the two contributions $g^{\mathrm{sp}}$ and $g^{\mathrm{orb}}$, the energy level evolution of the $\sigma^+$ polarized transition of the biexciton configurations $XX_2$, $XX_3$ and $XX_4$ is illustrated in Fig. 5.11(a). The behavior of the $\sigma^-$ transition follows from time-reversal symmetry (not shown here). As can be seen, the relevant two lowest conduction bands and the highest valence band undergo an energetic shift in a positive applied magnetic field due to the spin and orbital contributions. Note that the length of the arrows in Fig. 5.11 is not directly proportional to the magnitude of the individual contributions. To calculate the total $g$ factor of a biexciton configuration, we have to take into account all contributions from the participating excitonic complexes. In Fig. 5.11(b) the individual spin and orbital contributions for all excitonic complexes of the respective biexciton configuration are summarized. By adding up the $g$ factors of the individual constituents, one can estimate the total $g$ factor of the respective

biexciton configuration, as will be shown in the following.

First, we discuss the scenario of the $XX_2$ complex. The $g$ factor of the bright exciton $g^{X}_{bright}$ of $XX_2$ is equivalent to the already determined spectroscopic $g$ factor $g^{X}_{S}$ and thus amounts to $-3.85$. The dark state in $XX_2$ is of intra-valley nature, leading to an antiparallel evolution of the contributions from spin in the conduction and valence bands in a positive magnetic field. Therefore, we can write $g^{X}_{dark}$ of $XX_2$ as $g^{X}_{dark}(XX_2) = -g^{orb}_{c} + g^{sp}_{c} + g^{orb}_{v} + g^{sp}_{v} = 7.85$. Adding the bright and dark component of $XX_2$ up thus results in a total $g$ factor of $g^{XX_2}_{T} = -3.85 + 7.85 = 4$.

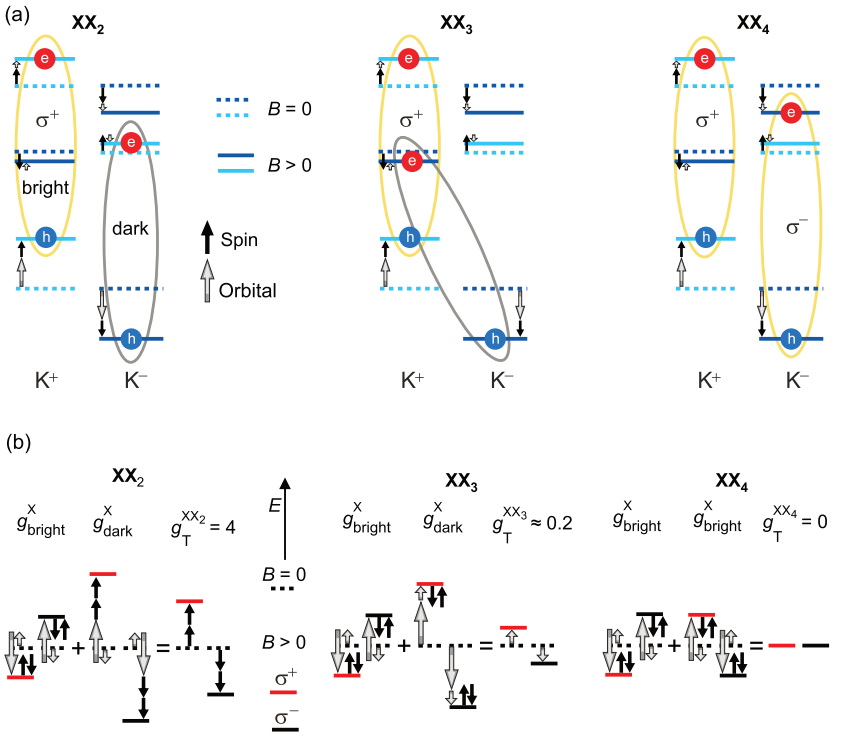


**Figure 5.11 |** (a) Expected evolution of the energy levels of the bright $\sigma^+$ state of $XX_2$, $XX_3$ and $XX_4$ with positive applied magnetic field ($B > 0$). The dashed lines indicate the situation for $B = 0$. Black arrows represent the spin contribution and black-grey arrows the orbital contribution to the total energy splitting. (b) Schematic energetic representation of $XX_2$, $XX_3$ and $XX_4$ with the individual $g$ factors of the bright exciton, the dark state and the resulting total $g$ factor of the respective biexciton state. Dashed lines show the situation for $B = 0$.

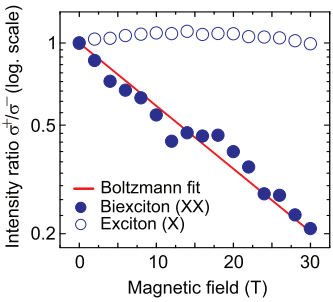


**Figure 5.12 |** Intensity ratio $I_{\sigma^+}/I_{\sigma^-}$ derived from the data in Fig. 5.10(b) for the biexciton and exciton peak. The solid red line corresponds to a fit to a thermal Boltzmann distribution using equation (5.1), with $g_{\mathrm{T}}^{\mathrm{XX}} = 4$. The corresponding temperature of the biexciton gas in this fit is $T = 50\,\mathrm{K}$.

Second, we calculate the expected total $g$ factor of the $XX_3$ configuration. In analogy to the situation in $XX_2$, the $g$ factor of the bright exciton amounts to $-3.85$. However, in contrast to $XX_2$, the dark state now extends over valleys of different index, which gives rise to an additional contribution from the orbital component in the conduction band, while the spin component in the conduction and valence band evolves parallel. Hence, the $g$ factor of the dark state of $XX_3$ can be written as $g_{\mathrm{dark}}^{\mathrm{X}}(\mathrm{XX}_3) = g_{\mathrm{c}}^{\mathrm{orb}} - g_{\mathrm{c}}^{\mathrm{sp}} + g_{\mathrm{v}}^{\mathrm{orb}} + g_{\mathrm{v}}^{\mathrm{sp}} = 4.07$, yielding a total $g$ factor of $g_{\mathrm{T}}^{\mathrm{XX_3}} = -3.85 + 4.07 = 0.22$. Finally, we shortly treat the case of the $XX_4$ complex. As this state consists of two bright excitons, all individual contributions to the total $g$ factor cancel out entirely, which results in a total $g$ factor of $XX_4$ of $g_{\mathrm{T}}^{\mathrm{XX_4}} = 0$.

To briefly summarize here, we could determine the expected total $g$ factors of the three relevant biexciton configurations by considering the energetic evolution of all constituents in a magnetic field. The respective values for the three complexes are $g_{\mathrm{T}}^{\mathrm{XX_2}} = 4$, $g_{\mathrm{T}}^{\mathrm{XX_3}} = 0.22$ and $g_{\mathrm{T}}^{\mathrm{XX_4}} = 0$.

Based on our previous considerations, we can explain the observed inverted polarization of the biexciton feature if the total $g$ factor is positive. Hence, we can exclude $XX_4$ as a possible configuration since its total $g$ factor of 0 would result in no population imbalance. Additionally, the observation of this state is rather unlikely due to its high-energy nature. This leaves $XX_2$ and $XX_3$ as the two remaining possible momentum space arrangements of the biexciton on our sample since both states lead to an inverted polarization due to their positive total $g$ factor. To resolve this situation, we return to the thermal Boltzmann distribution from equation 5.1 to describe the intensity relation of the two polarized components $I_{\sigma^+}/I_{\sigma^-}$ as shown in Fig. 5.12. In a straightforward picture, assuming quasi-equilibrium, the population of biexcitons between the two Zeeman-split states is determined by this relation. By fitting the data with the previously obtained theoretical estimations of $g_{\mathrm{T}}$ for $XX_2$ and $XX_3$, we can

extract the effective temperature of the biexciton gas $T$ for a given total $g$ factor. This yields an effective temperature of $T \approx 50\,\mathrm{K}$ for the $XX_2$ configuration and $T \approx 2.5\,\mathrm{K}$ for the $XX_3$ configuration. The fact that the nominal sample temperature in our setup is 4 K renders the $XX_3$ scenario highly unlikely due to its effective temperature of $T \approx 2.5\,\mathrm{K}$. From this we can conclude that the observed inverted polarization stems from the $XX_2$ biexciton, consisting of a bright exciton in one valley and an intravalley dark exciton in the other valley.

The recombination pathway of the $XX_2$ state and the resulting inverted polarization is further illustrated in Fig. 5.13. Since the total Zeeman splitting ($g_T^{XX_2}$) depends on both the contribution from the bright and dark exciton, the $XX_2$ state splits with a reversed energetic order compared to its bright exciton component. Consequently, as can be seen, even though the $\sigma^-$ polarized component emits at a higher energy than the $\sigma^+$ polarized state, the $\sigma^-$ state is more populated due to the positive total $g$ factor of the $XX_2$ configuration.

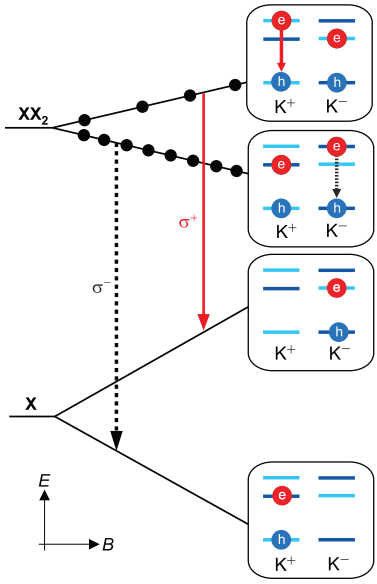


**Figure 5.13 |** Schematic illustration of the recombination of the $XX_2$ biexciton, where the lower-energy state of $XX_2$ emits at a higher photon energy. The number of filled circles indicates the relative populations of the Zeeman-split $XX_2$ states.

Finally, we aim to understand the apparent deviation of the derived effective temperature $T$ of the biexciton gas ($T \approx 50\,\mathrm{K}$) from the nominal sample temperature $T = 4\,\mathrm{K}$ in the experiment. In principle, this can either result from a lack of full thermal equilibrium of the biexciton gas with the lattice due to slow cooling by acoustic phonons or from the heating of the crystal lattice itself as a result of the high excitation power (1000 µW) used in the experiment. We can roughly estimate the latter effect by tracking the power-induced redshift from the power series in Fig. 5.5 and compare it to the typical temperature dependence of the peak energies in the temperature series in Fig. 5.6. As indicated by the dashed grey line in Fig. 5.5(a), the redshift of the trion amounts to 2.1 meV at 1000 µW. This shift can now be brought into relation to the temperature-dependent data, which is further shown in the range from 4 K to 60 K in Fig. 5.14. To quantify the estimated lattice temperature at an energy shift of 2.1 meV, we apply three of the most prominent analytical functions from the literature by Varshni [Var67], Viña *et al.* [Viñ84] and Pässler [Päs97] to the data. While all three functions generally provide reasonable fits to temperature-dependent PL data, it should be noted here that they mostly serve as a phenomenological description and the resulting fit parameters usually cannot be related to sensible physical quantities.

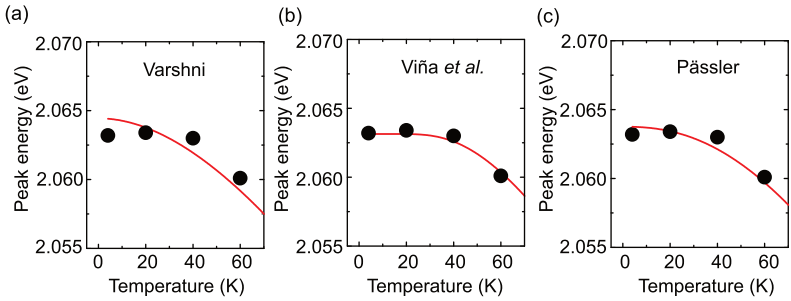


**Figure 5.14 |** (a)-(c) Peak energy of the neutral exciton as a function of temperature from 4 K to 60 K including the respective fit function (red line) by (a) Varshni, (b) Vina *et al.* and (c) Pässler.

In Fig. 5.14(a) the fit using the model by Varshni is shown, which was already introduced in chapter 4 (equation 4.3). The second fit function as proposed by Viña *et al.* [Viñ84] follows

$$E_g(T) = E_L - a_L \left(1 + \frac{2}{exp\left(\frac{\Theta}{T}\right) - 1}\right) \tag{5.4}$$

and is shown in Fig. 5.14(b). Here, the $T \approx 0$ limit is provided by the parameters $E_\mathrm{g}(0) = E_\mathrm{L} - a_\mathrm{L}$ and the material-specific characteristic phonon temperature is represented by $\Theta$.
Finally, the model given by Pässler [Päs97] provides the following formula:

$$E_\mathrm{g}(T) = E_\mathrm{g}(0) - \frac{\gamma\Theta}{2}\left[\sqrt[\mathrm{p}]{1+\left(\frac{2T}{\Theta}\right)^\mathrm{p}} - 1\right] , \tag{5.5}$$

where $E_\mathrm{g}(0)$ represents the energy of the bandgap at 0 K, $\Theta$ the material-specific characteristic phonon temperature and $\gamma$ and p are fit parameters. The resulting function together with the data is depicted in Fig. 5.14(c).
Based on these analytical descriptions of the temperature dependence we can deduce an estimated sample temperature of 35 K (Varshni), 43 K (Pässler) and 55 K (Viña *et al.*) for the given redshift of 2.1 meV at an excitation power of 1000 µW. All these values are in reasonable agreement with the estimated effective temperature of the $XX_2$ biexciton state of about 50 K, which further strengthens our assignment of prevalent momentum space configuration of biexcitons in monolayer $WS_2$.
Taken together, the presented spectroscopic measurements of biexcitons in hBN-encapsulated $WS_2$ underline the intriguing physics of this many-body state in a monolayer TMDC. Combining power- and temperature-dependent steady-state PL measurements with time-resolved data allows us to unambiguously identify biexcitonic emission in our sample. The encapsulation of the monolayer with hBN results in significantly reduced linewidths of all excitonic features and leads to a biexciton feature with a linewidth as narrow as 4.4 meV. In magneto-PL, we determine the spectroscopic $g$ factor of the biexciton to be $g_\mathrm{S}^\mathrm{XX} = -3.9 \pm 0.1$, in close agreement to the spectroscopic $g$ factor of the neutral exciton $g_\mathrm{S}^\mathrm{X} = -3.8 \pm 0.1$. Most importantly, we observe an inverted polarization of the biexciton in an out-of-plane magnetic field, implying that the state emitting at a higher energy is preferentially populated. We explain this behavior by taking into account the evolution of the total energy of all excitonic constituents, which is responsible for the distribution of states in a magnetic field. The subsequent analysis enables us to elucidate the specific momentum space configuration of the biexciton in monolayer $WS_2$ ($XX_2$) as a hybrid state consisting of one bright exciton in one valley and an intravalley dark exciton in the other valley.

## 5.4 Alternative scenario: The charged biexciton

The analysis from the previous section was based on the assumption that the observed biexciton is charge-neutral, i.e. it consists of two excitons implying a biexciton binding energy of about 50 meV. This assignment is in line with previous observations of biexciton emission in tungsten-based monolayer TMDCs [You15, Ple15, Sha15]. However, recent experiments on monolayer $MoSe_2$ found a binding energy of the neutral biexciton of about 20 meV [Hao17a]. Moreover, as already stated in section 5.2.2, several theoretical works suggest a biexciton binding energy in the same energetic region and a binding energy of the charged biexciton of about 50 meV [Zha15b, Kyl15, Szy17]. This attribution was corroborated very recently by four experimental studies which examine the gate-dependent biexcitonic properties of hBN-encapsulated monolayer $WSe_2$ [Bar18, Che18, Li18, Ye18]. By changing the density of the free carriers in the sample via an external gate, it could be shown that the binding energy of the neutral and charged biexciton amounts to about 20 meV and 50 meV, respectively.

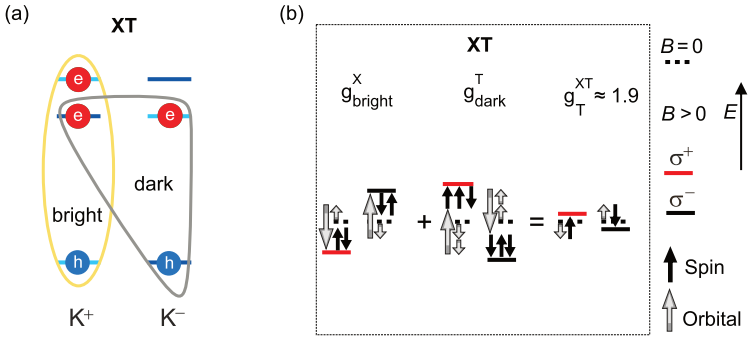


**Figure 5.15 |** (a) Momentum space configuration of the lowest-energy charged biexciton complex (XT) in monolayer $WS_2$. (b) Expected evolution of the energy levels of the charged biexciton with the respective $g$ factors of the bright exciton and the dark trion. The resulting total $g$ factor of the configuration amounts to $g_T^{XT} \approx 1.9$.

Taking these indications together, an alternative interpretation of the studied biexcitonic feature in this chapter as a charged biexciton emerges as a plausible scenario. In the following, we want to briefly discuss the configuration of a charged biexciton in momentum space, the resulting spectroscopic and total $g$ factor of this many-body state and the interpretation of our observation in light of this alternative scenario.
The expected lowest-energy composition of the charged biexciton (XT) in momentum space is illustrated in Fig. 5.15(a). As can be seen, it consists of one bright exciton

and one optically dark trion, which is forming a spin singlet. To evaluate the expected behavior of the XT complex in a magnetic field, we resort again to the two different $g$ factors, $g_S$ and $g_T$ of the system, which is further depicted in Fig. 5.15(b). In analogy to the discussed charge-neutral configurations from the previous section, the spectroscopic $g$ factor of the bright emission of the XT complex amounts to $g_S^{XT} = -3.85$ as it only depends on the recombination of the bright electron-hole pair (see $g_{bright}^{X}$ in Fig. 5.15(b)). However, to calculate the total $g$ factor of the charged biexciton in a magnetic field, we have to take into account an additional electron and its contribution from spin and orbital magnetic moments to the $g$ factor of the dark trion state. Thus, the $g$ factor of the dark state of XT can be expressed as $g_{dark}^{T}(XT) = g_v^{orb} - 2g_c^{orb} + 2g_c^{sp} - g_v^{sp} = 3.96 - 2 \cdot 0.11 + 2 \cdot 2 - 2 = 5.74$. By adding the bright and dark component of the respective $g$ factor up, we obtain a value of the total $g$ factor of XT of $g_T^{XT} = -3.85 + 5.74 \approx 1.9$. Hence, the total energy of the charged biexciton in a magnetic field is described by a positive $g$ factor, which is a crucial prerequisite for the observation of an inverted polarization.

Based on this total $g$ factor of about 1.9 for the charged biexciton, we can estimate the effective temperature of the gas of charged biexcitons by using the Boltzmann distribution (equation 5.1), resulting in a temperature of about 25 K. Due to the smaller total $g$ factor of XT, this value is naturally lower than the estimated temperature of about 50 K of the neutral $XX_2$ complex ($g_T^{XX_2} = +4$). Nevertheless, it is still in qualitative agreement to the estimated sample temperature of about 35 – 50 K that we extracted in the previous section from the comparison of power-dependent PL and the respective energetic shift in temperature-dependent PL measurements.

We can therefore summarize that the assignment of the superlinear feature in our experiment to emission from a charged biexciton is a reasonable alternative scenario for the interpretation of our data. Similar to the case of the charge-neutral $XX_2$ state, the charged biexciton possesses a positive total $g$ factor due to the contributions from the dark state, which is the fundamental prerequisite to understand the observed inverted polarization of the biexciton feature. The recently published work on the closely related material $WSe_2$ represents indeed strong evidence for the interpretation of our observed feature as a charged biexciton. However, to unambiguously resolve this conflict, future measurements on gated hBN-encapsulated $WS_2$ monolayer are required, which are beyond the scope of the present thesis.

Chapter 6

# Summary and outlook

In this thesis, the remarkable properties of excitons in atomically thin van der Waals heterostructures were intensively studied within two different material platforms. By using photoluminescence spectroscopy as the main experimental technique, novel insights on the behavior of these Coulomb-bound quasiparticles could be obtained for the case of an atomically thin heterostructure and an hBN-encapsulated monolayer.

In the first main project, the deterministic fabrication by means of the PDMS transfer technique allowed us to create a heterostructure consisting of two different monolayer TMDCs ($MoSe_2$ and $WSe_2$). Due to the type II band alignment, spatially indirect interlayer excitons are formed in this structure, where the electrons and holes are situated in different layers. For this material combination, direct optical transitions at the K points are only expected for twist angles of the heterostructure close to 0° (AA stacking) and 60° (AB stacking). Resorting to SHG spectroscopy, an AB stacking of the heterostructure could be determined, which gives rise to radiatively allowed interlayer exciton transitions between valleys of different index. In low-temperature PL measurements, we could observe the energetically well-separated emission from interlayer excitons in the sample. The attribution of this excitonic species was further supported by PLE measurements. Here, a clear enhancement of the interlayer exciton PL could be observed once the excitation energy of the laser was close to the main excitonic resonances of $MoSe_2$ and $WSe_2$. Furthermore, helicity-resolved PL measurements demonstrated the emergence of valley polarization of interlayer excitons, which could be tuned by varying the excitation energy of the laser.

Following this initial optical characterization, we then focused on the interaction effects and dynamics of interlayer excitons [Nag17b]. Temperature-dependent PL measurements on the heterostructure revealed an anomalous behavior of both the peak

position and the spectral linewidth of the interlayer exciton. These observations could be explained by taking into account disorder effects that arise from the inhomogeneous potential landscape in the heterostructure. Power-dependent PL measurements showed a pronounced blueshift of the interlayer exciton peak position that could not be observed for the monolayer excitons in the same experiment. It was proposed that the main mechanism behind this phenomenon is the repulsive dipole-dipole interaction of the spatially separated interlayer excitons, where electron and hole reside in different layers yielding permanent electrical dipoles. Time-resolved measurements gave access to the dynamics of interlayer excitons. Strikingly, the measured lifetime of interlayer excitons at 4 K was found to be in the nanosecond regime, clearly exceeding typical decay times of intralayer excitons by orders of magnitude as a result of the increased spatial separation of electrons and holes. The streak camera system allowed us to track the spectral evolution of the interlayer exciton PL at low temperatures for the first time. The observed initial broadening and subsequent blueshifted PL emission at later times was explained by a three-step process, where interlayer excitons decay within the inhomogeneous potential landscape of the heterostructure, accompanied by the effects of dipolar exciton repulsion. Furthermore, we studied the PL decay of interlayer excitons as a function of sample temperature and excitation power. It was shown that by combining our observations from the steady-state PL and the time-resolved PL measurements, an overall energetic tuning range of about 20 meV of the interlayer exciton can be achieved. Applying a basic capacitor model finally allowed us to provide a lower boundary of the interlayer exciton density in our experiments of about $n_{\mathrm{IEX}} \approx 4 \cdot 10^{10}\mathrm{cm}^{-2}$.

The intricate properties of interlayer excitons in a two-dimensional heterostructure were further investigated at the High Field Magnetic Laboratory in Nijmegen. Here, we could examine the behavior of this excitonic species under the influence of an external magnetic field up to 30 T for the first time [Nag17a]. Generally, the out-of-plane magnetic field lifts the valley degeneracy of all excitonic features. However, the energetic shifts of intra- and interlayer excitons deviated strongly from each other. For the excitonic resonance of monolayer $WSe_2$ we obtained a $g$ factor of $-3.7 \pm 0.1$, which is in line with recent literature. A three-component atomistic model consisting of contributions from spin, atomic orbital and valley magnetic moment provided a reasonable framework to understand the observed $g$ factor. In stark contrast to that, the $g$ factor of the interlayer exciton was determined to be $-15.1 \pm 0.1$ in our sample. Moreover, the valley polarization of the interlayer exciton reached values of more than 80 % for the highest fields of 30 T. In light of the evenly distributed exciton population right after the

linearly polarized excitation, this value is particularly remarkable. The anomalously high value of the $g$ factor of the interlayer exciton could be understood by resorting to the same framework as it was applied for the intralayer excitons. Most importantly, due to the AB stacking of the studied heterostructure and the resulting optically allowed intervalley transitions, the contributions from the valley magnetic moment add up. This gives rise to a drastic increase of the total magnetic response of the interlayer exciton in comparison to the monolayer case. Finally, it could be demonstrated that the lifetime of the interlayer exciton increases in an external magnetic field, presumably as a result of a smaller wave function overlap.

The second main project of this thesis dealt with the spectroscopic study of biexcitons emerging in a monolayer of $WS_2$, which was encapsulated by two thin sheets of hBN [Nag18]. This heterostructure was also fabricated by a step-by-step procedure using the PDMS transfer technique. In low-temperature PL experiments, it could be shown that the encapsulation of the monolayer with hBN results in a drastic reduction of the inhomogeneous broadening of all excitonic features, in agreement with similar observations in recent literature. The subsequent PL measurements revealed an ultra-narrow feature with superlinear power dependence, which was attributed to emission stemming from biexcitons. This assessment was further corroborated by a temperature-dependent PL series, where biexciton emission was discernible up to a nominal sample temperature of 100 K. Furthermore, by using the streak camera system, it was shown that the PL decay of the biexciton at low temperatures occurs on far longer timescales than that of the neutral exciton.

Crucially, by studying the effects of an external out-of-plane magnetic field on the behavior of biexcitons in monolayer TMDCs for the first time, we could reveal the momentum space configuration of this complex many-body state. As for the case of interlayer excitons, these experiments were also performed at the HFML in Nijmegen with magnetic fields up to 30 T. The observed $g$ factor of the neutral exciton and the biexciton were found to be largely the same in the experiment, as expected from the identical radiative pathway of both excitonic features. However, while the emission of the neutral exciton remained mostly unpolarized even at the highest fields, the biexciton exhibited a strongly inverted polarization of around $-70\,\%$, implying that the component emitting at higher energy is favored in emission. This intricate phenomenon could be understood by introducing a distinction for the $g$ factor into the spectroscopic $g$ factor, which is related to the energy of the emitting state and a total $g$ factor, which summarizes the contributions from all biexcitonic constituents. It could be shown that within the assumption of a Boltzmann distribution between the energetic levels,

an inverted polarization of the biexciton emerges for the case of a positive total $g$ factor. By comparing possible momentum space configurations of the biexciton and their respective expected total $g$ factor with the observed degree of polarization, it could be revealed that the biexciton is of hybrid nature as it consists of one bright exciton in one valley and an intravalley dark exciton in the other valley. Finally, it was outlined that an attribution of the studied feature as a charged biexciton is consistent with the proposed model system and represents a plausible alternative interpretation for our observations.

The aim of this thesis is to contribute to the understanding of exciton physics in van der Waals heterostructures. Nevertheless, as the field is evolving on a rapid pace, a plethora of outstanding questions remains, giving rise to multiple possible future research directions. The encapsulation of monolayer TMDCs with hBN and the demonstrated ultra-narrow excitonic features in such samples represent a clear advancement from a spectroscopic point of view. A natural next step would be to study the time-resolved dynamics of complex many-body states like the biexciton more thoroughly as a function of different experimental parameters such as sample temperature or excitation density. This could also provide new insights on the formation processes of these excitonic species. Moreover, the understanding of valley polarization effects of this many-body complex is still in its infancy, let alone the evolution of the valley dynamics. Generally, more research is required to understand why the formation of biexcitons seems to be strongly favored in tungsten-based TMDCs compared to molybdenum-based monolayers. From a fundamental point of view, the recent experimental confirmation of the existence of charged biexciton complexes in monolayer TMDCs is particularly promising since such a Coulomb-bound five-particle state could not be observed in any other material system up to now.

At the same time, interlayer excitons arising from atomically thin van der Waals heterostructures represent a highly promising playground for further spectroscopic studies. While the binding energy of excitons in monolayer TMDCs could already be determined by a variety of experimental techniques [Wan18], a direct measurement of this crucial quantity for interlayer excitons is still lacking. In particular, the weak oscillator strength of interlayer excitons renders the observation of excitonic resonances via interband absorption spectroscopy highly unlikely. A direct approach to overcome these problems comprises the measurement of the excitonic $1s$–$2p$ transition of interlayer excitons in a large-area van der Waals heterostructure using terahertz pump-probe spectroscopy. Very recently, this technique was successfully applied for the first time in a $WSe_2/WS_2$ heterostructure to determine a binding energy of interlayer excitons

of 118 meV [Mer18]. Alternatively, the measurement of the so-called diamagnetic shift of interlayer excitons in very high magnetic fields could be used to estimate their binding energy. This energetic shift evolves quadratically with the applied magnetic field and arises in the weak-field limit, where effects by an external magnetic field are considerably smaller than the exciton binding energy [Miu07]. Since the diamagnetic shift is sensitive to the mean square radius of the exciton state, it can be subsequently employed to approximate the binding energy. Recently, this method was successfully applied to estimate the binding energy of excitons in monolayer TMDCs [Sti16a, Ple16b, Mit16, Sti18, Zip18].

Fundamental additional insights on the physics of interlayer excitons can be expected by studying the implications of moiré effects on these Coulomb-bound quasiparticles [Riv18]. Long-period moiré patterns arise in van der Waals heterostructures with small lattice mismatch and nearly aligned crystallographic axes. It was shown by scanning tunneling microscopy measurements that such a superlattice can imprint a position-dependent potential landscape for interlayer excitons with a variation of about 150 meV [Zha17a]. One of the most important consequences of this modulation is the emergence of an inverted circular polarization of interlayer excitons for certain potential minima [Yu17, Hsu18]. Very recently, first direct experimental signatures of moiré excitons could be observed in hBN-encapsulated $WSe_2/MoSe_2$ heterostructures [Tra18, Sey18], representing an encouraging prospect for the further development of the field.

Ultimately, long sought-after phenomena such as the unambiguous observation of an excitonic Bose-Einstein condensate could be realized by resorting to van der Waals heterostructures. This would be facilitated by an elevated degeneracy temperature in comparison to GaAs-based systems due to the large binding energies of interlayer excitons in TMDC heterostructures in combination with their long lifetimes and the potential for high exciton densities [Fog14]. Clearly, the spectroscopic study of excitons in van der Waals heterostructures offers exciting perspectives for fundamental research over the upcoming years.

# Bibliography


[Aiv15] G. Aivazian, Z. Gong, A. M. Jones, R.-L. Chu, J. Yan, D. G. Mandrus, C. Zhang, D. Cobden, W. Yao, and X. Xu, *Magnetic control of valley pseudospin in monolayer $WSe_2$*, Nat. Phys. **11**, 148–152 (2015).

[Aja17] O. A. Ajayi, J. V. Ardelean, G. D. Shepard, J. Wang, A. Antony, T. Taniguchi, K. Watanabe, T. F. Heinz, S. Strauf, X.-Y. Zhu, and J. C. Hone, *Approaching the intrinsic photoluminescence linewidth in transition metal dichalcogenide monolayers*, 2D Mater. **4**, 031011 (2017).

[Alb02] K. Albe and A. Klein, *Density-functional-theory calculations of electronic band structure of single-crystal and single-layer $WS_2$*, Phys. Rev. B **66**, 073413 (2002).

[Ama15] M. Amani, D.-H. Lien, D. Kiriya, J. Xiao, A. Azcatl, J. Noh, S. R. Madhvapathy, R. Addou, S. KC, M. Dubey, K. Cho, R. M. Wallace, S.-C. Lee, J.-H. He, J. W. Ager, X. Zhang, E. Yablonovitch, and A. Javey, *Near-unity photoluminescence quantum yield in $MoS_2$*, Science **350**, 1065–1068 (2015).

[And91] L. C. Andreani, F. Tassone, and F. Bassani, *Radiative lifetime of free excitons in quantum wells*, Solid State Commun. **77**, 641–645 (1991).

[Aro15a] A. Arora, M. Koperski, K. Nogajewski, J. Marcus, C. Faugeras, and M. Potemski, *Excitonic resonances in thin films of $WSe_2$: from monolayer to bulk material*, Nanoscale **7**, 10421–10429 (2015).

[Aro15b] A. Arora, K. Nogajewski, M. Molas, M. Koperski, and M. Potemski, *Exciton band structure in layered $MoSe_2$: from a monolayer to the bulk limit*, Nanoscale **7**, 20769–20775 (2015).

[Ast05] G. V. Astakhov, D. R. Yakovlev, V. V. Rudenkov, P. C. M. Christianen, T. Barrick, S. A. Crooker, A. B. Dzyubenko, W. Ossau, J. C. Maan, G. Karczewski, and T. Wojtowicz, *Definitive observation of the dark triplet ground state of charged excitons in high magnetic fields*, Phys. Rev. B **71**, 201312(R) (2005).

[Bar98] S. D. Baranovskii, R. Eichmann, and P. Thomas, *Temperature-dependent exciton luminescence in quantum wells by computer simulation*, Phys. Rev. B **58**, 13081–13087 (1998).

[Bar11] G. Bartsch, M. Gerbracht, D. R. Yakovlev, J. H. Blokland, P. C. M. Christianen, E. A. Zhukov, A. B. Dzyubenko, G. Karczewski, T. Wojtowicz, J. Kossut, J. C. Maan, and M. Bayer, *Positively versus negatively charged excitons: A high magnetic field study of $CdTe/Cd_{1-x}Mg_xTe$ quantum wells*, Phys. Rev. B **83**, 235317 (2011).

[Bar14] C. J. Bardeen, *The Structure and Dynamics of Molecular Excitons*, Annu. Rev. Phys. Chem. **65**, 127–148 (2014).

[Bar17a] M. Baranowski, A. Surrente, L. Klopotowski, J. M. Urban, N. Zhang, D. K. Maude, K. Wiwatowski, S. Mackowski, Y. C. Kung, D. Dumcenco, A. Kis, and P. Plochocka, *Probing the Interlayer Exciton Physics in a $MoS_2/MoSe_2/MoS_2$ van der Waals Heterostructure*, Nano Lett. **17**, 6360–6365 (2017).

[Bar17b] M. Baranowski, A. Surrente, D. K. Maude, M. V. Ballottin, A. A. Mitioglu, P. C. M. Christianen, Y. C. Kung, D. Dumcenco, A. Kis, and P. Plochocka, *Dark excitons and the elusive valley polarization in transition metal dichalcogenides*, 2D Mater. **4**, 025016 (2017).

[Bar18] M. Barbone, A. R.-P. Montblanch, D. M. Kara, C. Palacios-Berraquero, A. R. Cadore, D. De Fazio, B. Pingault, E. Mostaani, H. Li, B. Chen, K. Watanabe, T. Taniguchi, S. Tongay, G. Wang, A. C. Ferrari, and M. Atatüre, *Charge-tuneable biexciton complexes in monolayer $WSe_2$*, Nat. Commun. **9**, 3721 (2018).

[Bau94] J. J. Baumberg, D. D. Awschalom, N. Samarth, H. Luo, and J. K. Furdyna, *Spin beats and dynamical magnetization in quantum structures*, Phys. Rev. Lett. **72**, 717–720 (1994).

[Ben00] O. Benson, C. Santori, M. Pelton, and Y. Yamamoto, *Regulated and Entangled Photons from a Single Quantum Dot*, Phys. Rev. Lett. **84**, 2513–2516 (2000).

[Ber13] T. C. Berkelbach, M. S. Hybertsen, and D. R. Reichman, *Theory of neutral and charged excitons in monolayer transition metal dichalcogenides*, Phys. Rev. B **88**, 045318 (2013).

[Bla07] P. Blake, E. W. Hill, A. H. Castro Neto, K. S. Novoselov, D. Jiang, R. Yang, T. J. Booth, and A. K. Geim, *Making graphene visible*, Appl. Phys. Lett. **91**, 063124 (2007).

[Bri13] L. Britnell, R. M. Ribeiro, A. Eckmann, R. Jalil, B. D. Belle, A. Mishchenko, Y. Kim, R. V. Gorbachev, T. Georgiou, S. V. Morozov, A. N. Grigorenko, A. K. Geim, C. Casiraghi, A. H. Castro Neto, and K. S. Novoselov, *Strong Light-Matter Interactions in Heterostructures of Atomically Thin Films*, Science **340**, 1311–1314 (2013).

[Bro72] R. A. Bromley, R. B. Murray, and A. D. Yoffe, *The band structures of some transition metal dichalcogenides. III. Group VIA: trigonal prism materials*, J. Phys. C Solid State Phys. **5**, 759–778 (1972).

[But98] L. V. Butov and A. I. Filin, *Anomalous transport and luminescence of indirect excitons in AlAs/GaAs coupled quantum wells as evidence for exciton condensation*, Phys. Rev. B **58**, 1980–2000 (1998).

[But99] L. V. Butov, A. A. Shashkin, V. T. Dolgopolov, K. L. Campman, and A. C. Gossard, *Magneto-optics of the spatially separated electron and hole layers in* $GaAs/Al_xGa_{1-x}As$ *coupled quantum wells*, Phys. Rev. B **60**, 8753–8758 (1999).

[Cad17] F. Cadiz, E. Courtade, C. Robert, G. Wang, Y. Shen, H. Cai, T. Taniguchi, K. Watanabe, H. Carrere, D. Lagarde, M. Manca, T. Amand, P. Renucci, S. Tongay, X. Marie, and B. Urbaszek, *Excitonic Linewidth Approaching the Homogeneous Limit in* $MoS_2$*-Based van der Waals Heterostructures*, Phys. Rev. X **7**, 021026 (2017).

[Cao12] T. Cao, G. Wang, W. Han, H. Ye, C. Zhu, J. Shi, Q. Niu, P. H. Tan, E. Wang, B. Liu, and J. Feng, *Valley-selective circular dichroism of monolayer molybdenum disulphide*, Nat. Commun. **3**, 887 (2012).

[Cao15] Y. Cao, A. Mishchenko, G. L. Yu, E. Khestanova, A. P. Rooney, E. Prestat, A. V. Kretinin, P. Blake, M. B. Shalom, C. Woods, J. Chapman, G. Balakrishnan, I. V. Grigorieva, K. S. Novoselov, B. A. Piot, M. Potemski, K. Watanabe, T. Taniguchi, S. J. Haigh, A. K. Geim, and R. V. Gorbachev, *Quality Heterostructures from Two-Dimensional Crystals Unstable in Air by Their Assembly in Inert Atmosphere*, Nano Lett. **15**, 4914–4921 (2015).

[Cas09] A. H. Castro Neto, F. Guinea, N. M. R. Peres, K. S. Novoselov, and A. K. Geim, *The electronic properties of graphene*, Rev. Mod. Phys. **81**, 109–162 (2009).

[Ceb14] F. Ceballos, M. Z. Bellus, H.-Y. Chiu, and H. Zhao, *Ultrafast Charge Separation and Indirect Exciton Formation in a $MoS_2$-$MoSe_2$ van der Waals Heterostructure*, ACS Nano **8**, 12717–12724 (2014).

[Ceb15] F. Ceballos, M. Z. Bellus, H.-Y. Chiu, and H. Zhao, *Probing charge transfer excitons in a $MoSe_2/WS_2$ van der Waals heterostructure*, Nanoscale **7**, 17523–17528 (2015).

[CG10] A. Castellanos-Gomez, N. Agraït, and G. Rubio-Bollinger, *Optical identification of atomically thin dichalcogenide crystals*, Appl. Phys. Lett. **96**, 213116 (2010).

[CG14] A. Castellanos-Gomez, M. Buscema, R. Molenaar, V. Singh, L. Janssen, H. S. J. van der Zant, and G. A. Steele, *Deterministic transfer of two-dimensional materials by all-dry viscoelastic stamping*, 2D Mater. **1**, 011002 (2014).

[Che12] T. Cheiwchanchamnangij and W. R. L. Lambrecht, *Quasiparticle band structure calculation of monolayer, bilayer, and bulk $MoS_2$*, Phys. Rev. B **85**, 205302 (2012).

[Che14a] R. Cheng, D. Li, H. Zhou, C. Wang, A. Yin, S. Jiang, Y. Liu, Y. Chen, Y. Huang, and X. Duan, *Electroluminescence and Photocurrent Generation from Atomically Sharp $WSe_2/MoS_2$ Heterojunction p-n Diodes*, Nano Lett. **14**, 5590–5597 (2014).

[Che14b] A. Chernikov, T. C. Berkelbach, H. M. Hill, A. Rigosi, Y. Li, O. B. Aslan, D. R. Reichman, M. S. Hybertsen, and T. F. Heinz, *Exciton Binding Energy*

*and Nonhydrogenic Rydberg Series in Monolayer $WS_2$*, Phys. Rev. Lett. **113**, 076802 (2014).

[Che15] A. Chernikov, A. M. van der Zande, H. M. Hill, A. F. Rigosi, A. Velauthapillai, J. Hone, and T. F. Heinz, *Electrical Tuning of Exciton Binding Energies in Monolayer $WS_2$*, Phys. Rev. Lett. **115**, 126802 (2015).

[Che18] S.-Y. Chen, T. Goldstein, T. Taniguchi, K. Watanabe, and J. Yan, *Coulomb-bound four- and five-particle intervalley states in an atomically-thin semiconductor*, Nat. Commun. **9**, 3717 (2018).

[Chi15] M.-H. Chiu, C. Zhang, H.-W. Shiu, C.-P. Chuu, C.-H. Chen, C.-Y. S. Chang, C.-H. Chen, M.-Y. Chou, C.-K. Shih, and L.-J. Li, *Determination of band alignment in the single-layer $MoS_2/WSe_2$ heterojunction*, Nat. Commun. **6**, 7666 (2015).

[Cho70] A. Y. Cho, *Morphology of Epitaxial Growth of GaAs by a Molecular Beam Method: The Observation of Surface Structures*, J. Appl. Phys. **41**, 2780–2786 (1970).

[Cit94] D. S. Citrin, *Long radiative lifetimes of biexcitons in $GaAs/Al_xGa_{1-x}As$ quantum wells*, Phys. Rev. B **50**, 17655–17658 (1994).

[Cou17] E. Courtade, M. Semina, M. Manca, M. M. Glazov, C. Robert, F. Cadiz, G. Wang, T. Taniguchi, K. Watanabe, M. Pierre, W. Escoffier, E. L. Ivchenko, P. Renucci, X. Marie, T. Amand, and B. Urbaszek, *Charged excitons in monolayer $WSe_2$: Experiment and theory*, Phys. Rev. B **96**, 085302 (2017).

[Dal15] S. Dal Conte, F. Bottegoni, E. A. A. Pogna, D. De Fazio, S. Ambrogio, I. Bargigia, C. D'Andrea, A. Lombardo, M. Bruna, F. Ciccacci, A. C. Ferrari, G. Cerullo, and M. Finazzi, *Ultrafast valley relaxation dynamics in monolayer $MoS_2$ probed by nonequilibrium optical techniques*, Phys. Rev. B **92**, 235425 (2015).

[Dan17] M. Danovich, V. Zólyomi, and V. I. Fal'ko, *Dark trions and biexcitons in $WS_2$ and $WSe_2$ made bright by e-e scattering*, Sci. Rep. **7**, 45998 (2017).

[Dav09] D. H. Davies, *The physics of low-dimensional semiconductors*, Cambridge University Press, 2009.

[Dea10] C. R. Dean, A. F. Young, I. Meric, C. Lee, L. Wang, S. Sorgenfrei, K. Watanabe, T. Taniguchi, P. Kim, K. L. Shepard, and J. Hone, *Boron nitride substrates for high-quality graphene electronics.*, Nat. Nanotech. **5**, 722–726 (2010).

[Dey16] P. Dey, J. Paul, Z. Wang, C. E. Stevens, C. Liu, A. H. Romero, J. Shan, D. J. Hilton, and D. Karaiskaj, *Optical Coherence in Atomic-Monolayer Transition-Metal Dichalcogenides Limited by Electron-Phonon Interactions*, Phys. Rev. Lett. **116**, 127402 (2016).

[Dic23] R. G. Dickinson and L. Pauling, *The crystal structure of molybdenite*, J. Am. Chem. Soc. **45**, 1466–1471 (1923).

[Drü17] M. Drüppel, T. Deilmann, P. Krüger, and M. Rohlfing, *Diversity of trion states and substrate effects in the optical properties of an $MoS_2$ monolayer*, Nat. Commun. **8**, 2117 (2017).

[Fan14] H. Fang, C. Battaglia, C. Carraro, S. Nemsak, B. Ozdol, J. S. Kang, H. A. Bechtel, S. B. Desai, F. Kronast, A. A. Unal, G. Conti, C. Conlon, G. K. Palsson, M. C. Martin, A. M. Minor, C. S. Fadley, E. Yablonovitch, R. Maboudian, and A. Javey, *Strong interlayer coupling in van der Waals heterostructures built from single-layer chalcogenides*, Proc. Natl. Acad. Sci. **111**, 6198–6202 (2014).

[Fen07] X. Feng, M. A. Meitl, A. M. Bowen, Y. Huang, R. G. Nuzzo, and J. A. Rogers, *Competing Fracture in Kinetically Controlled Transfer Printing*, Langmuir **23**, 12555–12560 (2007).

[Fio14] G. Fiori, F. Bonaccorso, G. Iannaccone, T. Palacios, D. Neumaier, A. Seabaugh, S. K. Banerjee, and L. Colombo, *Electronics based on two-dimensional materials*, Nat. Nanotech. **9**, 768–779 (2014).

[Fog14] M. M. Fogler, L. V. Butov, and K. S. Novoselov, *High-temperature superfluidity with indirect excitons in van der Waals heterostructures.*, Nat. Commun. **5**, 4555 (2014).

[Fre31] J. Frenkel, *On the Transformation of light into Heat in Solids. I*, Phys. Rev. **37**, 17–44 (1931).

[Fri18a] R. Frisenda, A. J. Molina-Mendoza, T. Mueller, A. Castellanos-Gomez, and H. S. J. van der Zant, *Atomically thin p-n junctions based on two-dimensional materials*, Chem. Soc. Rev. **47**, 3339–3358 (2018).

[Fri18b] R. Frisenda, E. Navarro-Moratalla, P. Gant, D. Pérez De Lara, P. Jarillo-Herrero, R. V. Gorbachev, and A. Castellanos-Gomez, *Recent progress in the assembly of nanodevices and van der Waals heterostructures by deterministic placement of 2D materials*, Chem. Soc. Rev. **47**, 53–68 (2018).

[Fur14] M. M. Furchi, A. Pospischil, F. Libisch, J. Burgdörfer, and T. Mueller, *Photovoltaic Effect in an Electrically Tunable van der Waals Heterojunction*, Nano Lett. **14**, 4785–4791 (2014).

[Gei13] A. K. Geim and I. V. Grigorieva, *Van der Waals heterostructures*, Nature **499**, 419–425 (2013).

[Gla14] M. M. Glazov, T. Amand, X. Marie, D. Lagarde, L. Bouet, and B. Urbaszek, *Exciton fine structure and spin decoherence in monolayers of transition metal dichalcogenides*, Phys. Rev. B **89**, 201302(R) (2014).

[God16] T. Godde, D. Schmidt, J. Schmutzler, M. Aßmann, J. Debus, F. Withers, E. M. Alexeev, O. Del Pozo-Zamudio, O. V. Skrypka, K. S. Novoselov, M. Bayer, and A. I. Tartakovskii, *Exciton and trion dynamics in atomically thin $MoSe_2$ and $WSe_2$: Effect of localization*, Phys. Rev. B **94**, 165301 (2016).

[Gon17] C. Gong, L. Li, Z. Li, H. Ji, A. Stern, Y. Xia, T. Cao, W. Bao, C. Wang, Y. Wang, Z. Q. Qiu, R. J. Cava, S. G. Louie, J. Xia, and X. Zhang, *Discovery of intrinsic ferromagnetism in two-dimensional van der Waals crystals*, Nature **546**, 265–269 (2017).

[Gou79] P. L. Gourley and J. P. Wolfe, *Thermodynamics of excitonic molecules in silicon*, Phys. Rev. B **20**, 3319–3327 (1979).

[Gou97] E. Gourmelon, O. Lignier, H. Hadouda, G. Couturier, J. C. Bernède, J. Tedd, J. Pouzet, and J. Salardenne, *$MS_2$ (M=W, Mo) photosensitive thin films for solar cells*, Sol. Energy Mater. Sol. Cells **46**, 115–121 (1997).

[Hai12] S. J. Haigh, A. Gholinia, R. Jalil, S. Romani, L. Britnell, D. C. Elias, K. S. Novoselov, L. A. Ponomarenko, A. K. Geim, and R. Gorbachev, *Cross-sectional imaging of individual layers and buried interfaces of graphene-based heterostructures and superlattices*, Nat. Mater. **11**, 764–767 (2012).

[Hao16] K. Hao, L. Xu, P. Nagler, A. Singh, K. Tran, C. K. Dass, C. Schüller, T. Korn, X. Li, and G. Moody, *Coherent and Incoherent Coupling Dynamics between Neutral and Charged Excitons in Monolayer $MoSe_2$*, Nano Lett. **16**, 5109–5113 (2016).

[Hao17a] K. Hao, J. F. Specht, P. Nagler, L. Xu, K. Tran, A. Singh, C. K. Dass, C. Schüller, T. Korn, M. Richter, A. Knorr, X. Li, and G. Moody, *Neutral and charged inter-valley biexcitons in monolayer $MoSe_2$*, Nat. Commun. **8**, 15552 (2017).

[Hao17b] K. Hao, L. Xu, F. Wu, P. Nagler, K. Tran, X. Ma, C. Schüller, T. Korn, A. H. MacDonald, G. Moody, and X. Li, *Trion valley coherence in monolayer semiconductors*, 2D Mater. **4**, 025105 (2017).

[He14] K. He, N. Kumar, L. Zhao, Z. Wang, K. F. Mak, H. Zhao, and J. Shan, *Tightly Bound Excitons in $WSe_2$*, Phys. Rev. Lett. **113**, 026803 (2014).

[He16a] Y.-M. He, O. Iff, N. Lundt, V. Baumann, M. Davanco, K. Srinivasan, S. Höfling, and C. Schneider, *Cascaded emission of single photons from the biexciton in monolayered $WSe_2$*, Nat. Commun. **7**, 13409 (2016).

[He16b] Z. He, W. Xu, Y. Zhou, X. Wang, Y. Sheng, Y. Rong, S. Guo, J. Zhang, J. M. Smith, and J. H. Warner, *Biexciton Formation in Bilayer Tungsten Disulfide*, ACS Nano **10**, 2176–2183 (2016).

[Her03] F. Herlach and N. Miura, *High Magnetic Fields; Science and Technology*, World Scientific, 2003.

[Hil15] H. M. Hill, A. F. Rigosi, C. Roquelet, A. Chernikov, T. C. Berkelbach, D. R. Reichman, M. S. Hybertsen, L. E. Brus, and T. F. Heinz, *Observation of Excitonic Rydberg States in Monolayer $MoS_2$ and $WS_2$ by Photoluminescence Excitation Spectroscopy*, Nano Lett. **15**, 2992–2997 (2015).

[Hil16] H. M. Hill, A. F. Rigosi, K. T. Rim, G. W. Flynn, and T. F. Heinz, *Band Alignment in $MoS_2/WS_2$ Transition Metal Dichalcogenide Heterostructures Probed by Scanning Tunneling Microscopy and Spectroscopy*, Nano Lett. **16**, 4831–4837 (2016).

[Hon14] X. Hong, J. Kim, S.-F. Shi, Y. Zhang, C. Jin, Y. Sun, S. Tongay, J. Wu, Y. Zhang, and F. Wang, *Ultrafast charge transfer in atomically thin $MoS_2/WS_2$ heterostructures*, Nat. Nanotech. **9**, 682–686 (2014).

[Hsu14] W.-T. Hsu, Z.-A. Zhao, L.-J. Li, C.-H. Chen, M.-H. Chiu, P.-S. Chang, Y.-C. Chou, and W.-H. Chang, *Second Harmonic Generation from Artificially Stacked Transition Metal Dichalcogenide Twisted Bilayers*, ACS Nano **8**, 2951–2958 (2014).

[Hsu18] W.-T. Hsu, L.-S. Lu, P.-H. Wu, M.-H. Lee, P.-J. Chen, P.-Y. Wu, Y.-C. Chou, H.-T. Jeng, L.-J. Li, M.-W. Chu, and W.-H. Chang, *Negative circular polarization emissions from $WSe_2/MoSe_2$ commensurate heterobilayers*, Nat. Commun. **9**, 1356 (2018).

[Hua16] J. Huang, T. B. Hoang, and M. H. Mikkelsen, *Probing the origin of excitonic states in monolayer $WSe_2$*, Sci. Rep. **6**, 22414 (2016).

[Hua17] B. Huang, G. Clark, E. Navarro-Moratalla, D. R. Klein, R. Cheng, K. L. Seyler, D. Zhong, E. Schmidgall, M. A. McGuire, D. H. Cobden, W. Yao, D. Xiao, P. Jarillo-Herrero, and X. Xu, *Layer-dependent ferromagnetism in a van der Waals crystal down to the monolayer limit*, Nature **546**, 270–273 (2017).

[Imh10] S. Imhof, A. Thränhardt, A. Chernikov, M. Koch, N. S. Köster, K. Kolata, S. Chatterjee, S. W. Koch, X. Lu, S. R. Johnson, D. A. Beaton, T. Tiedje, and O. Rubel, *Clustering effects in Ga(AsBi)*, Appl. Phys. Lett. **96**, 131115 (2010).

[Imh11] S. Imhof, C. Wagner, A. Thränhardt, A. Chernikov, M. Koch, N. S. Köster, S. Chatterjee, S. W. Koch, O. Rubel, X. Lu, S. R. Johnson, D. A. Beaton, and T. Tiedje, *Luminescence dynamics in Ga(AsBi)*, Appl. Phys. Lett. **98**, 161104 (2011).

[Jak16] T. Jakubczyk, V. Delmonte, M. Koperski, K. Nogajewski, C. Faugeras, W. Langbein, M. Potemski, and J. Kasprzak, *Radiatively Limited Dephasing and Exciton Dynamics in $MoSe_2$ Monolayers Revealed with Four-Wave Mixing Microscopy*, Nano Lett. **16**, 5333–5339 (2016).

[Jan15] C. Janisch, Y. Wang, D. Ma, N. Mehta, A. L. Elías, N. Perea-López, M. Terrones, V. Crespi, and Z. Liu, *Extraordinary Second Harmonic Generation in Tungsten Disulfide Monolayers*, Sci. Rep. **4**, 5530 (2015).

[Job16] J. Jobst, A. J. H. van der Torren, E. E. Krasovskii, J. Balgley, C. R. Dean, R. M. Tromp, and S. J. van der Molen, *Quantifying electronic band interactions*

*in van der Waals materials using angle-resolved reflected-electron spectroscopy*, Nat. Commun. **7**, 13621 (2016).

[Jon13] A. M. Jones, H. Yu, N. J. Ghimire, S. Wu, G. Aivazian, J. S. Ross, B. Zhao, J. Yan, D. G. Mandrus, D. Xiao, W. Yao, and X. Xu, *Optical generation of excitonic valley coherence in monolayer $WSe_2$*, Nat. Nanotech. **8**, 634–638 (2013).

[Jon15] A. M. Jones, H. Yu, J. R. Schaibley, J. Yan, D. G. Mandrus, T. Taniguchi, K. Watanabe, H. Dery, W. Yao, and X. Xu, *Excitonic luminescence upconversion in a two-dimensional semiconductor*, Nat. Phys. **12**, 323–327 (2015).

[Kai03] R. A. Kaindl, M. A. Carnahan, D. Hägele, R. Lövenich, and D. S. Chemla, *Ultrafast terahertz probes of transient conducting and insulating phases in an electron-hole gas*, Nature **423**, 734–738 (2003).

[Kel79] L. V. Keldysh, *Coulomb interaction in thin semiconductor and semimetal films*, Sov. J. Exp. Theor. Phys. Lett. **29**, 658–660 (1979).

[Kid16] D. W. Kidd, D. K. Zhang, and K. Varga, *Binding energies and structures of two-dimensional excitonic complexes in transition metal dichalcogenides*, Phys. Rev. B **93**, 125423 (2016).

[Kim94] J. C. Kim, D. R. Wake, and J. P. Wolfe, *Thermodynamics of biexcitons in a GaAs quantum well*, Phys. Rev. B **50**, 15099–15107 (1994).

[Kim16] M. S. Kim, S. J. Yun, Y. Lee, C. Seo, G. H. Han, K. K. Kim, Y. H. Lee, and J. Kim, *Biexciton Emission from Edges and Grain Boundaries of Triangular $WS_2$ Monolayers*, ACS Nano **10**, 2399–2405 (2016).

[Kio12] G. Kioseoglou, A. T. Hanbicki, M. Currie, A. L. Friedman, D. Gunlycke, and B. T. Jonker, *Valley polarization and intervalley scattering in monolayer $MoS_2$*, Appl. Phys. Lett. **101**, 221907 (2012).

[Kio16] G. Kioseoglou, A. T. Hanbicki, M. Currie, A. L. Friedman, and B. T. Jonker, *Optical polarization and intervalley scattering in single layers of $MoS_2$ and $MoSe_2$*, Sci. Rep. **6**, 25041 (2016).

[Kli80] K. v. Klitzing, G. Dorda, and M. Pepper, *New Method for High-Accuracy Determination of the Fine-Structure Constant Based on Quantized Hall Resistance*, Phys. Rev. Lett. **45**, 494–497 (1980).

[Kli12] C. F. Klingshirn, *Semiconductor Optics*, Graduate Texts in Physics, Springer, Berlin, 2012.

[Klo15] A. R. Klots, A. K. M. Newaz, B. Wang, D. Prasai, H. Krzyzanowska, J. Lin, D. Caudel, N. J. Ghimire, J. Yan, B. L. Ivanov, K. A. Velizhanin, A. Burger, D. G. Mandrus, N. H. Tolk, S. T. Pantelides, and K. I. Bolotin, *Probing excitonic states in suspended two-dimensional semiconductors by photocurrent spectroscopy*, Sci. Rep. **4**, 6608 (2015).

[Kom13] H.-P. Komsa and A. V. Krasheninnikov, *Electronic structures and optical properties of realistic transition metal dichalcogenide heterostructures from first principles*, Phys. Rev. B **88**, 085318 (2013).

[Kor11] T. Korn, S. Heydrich, M. Hirmer, J. Schmutzler, and C. Schüller, *Low-temperature photocarrier dynamics in monolayer $MoS_2$*, Appl. Phys. Lett. **99**, 102109 (2011).

[Kor14] A. Kormányos, V. Zólyomi, N. D. Drummond, and G. Burkard, *Spin-Orbit Coupling, Quantum Dots, and Qubits in Monolayer Transition Metal Dichalcogenides*, Phys. Rev. X **4**, 011034 (2014).

[Kor15] A. Kormányos, G. Burkard, M. Gmitra, J. Fabian, V. Zólyomi, N. D. Drummond, and V. Fal'ko, *$k \cdot p$ theory for two-dimensional transition metal dichalcogenide semiconductors*, 2D Mater. **2**, 022001 (2015).

[Koś13] K. Kośmider, J. W. González, and J. Fernández-Rossier, *Large spin splitting in the conduction band of transition metal dichalcogenide monolayers*, Phys. Rev. B **88**, 245436 (2013).

[Kuc11] A. Kuc, N. Zibouche, and T. Heine, *Influence of quantum confinement on the electronic structure of the transition metal sulfide $TS_2$*, Phys. Rev. B **83**, 245213 (2011).

[Kuh17] J. Kuhnert, A. Rahimi-Iman, and W. Heimbrodt, *Magneto photoluminescence measurements of tungsten disulphide monolayers*, J. Phys. Condens. Matter **29**, 8 (2017).

[Kul18] M. Kulig, J. Zipfel, P. Nagler, S. Blanter, C. Schüller, T. Korn, N. Paradiso, M. M. Glazov, and A. Chernikov, *Exciton Diffusion and Halo Effects in Monolayer Semiconductors*, Phys. Rev. Lett. **120**, 207401 (2018).

[Kum12] A. Kumar and P. K. Ahluwalia, *Tunable dielectric response of transition metals dichalcogenides $MX_2$ (M=Mo,W; X=S,Se,Te): Effect of quantum confinement*, Phys. B Condens. Matter **407**, 4627–4634 (2012).

[Kun18] J. Kunstmann, F. Mooshammer, P. Nagler, A. Chaves, F. Stein, N. Paradiso, G. Plechinger, C. Strunk, C. Schüller, G. Seifert, D. R. Reichman, and T. Korn, *Momentum-space indirect interlayer excitons in transition-metal dichalcogenide van der Waals heterostructures*, Nat. Phys. **14**, 801–805 (2018).

[Kyl15] I. Kylänpää and H.-P. Komsa, *Binding energies of exciton complexes in transition metal dichalcogenide monolayers and effect of dielectric environment*, Phys. Rev. B **92**, 205418 (2015).

[Lag14] D. Lagarde, L. Bouet, X. Marie, C. R. Zhu, B. L. Liu, T. Amand, P. H. Tan, and B. Urbaszek, *Carrier and Polarization Dynamics in Monolayer $MoS_2$*, Phys. Rev. Lett. **112**, 047401 (2014).

[Lai09] B. Laikhtman and R. Rapaport, *Exciton correlations in coupled quantum wells and their luminescence blue shift*, Phys. Rev. B **80**, 195313 (2009).

[Lan16] F. Langer, M. Hohenleutner, C. P. Schmid, C. Poellmann, P. Nagler, T. Korn, C. Schüller, M. S. Sherwin, U. Huttner, J. T. Steiner, S. W. Koch, M. Kira, and R. Huber, *Lightwave-driven quasiparticle collisions on a subcycle timescale*, Nature **533**, 225–229 (2016).

[Lan18] F. Langer, C. P. Schmid, S. Schlauderer, M. Gmitra, J. Fabian, P. Nagler, C. Schüller, T. Korn, P. G. Hawkins, J. T. Steiner, U. Huttner, S. W. Koch, M. Kira, and R. Huber, *Lightwave valleytronics in a monolayer of tungsten diselenide*, Nature **557**, 76–80 (2018).

[Lat17] S. Latini, K. T. Winther, T. Olsen, and K. S. Thygesen, *Interlayer Excitons and Band Alignment in $MoS_2$/hBN/$WSe_2$ van der Waals Heterostructures*, Nano Lett. **17**, 938–945 (2017).

[Leb09] S. Lebègue and O. Eriksson, *Electronic structure of two-dimensional crystals from ab initio theory*, Phys. Rev. B **79**, 115409 (2009).

[Lee14] C.-H. Lee, G.-H. Lee, A. M. van der Zande, W. Chen, Y. Li, M. Han, X. Cui, G. Arefe, C. Nuckolls, T. F. Heinz, J. Guo, J. Hone, and P. Kim, *Atomically thin p-n junctions with van der Waals heterointerfaces*, Nat. Nanotech. **9**, 676–681 (2014).

[Lee16] H. S. Lee, M. S. Kim, H. Kim, and Y. H. Lee, *Identifying multiexcitons in $MoS_2$ monolayers at room temperature*, Phys. Rev. B **93**, 140409(R) (2016).

[Li07] T. Li and G. Galli, *Electronic Properties of $MoS_2$ Nanoparticles*, J. Phys. Chem. C **111**, 16192–16196 (2007).

[Li13] Y. Li, Y. Rao, K. F. Mak, Y. You, S. Wang, C. R. Dean, and T. F. Heinz, *Probing Symmetry Properties of Few-Layer $MoS_2$ and h-BN by Optical Second-Harmonic Generation*, Nano Lett. **13**, 3329–3333 (2013).

[Li14a] Y. Li, A. Chernikov, X. Zhang, A. Rigosi, H. M. Hill, A. M. van der Zande, D. A. Chenet, E.-M. Shih, J. Hone, and T. F. Heinz, *Measurement of the optical dielectric function of monolayer transition-metal dichalcogenides: $MoS_2$, $MoSe_2$, $WS_2$, and $WSe_2$*, Phys. Rev. B **90**, 205422 (2014).

[Li14b] Y. Li, J. Ludwig, T. Low, A. Chernikov, X. Cui, G. Arefe, Y. D. Kim, A. M. van der Zande, A. Rigosi, H. M. Hill, S. H. Kim, J. Hone, Z. Li, D. Smirnov, and T. F. Heinz, *Valley Splitting and Polarization by the Zeeman Effect in Monolayer $MoSe_2$*, Phys. Rev. Lett. **113**, 266804 (2014).

[Li17] L. Li, R. Long, and O. V. Prezhdo, *Charge Separation and Recombination in Two-Dimensional $MoS_2/WS_2$: Time-Domain ab Initio Modeling*, Chem. Mater. **29**, 2466–2473 (2017).

[Li18] Z. Li, T. Wang, Z. Lu, C. Jin, Y. Chen, Y. Meng, Z. Lian, T. Taniguchi, K. Watanabe, S. Zhang, D. Smirnov, and S.-F. Shi, *Revealing the biexciton and trion-exciton complexes in BN encapsulated $WSe_2$*, Nat. Commun. **9**, 3719 (2018).

[Lia13] Y. Liang, S. Huang, R. Soklaski, and L. Yang, *Quasiparticle band-edge energy and band offsets of monolayer of molybdenum and tungsten chalcogenides*, Appl. Phys. Lett. **103**, 042106 (2013).

[Liu13] G.-B. Liu, W.-Y. Shan, Y. Yao, W. Yao, and D. Xiao, *Three-band tight-binding model for monolayers of group-VIB transition metal dichalcogenides*, Phys. Rev. B **88**, 085433 (2013).

[Liu15] G.-B. Liu, D. Xiao, Y. Yao, X. Xu, and W. Yao, *Electronic structures and theoretical modelling of two-dimensional group-VIB transition metal dichalcogenides*, Chem. Soc. Rev. **44**, 2643–2663 (2015).

[Lon16] M. Long, E. Liu, P. Wang, A. Gao, H. Xia, W. Luo, B. Wang, J. Zeng, Y. Fu, K. Xu, W. Zhou, Y. Lv, S. Yao, M. Lu, Y. Chen, Z. Ni, Y. You, X. Zhang, S. Qin, Y. Shi, W. Hu, D. Xing, and F. Miao, *Broadband Photovoltaic Detectors Based on an Atomically Thin Heterostructure*, Nano Lett. **16**, 2254–2259 (2016).

[LS14] O. Lopez-Sanchez, E. Alarcon Llado, V. Koman, A. Fontcuberta i Morral, A. Radenovic, and A. Kis, *Light Generation and Harvesting in a van der Waals Heterostructure*, ACS Nano **8**, 3042–3048 (2014).

[Mac15] D. MacNeill, C. Heikes, K. F. Mak, Z. Anderson, A. Kormányos, V. Zólyomi, J. Park, and D. C. Ralph, *Breaking of valley degeneracy by magnetic field in monolayer $MoSe_2$*, Phys. Rev. Lett. **114**, 037401 (2015).

[Mai14] C. Mai, A. Barrette, Y. Yu, Y. G. Semenov, K. W. Kim, L. Cao, and K. Gundogdu, *Many-Body Effects in Valleytronics: Direct Measurement of Valley Lifetimes in Single-Layer $MoS_2$*, Nano Lett. **14**, 202–206 (2014).

[Mak10] K. F. Mak, C. Lee, J. Hone, J. Shan, and T. F. Heinz, *Atomically Thin $MoS_2$: A New Direct-Gap Semiconductor*, Phys. Rev. Lett. **105**, 136805 (2010).

[Mak12] K. F. Mak, K. He, J. Shan, and T. F. Heinz, *Control of valley polarization in monolayer $MoS_2$ by optical helicity*, Nat. Nanotech. **7**, 494–498 (2012).

[Mak13] K. F. Mak, K. He, C. Lee, G. H. Lee, J. Hone, T. F. Heinz, and J. Shan, *Tightly bound trions in monolayer $MoS_2$*, Nat. Mater. **12**, 207–211 (2013).

[Mak14] K. F. Mak, K. L. McGill, J. Park, and P. L. McEuen, *The valley Hall effect in $MoS_2$ transistors*, Science **344**, 1489–1492 (2014).

[Mal13] L. M. Malard, T. V. Alencar, A. P. M. Barboza, K. F. Mak, and A. M. de Paula, *Observation of intense second harmonic generation from $MoS_2$ atomic crystals*, Phys. Rev. B **87**, 201401(R) (2013).

[Man17] M. Manca, M. M. Glazov, C. Robert, F. Cadiz, T. Taniguchi, K. Watanabe, E. Courtade, T. Amand, P. Renucci, X. Marie, G. Wang, and B. Urbaszek, *Enabling valley selective exciton scattering in monolayer $WSe_2$ through upconversion*, Nat. Commun. **8**, 14927 (2017).

[Mar17] K. Marinov, A. Avsar, K. Watanabe, T. Taniguchi, and A. Kis, *Resolving the spin splitting in the conduction band of monolayer $MoS_2$*, Nat. Commun. **8**, 1938 (2017).

[Mas15] M. Massicotte, P. Schmidt, F. Vialla, K. G. Schädler, A. Reserbat-Plantey, K. Watanabe, T. Taniguchi, K. J. Tielrooij, and F. H. L. Koppens, *Picosecond photoresponse in van der Waals heterostructures*, Nat. Nanotech. **11**, 42–46 (2015).

[Mas18] S. Masubuchi, M. Morimoto, S. Morikawa, M. Onodera, Y. Asakawa, K. Watanabe, T. Taniguchi, and T. Machida, *Autonomous robotic searching and assembly of two-dimensional crystals to build van der Waals superlattices*, Nat. Commun. **9**, 1413 (2018).

[Mat73a] L. F. Mattheiss, *Band Structures of Transition-Metal-Dichalcogenide Layer Compounds*, Phys. Rev. B **8**, 3719–3740 (1973).

[Mat73b] L. F. Mattheiss, *Energy Bands for 2H-$NbSe_2$ and 2H-$MoS_2$*, Phys. Rev. Lett. **30**, 784–787 (1973).

[May15] M. Z. Mayers, T. C. Berkelbach, M. S. Hybertsen, and D. R. Reichman, *Binding energies and spatial structures of small carrier complexes in monolayer transition-metal dichalcogenides via diffusion Monte Carlo*, Phys. Rev. B **92**, 161404(R) (2015).

[Mei06] M. A. Meitl, Z.-T. Zhu, V. Kumar, K. J. Lee, X. Feng, Y. Y. Huang, I. Adesida, R. G. Nuzzo, and J. A. Rogers, *Transfer printing by kinetic control of adhesion to an elastomeric stamp*, Nat. Mater. **5**, 33–38 (2006).

[Mer18] P. Merkl, P. Steinleitner, F. Mooshammer, K. Lin, P. Nagler, J. Holler, C. Schüller, J. M. Lupton, T. Korn, S. Ovesen, S. Brem, E. Malic, and R. Huber, *Ultrafast transition between exciton phases in van der Waals heterostructures*, submitted (2018).

[Mit99] V. Mitin, V. Kochelap, and M. A. Stroscio, *Quantum heterostructures: Microelectronics and Optoelectronic*, Cambridge University Press, 1999.

[Mit15] A. A. Mitioglu, P. Plochocka, A. Granados del Águila, P. C. M. Christianen, G. Deligeorgis, S. Anghel, L. Kulyuk, and D. K. Maude, *Optical Investigation of Monolayer and Bulk Tungsten Diselenide ($WSe_2$) in High Magnetic Fields*, Nano Lett. **15**, 4387–4392 (2015).

[Mit16] A. A. Mitioglu, K. Galkowski, A. Surrente, L. Klopotowski, D. Dumcenco, A. Kis, D. K. Maude, and P. Plochocka, *Magnetoexcitons in large area CVD-grown monolayer $MoS_2$ and $MoSe_2$ on sapphire*, Phys. Rev. B **93**, 165412 (2016).

[Miu07] N. Miura, *Physics of Semiconductors in High Magnetic Fields*, Oxford University Press, 2007.

[Miw15] J. A. Miwa, S. Ulstrup, S. G. Sørensen, M. Dendzik, A. G. Čabo, M. Bianchi, J. V. Lauritsen, and P. Hofmann, *Electronic Structure of Epitaxial Single-Layer $MoS_2$*, Phys. Rev. Lett. **114**, 046802 (2015).

[Mol17] M. R. Molas, C. Faugeras, A. O. Slobodeniuk, K. Nogajewski, M. Bartos, D. M. Basko, and M. Potemski, *Brightening of dark excitons in monolayers of semiconducting transition metal dichalcogenides*, 2D Mater. **4**, 021003 (2017).

[Moo15a] G. Moody, C. K. Dass, K. Hao, C.-H. Chen, L.-J. Li, A. Singh, K. Tran, G. Clark, X. Xu, G. Berghäuser, E. Malic, A. Knorr, and X. Li, *Intrinsic homogeneous linewidth and broadening mechanisms of excitons in monolayer transition metal dichalcogenides*, Nat. Commun. **6**, 8315 (2015).

[Moo15b] F. Mooshammer, *Twist-induced tuning of interlayer coupling in $MoS_2/WSe_2$ heterostructures*, 2015.

[Moo16] G. Moody, J. Schaibley, and X. Xu, *Exciton dynamics in monolayer transition metal dichalcogenides*, J. Opt. Soc. Am. B **33**, C39 (2016).

[Mou17] S. Mouri, W. Zhang, D. Kozawa, Y. Miyauchi, G. Eda, and K. Matsuda, *Thermal dissociation of inter-layer excitons in $MoS_2/MoSe_2$ hetero-bilayers*, Nanoscale **9**, 6674–6679 (2017).

[MS13] A. Molina-Sánchez, D. Sangalli, K. Hummer, A. Marini, and L. Wirtz, *Effect of spin-orbit interaction on the optical spectra of single-layer, double-layer, and bulk $MoS_2$*, Phys. Rev. B **88**, 045412 (2013).

[Nag17a] P. Nagler, M. V. Ballottin, A. A. Mitioglu, F. Mooshammer, N. Paradiso, C. Strunk, R. Huber, A. Chernikov, P. C. M. Christianen, C. Schüller, and T. Korn, *Giant magnetic splitting inducing near-unity valley polarization in van der Waals heterostructures*, Nat. Commun. **8**, 1551 (2017).

[Nag17b] P. Nagler, G. Plechinger, M. V. Ballottin, A. A. Mitioglu, S. Meier, N. Paradiso, C. Strunk, A. Chernikov, P. C. M. Christianen, C. Schüller, and T. Korn, *Interlayer exciton dynamics in a dichalcogenide monolayer heterostructure*, 2D Mater. **4**, 025112 (2017).

[Nag18] P. Nagler, M. V. Ballottin, A. A. Mitioglu, M. V. Durnev, T. Taniguchi, K. Watanabe, A. Chernikov, C. Schüller, M. M. Glazov, P. C. M. Christianen, and T. Korn, *Zeeman Splitting and Inverted Polarization of Biexciton Emission in Monolayer $WS_2$*, Phys. Rev. Lett. **121**, 057402 (2018).

[Nay17] P. K. Nayak, Y. Horbatenko, S. Ahn, G. Kim, J.-U. Lee, K. Y. Ma, A.-R. Jang, H. Lim, D. Kim, S. Ryu, H. Cheong, N. Park, and H. S. Shin, *Probing Evolution of Twist-Angle-Dependent Interlayer Excitons in $MoSe_2/WSe_2$ van der Waals Heterostructures*, ACS Nano **11**, 4041–4050 (2017).

[Nov04] K. S. Novoselov, A. K. Geim, S. V. Morozov, D. Jiang, Y. Zhang, S. V. Dubonos, I. V. Grigorieva, and A. A. Firsov, *Electric Field Effect in Atomically Thin Carbon Films*, Science **306**, 666–669 (2004).

[Nov05a] K. S. Novoselov, A. K. Geim, S. V. Morozov, D. Jiang, M. I. Katsnelson, I. V. Grigorieva, S. V. Dubonos, and A. A. Firsov, *Two-dimensional gas of massless Dirac fermions in graphene*, Nature **438**, 197–200 (2005).

[Nov05b] K. S. Novoselov, D. Jiang, F. Schedin, T. J. Booth, V. V. Khotkevich, S. V. Morozov, and A. K. Geim, *Two-dimensional atomic crystals*, Proc. Natl. Acad. Sci. **102**, 10451–10453 (2005).

[Nov16] K. S. Novoselov, A. Mishchenko, A. Carvalho, and A. H. Castro Neto, *2D materials and van der Waals heterostructures*, Science **353**, 461–471 (2016).

[Oka17] M. Okada, Y. Miyauchi, K. Matsuda, T. Taniguchi, K. Watanabe, H. Shinohara, and R. Kitaura, *Observation of biexcitonic emission at extremely low power density in tungsten disulfide atomic layers grown on hexagonal boron nitride*, Sci. Rep. **7**, 322 (2017).

[Özç16] V. O. Özçelik, J. G. Azadani, C. Yang, S. J. Koester, and T. Low, *Band alignment of two-dimensional semiconductors for designing heterostructures with momentum space matching*, Phys. Rev. B **94**, 035125 (2016).

[Pal15] M. Palummo, M. Bernardi, and J. C. Grossman, *Exciton Radiative Lifetimes in Two-Dimensional Transition Metal Dichalcogenides*, Nano Lett. **15**, 2794–2800 (2015).

[Par17] I. Paradisanos, S. Germanis, N. T. Pelekanos, C. Fotakis, E. Kymakis, G. Kioseoglou, and E. Stratakis, *Room temperature observation of biexcitons in exfoliated $WS_2$ monolayers*, Appl. Phys. Lett. **110**, 193102 (2017).

[Päs97] R. Pässler, *Basic Model Relations for Temperature Dependencies of Fundamental Energy Gaps in Semiconductors*, Phys. Status Solidi **200**, 155–172 (1997).

[Pen16] B. Peng, G. Yu, X. Liu, B. Liu, X. Liang, L. Bi, L. Deng, T. C. Sum, and K. P. Loh, *Ultrafast charge transfer in $MoS_2/WSe_2$ p-n Heterojunction*, 2D Mater. **3**, 025020 (2016).

[Ple14] G. Plechinger, P. Nagler, C. Schüller, and T. Korn, *Time-resolved Kerr rotation spectroscopy of valley dynamics in single-layer $MoS_2$*, arXiv:1404.7674v3 (2014).

[Ple15] G. Plechinger, P. Nagler, J. Kraus, N. Paradiso, C. Strunk, C. Schüller, and T. Korn, *Identification of excitons, trions and biexcitons in single-layer $WS_2$*, Phys. Status Solidi-Rapid Res. Lett. **9**, 457–461 (2015).

[Ple16a] G. Plechinger, *Valley-Effekte und exzitonische Eigenschaften von zweidimensionalen Übergangsmetall-Dichalcogeniden*, Doktorarbeit, Universität Regensburg, 2016.

[Ple16b] G. Plechinger, P. Nagler, A. Arora, A. Granados del Águila, M. V. Ballottin, T. Frank, P. Steinleitner, M. Gmitra, J. Fabian, P. C. M. Christianen, R. Bratschitsch, C. Schüller, and T. Korn, *Excitonic Valley Effects in Monolayer $WS_2$ under High Magnetic Fields*, Nano Lett. **16**, 7899–7904 (2016).

[Ple16c] G. Plechinger, P. Nagler, A. Arora, R. Schmidt, A. Chernikov, A. Granados del Águila, P. C. M. Christianen, R. Bratschitsch, C. Schüller, and T. Korn, *Trion fine structure and coupled spin-valley dynamics in monolayer tungsten disulfide*, Nat. Commun. **7**, 12715 (2016).

[Ple17] G. Plechinger, P. Nagler, A. Arora, R. Schmidt, A. Chernikov, J. M. Lupton, R. Bratschitsch, C. Schüller, and T. Korn, *Valley dynamics of excitons in*

*monolayer dichalcogenides*, Phys. Status Solidi-Rapid Res. Lett. **11**, 1700131 (2017).

[Poe15] C. Poellmann, P. Steinleitner, U. Leierseder, P. Nagler, G. Plechinger, M. Porer, R. Bratschitsch, C. Schüller, T. Korn, and R. Huber, *Resonant internal quantum transitions and femtosecond radiative decay of excitons in monolayer $WSe_2$*, Nat. Mater. **14**, 889–893 (2015).

[Pos16] A. Pospischil and T. Mueller, *Optoelectronic Devices Based on Atomically Thin Transition Metal Dichalcogenides*, Appl. Sci. **6**, 78 (2016).

[Qiu13] D. Y. Qiu, F. H. da Jornada, and S. G. Louie, *Optical Spectrum of $MoS_2$: Many-Body Effects and Diversity of Exciton States*, Phys. Rev. Lett. **111**, 216805 (2013).

[Rad11] B. Radisavljevic, A. Radenovic, J. Brivio, V. Giacometti, and A. Kis, *Single-layer $MoS_2$ transistors*, Nat. Nanotech. **6**, 147–150 (2011).

[Rid13] B. K. Ridley, *Quantum Processes in Semiconductors*, Oxford University Press, 2013.

[Rig16] A. F. Rigosi, H. M. Hill, K. T. Rim, G. W. Flynn, and T. F. Heinz, *Electronic band gaps and exciton binding energies in monolayer $Mo_x W_{1-x} S_2$ transition metal dichalcogenide alloys probed by scanning tunneling and optical spectroscopy*, Phys. Rev. B **94**, 075440 (2016).

[Riv15] P. Rivera, J. R. Schaibley, A. M. Jones, J. S. Ross, S. Wu, G. Aivazian, P. Klement, K. Seyler, G. Clark, N. J. Ghimire, J. Yan, D. G. Mandrus, W. Yao, and X. Xu, *Observation of long-lived interlayer excitons in monolayer $MoSe_2$-$WSe_2$ heterostructures*, Nat. Commun. **6**, 6242 (2015).

[Riv16] P. Rivera, K. L. Seyler, H. Yu, J. R. Schaibley, J. Yan, D. G. Mandrus, W. Yao, and X. Xu, *Valley-polarized exciton dynamics in a 2D semiconductor heterostructure*, Science **351**, 688–691 (2016).

[Riv18] P. Rivera, H. Yu, K. L. Seyler, N. P. Wilson, W. Yao, and X. Xu, *Interlayer valley excitons in heterobilayers of transition metal dichalcogenides*, Nat. Nanotech. **13**, 1004–1015 (2018).

[Rob16] C. Robert, D. Lagarde, F. Cadiz, G. Wang, B. Lassagne, T. Amand, A. Balocchi, P. Renucci, S. Tongay, B. Urbaszek, and X. Marie, *Exciton radiative lifetime in transition metal dichalcogenide monolayers*, Phys. Rev. B **93**, 205423 (2016).

[Rol14] R. Roldán, J. A. Silva-Guillén, M. P. López-Sancho, F. Guinea, E. Cappelluti, and P. Ordejón, *Electronic properties of single-layer and multilayer transition metal dichalcogenides $MX_2$ (M=Mo,W and X=S, Se)*, Ann. Phys. **526**, 347–357 (2014).

[Ros13] J. S. Ross, S. Wu, H. Yu, N. J. Ghimire, A. M. Jones, G. Aivazian, J. Yan, D. G. Mandrus, D. Xiao, W. Yao, and X. Xu, *Electrical control of neutral and charged excitons in a monolayer semiconductor*, Nat. Commun. **4**, 1474 (2013).

[Ros17] J. S. Ross, P. Rivera, J. Schaibley, E. Lee-Wong, H. Yu, T. Taniguchi, K. Watanabe, J. Yan, D. G. Mandrus, D. Cobden, W. Yao, and X. Xu, *Interlayer Exciton Optoelectronics in a 2D Heterostructure p-n Junction*, Nano Lett. **17**, 638–643 (2017).

[Ros18] M. R. Rosenberger, H.-J. Chuang, K. M. McCreary, A. T. Hanbicki, S. V. Sivaram, and B. T. Jonker, *Nano-Squeegee for the Creation of Clean 2D Material Interfaces*, ACS Appl. Mater. Interfaces **10**, 10379–10387 (2018).

[Rub05] O. Rubel, M. Galluppi, S. D. Baranovskii, K. Volz, L. Geelhaar, H. Riechert, P. Thomas, and W. Stolz, *Quantitative description of disorder parameters in (GaIn)(NAs) quantum wells from the temperature-dependent photoluminescence spectroscopy*, J. Appl. Phys. **98**, 063518 (2005).

[Rub07] O. Rubel, S. D. Baranovskii, K. Hantke, B. Kunert, W. W. Rühle, P. Thomas, K. Volz, and W. Stolz, *Kinetic effects in recombination of optical excitations in disordered quantum heterostructures: Theory and experiment*, J. Lumin. **127**, 285–290 (2007).

[Ryb17] D. V. Rybkovskiy, I. C. Gerber, and M. V. Durnev, *Atomically inspired $k \cdot p$ approach and valley Zeeman effect in transition metal dichalcogenide monolayers*, Phys. Rev. B **95**, 155406 (2017).

[Ryt67] N. S. Rytova, *Screened potential of a point charge in a thin film*, Proc. MSU, Phys., Astron. **3**, 1–5 (1967).

[Sal12] G. Sallen, L. Bouet, X. Marie, G. Wang, C. R. Zhu, W. P. Han, Y. Lu, P. H. Tan, T. Amand, B. L. Liu, and B. Urbaszek, *Robust optical emission polarization in $MoS_2$ monolayers through selective valley excitation*, Phys. Rev. B **86**, 081301(R) (2012).

[Sch16] J. R. Schaibley, H. Yu, G. Clark, P. Rivera, J. S. Ross, K. L. Seyler, W. Yao, and X. Xu, *Valleytronics in 2D materials*, Nat. Rev. Mater. **1**, 16055 (2016).

[Sel16] M. Selig, G. Berghäuser, A. Raja, P. Nagler, C. Schüller, T. F. Heinz, T. Korn, A. Chernikov, E. Malic, and A. Knorr, *Excitonic linewidth and coherence lifetime in monolayer transition metal dichalcogenides*, Nat. Commun. **7**, 13279 (2016).

[Sey18] K. L. Seyler, P. Rivera, H. Yu, N. P. Wilson, E. L. Ray, D. G. Mandrus, J. Yan, W. Yao, and X. Xu, *Signature of moiré-trapped valley excitons in $MoSe_2/WSe_2$ heterobilayers*, arXiv:1809.04562 (2018).

[Sha15] J. Shang, X. Shen, C. Cong, N. Peimyoo, B. Cao, M. Eginligil, and T. Yu, *Observation of Excitonic Fine Structure in a 2D Transition-Metal Dichalcogenide Semiconductor*, ACS Nano **9**, 647–655 (2015).

[Shr18] S. Shree, M. Semina, C. Robert, B. Han, T. Amand, A. Balocchi, M. Manca, E. Courtade, X. Marie, T. Taniguchi, K. Watanabe, M. M. Glazov, and B. Urbaszek, *Observation of exciton-phonon coupling in $MoSe_2$ monolayers*, Phys. Rev. B **98**, 035302 (2018).

[Sie15] E. J. Sie, A. J. Frenzel, Y.-H. Lee, J. Kong, and N. Gedik, *Intervalley biexcitons and many-body effects in monolayer $MoS_2$*, Phys. Rev. B **92**, 125417 (2015).

[Sie16] E. J. Sie, C. H. Lui, Y.-H. Lee, J. Kong, and N. Gedik, *Observation of Intervalley Biexcitonic Optical Stark Effect in Monolayer $WS_2$*, Nano Lett. **16**, 7421–7426 (2016).

[Sko86] M. S. Skolnick, P. R. Tapster, S. J. Bass, A. D. Pitt, N. Apsley, and S. P. Aldred, *Investigation of InGaAs-InP quantum wells by optical spectroscopy*, Semicond. Sci. Technol. **1**, 29–40 (1986).

[Spl10] A. Splendiani, L. Sun, Y. Zhang, T. Li, J. Kim, C.-Y. Chim, G. Galli, and F. Wang, *Emerging Photoluminescence in Monolayer $MoS_2$*, Nano Lett. **10**, 1271–1275 (2010).

[Sri15] A. Srivastava, M. Sidler, A. V. Allain, D. S. Lembke, A. Kis, and A. Imamoğlu, *Valley Zeeman effect in elementary optical excitations of monolayer $WSe_2$*, Nat. Phys. **11**, 141–147 (2015).

[Ste17] P. Steinleitner, P. Merkl, P. Nagler, J. Mornhinweg, C. Schüller, T. Korn, A. Chernikov, and R. Huber, *Direct Observation of Ultrafast Exciton Formation in a Monolayer of $WSe_2$*, Nano Lett. **17**, 1455–1460 (2017).

[Ste18] P. Steinleitner, P. Merkl, A. Graf, P. Nagler, K. Watanabe, T. Taniguchi, J. Zipfel, C. Schüller, T. Korn, A. Chernikov, S. Brem, M. Selig, G. Berghäuser, E. Malic, and R. Huber, *Dielectric Engineering of Electronic Correlations in a van der Waals Heterostructure*, Nano Lett. **18**, 1402–1409 (2018).

[Sti16a] A. V. Stier, K. M. McCreary, B. T. Jonker, J. Kono, and S. A. Crooker, *Exciton diamagnetic shifts and valley Zeeman effects in monolayer $WS_2$ and $MoS_2$ to 65 Tesla*, Nat. Commun. **7**, 10643 (2016).

[Sti16b] A. V. Stier, N. P. Wilson, G. Clark, X. Xu, and S. A. Crooker, *Probing the Influence of Dielectric Environment on Excitons in Monolayer $WSe_2$: Insight from High Magnetic Fields*, Nano Lett. **16**, 7054–7060 (2016).

[Sti18] A. V. Stier, N. P. Wilson, K. A. Velizhanin, J. Kono, X. Xu, and S. A. Crooker, *Magnetooptics of Exciton Rydberg States in a Monolayer Semiconductor*, Phys. Rev. Lett. **120**, 057405 (2018).

[Szy17] M. Szyniszewski, E. Mostaani, N. D. Drummond, and V. I. Fal'ko, *Binding energies of trions and biexcitons in two-dimensional semiconductors from diffusion quantum Monte Carlo calculations*, Phys. Rev. B **95**, 081301(R) (2017).

[Tar01] S. A. Tarasenko, A. A. Kiselev, E. L. Ivchenko, A. Dinger, M. Baldauf, C. Klingshirn, H. Kalt, S. D. Baranovskii, R. Eichmann, and P. Thomas, *Energy relaxation of localized excitons at finite temperature*, Semicond. Sci. Technol. **16**, 486–492 (2001).

[Ter13] H. Terrones, F. Lopez-Urias, and M. Terrones, *Novel hetero-layered materials with tunable direct band gaps by sandwiching different metal disulfides and diselenides*, Sci. Rep. **3**, 1549 (2013).

[Ton13] P. Tonndorf, R. Schmidt, P. Böttger, X. Zhang, J. Börner, A. Liebig, M. Albrecht, C. Kloc, O. Gordan, D. R. T. Zahn, S. Michaelis de Vasconcellos, and R. Bratschitsch, *Photoluminescence emission and Raman response of monolayer $MoS_2$, $MoSe_2$, and $WSe_2$*, Opt. Express **21**, 4908 (2013).

[Ton14] S. Tongay, W. Fan, J. Kang, J. Park, U. Koldemir, J. Suh, D. S. Narang, K. Liu, J. Ji, J. Li, R. Sinclair, and J. Wu, *Tuning interlayer coupling in large-area heterostructures with CVD-grown $MoS_2$ and $WS_2$ monolayers*, Nano Lett. **14**, 3185–3190 (2014).

[Tra18] K. Tran, G. Moody, F. Wu, X. Lu, J. Choi, A. Singh, J. Embley, A. Zepeda, M. Campbell, K. Kim, A. Rai, T. Autry, D. A. Sanchez, T. Taniguchi, K. Watanabe, N. Lu, S. K. Banerjee, E. Tutuc, L. Yang, A. H. MacDonald, K. L. Silverman, and X. Li, *Moiré Excitons in Van der Waals Heterostructures*, arXiv:1807.03771 (2018).

[Tru16] M. Trushin, M. O. Goerbig, and W. Belzig, *Optical absorption by Dirac excitons in single-layer transition-metal dichalcogenides*, Phys. Rev. B **94**, 041301(R) (2016).

[Uge14] M. M. Ugeda, A. J. Bradley, S.-F. Shi, F. H. da Jornada, Y. Zhang, D. Y. Qiu, W. Ruan, S.-K. Mo, Z. Hussain, Z.-X. Shen, F. Wang, S. G. Louie, and M. F. Crommie, *Giant bandgap renormalization and excitonic effects in a monolayer transition metal dichalcogenide semiconductor*, Nat. Mater. **13**, 1091–1095 (2014).

[Uge16] M. M. Ugeda, A. J. Bradley, Y. Zhang, S. Onishi, Y. Chen, W. Ruan, C. Ojeda-Aristizabal, H. Ryu, M. T. Edmonds, H.-Z. Tsai, A. Riss, S.-K. Mo, D. Lee, A. Zettl, Z. Hussain, Z.-X. Shen, and M. F. Crommie, *Characterization of collective ground states in single-layer $NbSe_2$*, Nat. Phys. **12**, 92–97 (2016).

[Unu18] D. Unuchek, A. Ciarrocchi, A. Avsar, K. Watanabe, T. Taniguchi, and A. Kis, *Room-temperature electrical control of exciton flux in a van der Waals heterostructure*, Nature **560**, 340–344 (2018).

[Uwa15] T. Uwanno, Y. Hattori, T. Taniguchi, K. Watanabe, and K. Nagashio, *Fully dry PMMA transfer of graphene on h-BN using a heating/cooling system*, 2D Mater. **2**, 041002 (2015).

[Van17] M. Van der Donck, M. Zarenia, and F. M. Peeters, *Excitons and trions in monolayer transition metal dichalcogenides: A comparative study between the multiband model and the quadratic single-band model*, Phys. Rev. B **96**, 035131 (2017).

[Var67] P. Y. Varshni, *Temperature dependence of the energy gap in semiconductors*, Physica **34**, 149–154 (1967).

[Viñ84] L. Viña, S. Logothetidis, and M. Cardona, *Temperature dependence of the dielectric function of germanium*, Phys. Rev. B **30**, 1979–1991 (1984).

[Wan37] G. H. Wannier, *The Structure of Electronic Excitation Levels in Insulating Crystals*, Phys. Rev. **52**, 191–197 (1937).

[Wan13] L. Wang, I. Meric, P. Y. Huang, Q. Gao, Y. Gao, H. Tran, T. Taniguchi, K. Watanabe, L. M. Campos, D. A. Muller, J. Guo, P. Kim, J. Hone, K. L. Shepard, and C. R. Dean, *One-Dimensional Electrical Contact to a Two-Dimensional Material*, Science **342**, 614–617 (2013).

[Wan14] G. Wang, L. Bouet, D. Lagarde, M. Vidal, A. Balocchi, T. Amand, X. Marie, and B. Urbaszek, *Valley dynamics probed through charged and neutral exciton emission in monolayer $WSe_2$*, Phys. Rev. B **90**, 075413 (2014).

[Wan15a] G. Wang, L. Bouet, M. M. Glazov, T. Amand, E. L. Ivchenko, E. Palleau, X. Marie, and B. Urbaszek, *Magneto-optics in transition metal diselenide monolayers*, 2D Mater. **2**, 034002 (2015).

[Wan15b] G. Wang, E. Palleau, T. Amand, S. Tongay, X. Marie, and B. Urbaszek, *Polarization and time-resolved photoluminescence spectroscopy of excitons in $MoSe_2$ monolayers*, Appl. Phys. Lett. **106**, 112101 (2015).

[Wan15c] G. Wang, C. Robert, A. Suslu, B. Chen, S. Yang, S. Alamdari, I. C. Gerber, T. Amand, X. Marie, S. Tongay, and B. Urbaszek, *Spin-orbit engineering in transition metal dichalcogenide alloy monolayers*, Nat. Commun. **6**, 10110 (2015).

[Wan16a] H. Wang, C. Zhang, W. Chan, C. Manolatou, S. Tiwari, and F. Rana, *Radiative lifetimes of excitons and trions in monolayers of the metal dichalcogenide $MoS_2$*, Phys. Rev. B **93**, 045407 (2016).

[Wan16b] Z. Wang, J. Shan, and K. F. Mak, *Valley- and spin-polarized Landau levels in monolayer $WSe_2$*, Nat. Nanotech. **12**, 144–149 (2016).

[Wan17a] G. Wang, C. Robert, M. M. Glazov, F. Cadiz, E. Courtade, T. Amand, D. Lagarde, T. Taniguchi, K. Watanabe, B. Urbaszek, and X. Marie, *In-Plane Propagation of Light in Transition Metal Dichalcogenide Monolayers: Optical Selection Rules*, Phys. Rev. Lett. **119**, 047401 (2017).

[Wan17b] Z. Wang, L. Zhao, K. F. Mak, and J. Shan, *Probing the Spin-Polarized Electronic Band Structure in Monolayer Transition Metal Dichalcogenides by Optical Spectroscopy*, Nano Lett. **17**, 740–746 (2017).

[Wan18] G. Wang, A. Chernikov, M. M. Glazov, T. F. Heinz, X. Marie, T. Amand, and B. Urbaszek, *Colloquium: Excitons in atomically thin transition metal dichalcogenides*, Rev. Mod. Phys. **90**, 021001 (2018).

[Wie17] J. Wierzbowski, J. Klein, F. Sigger, C. Straubinger, M. Kremser, T. Taniguchi, K. Watanabe, U. Wurstbauer, A. W. Holleitner, M. Kaniber, K. Müller, and J. J. Finley, *Direct exciton emission from atomically thin transition metal dichalcogenide heterostructures near the lifetime limit*, Sci. Rep. **7**, 12383 (2017).

[Wil69] J. A. Wilson and A. D. Yoffe, *The transition metal dichalcogenides discussion and interpretation of the observed optical, electrical and structural properties*, Adv. Phys. **18**, 193–335 (1969).

[Wil17] N. R. Wilson, P. V. Nguyen, K. Seyler, P. Rivera, A. J. Marsden, Z. P. L. Laker, G. C. Constantinescu, V. Kandyba, A. Barinov, N. D. M. Hine, X. Xu, and D. H. Cobden, *Determination of band offsets, hybridization, and exciton binding in 2D semiconductor heterostructures*, Sci. Adv. **3**, e1601832 (2017).

[Wit15] F. Withers, O. Del Pozo-Zamudio, A. Mishchenko, A. P. Rooney, A. Gholinia, K. Watanabe, T. Taniguchi, S. J. Haigh, A. K. Geim, A. I. Tartakovskii, and K. S. Novoselov, *Light-emitting diodes by band-structure engineering in van der Waals heterostructures*, Nat. Mater. **14**, 301–306 (2015).

[Xia07] D. Xiao, W. Yao, and Q. Niu, *Valley-Contrasting Physics in Graphene: Magnetic Moment and Topological Transport*, Phys. Rev. Lett. **99**, 236809 (2007).

[Xia12] D. Xiao, G.-B. Liu, W. Feng, X. Xu, and W. Yao, *Coupled Spin and Valley Physics in Monolayers of $MoS_2$ and Other Group-VI Dichalcogenides*, Phys. Rev. Lett. **108**, 196802 (2012).

[Xu14] X. Xu, W. Yao, D. Xiao, and T. F. Heinz, *Spin and pseudospins in layered transition metal dichalcogenides*, Nat. Phys. **10**, 343–350 (2014).

[Yan17] T. Yan, J. Ye, X. Qiao, P. H. Tan, and X. Zhang, *Exciton valley dynamics in monolayer $WSe_2$ probed by the two-color ultrafast Kerr rotation*, Phys. Chem. Chem. Phys. **19**, 3176–3181 (2017).

[Yao08] W. Yao, D. Xiao, and Q. Niu, *Valley-dependent optoelectronics from inversion symmetry breaking*, Phys. Rev. B **77**, 235406 (2008).

[Ye14] Z. Ye, T. Cao, K. O'Brien, H. Zhu, X. Yin, Y. Wang, S. G. Louie, and X. Zhang, *Probing excitonic dark states in single-layer tungsten disulphide*, Nature **513**, 214–218 (2014).

[Ye18] Z. Ye, L. Waldecker, E. Y. Ma, D. Rhodes, A. Antony, B. Kim, X.-X. Zhang, M. Deng, Y. Jiang, Z. Lu, D. Smirnov, K. Watanabe, T. Taniguchi, J. Hone, and T. F. Heinz, *Efficient generation of neutral and charged biexcitons in encapsulated $WSe_2$ monolayers*, Nat. Commun. **9**, 3718 (2018).

[You06] R. J. Young, R. M. Stevenson, P. Atkinson, K. Cooper, D. A. Ritchie, and A. J. Shields, *Improved fidelity of triggered entangled photons from single quantum dots*, New J. Phys. **8**, 29 (2006).

[You09] A. F. Young and P. Kim, *Quantum interference and Klein tunnelling in graphene heterojunctions*, Nat. Phys. **5**, 222–226 (2009).

[You15] Y. You, X.-X. Zhang, T. C. Berkelbach, M. S. Hybertsen, D. R. Reichman, and T. F. Heinz, *Observation of biexcitons in monolayer $WSe_2$*, Nat. Phys. **11**, 477–481 (2015).

[Yu10] P. Y. Yu and M. Cardona, *Fundamentals of Semiconductors*, Graduate Texts in Physics, Springer, Berlin, 2010.

[Yu13] W. J. Yu, Y. Liu, H. Zhou, A. Yin, Z. Li, Y. Huang, and X. Duan, *Highly efficient gate-tunable photocurrent generation in vertical heterostructures of layered materials*, Nat. Nanotech. **8**, 952–958 (2013).

[Yu14a] H. Yu, G.-B. Liu, P. Gong, X. Xu, and W. Yao, *Dirac cones and Dirac saddle points of bright excitons in monolayer transition metal dichalcogenides*, Nat. Commun. **5**, 3876 (2014).

[Yu14b] T. Yu and M. W. Wu, *Valley depolarization due to intervalley and intravalley electron-hole exchange interactions in monolayer $MoS_2$*, Phys. Rev. B **89**, 205303 (2014).

[Yu15a] H. Yu, X. Cui, X. Xu, and W. Yao, *Valley excitons in two-dimensional semiconductors*, Natl. Sci. Rev. **2**, 57–70 (2015).

[Yu15b] H. Yu, Y. Wang, Q. Tong, X. Xu, and W. Yao, *Anomalous Light Cones and Valley Optical Selection Rules of Interlayer Excitons in Twisted Heterobilayers*, Phys. Rev. Lett. **115**, 187002 (2015).

[Yu17] H. Yu, G.-B. Liu, J. Tang, X. Xu, and W. Yao, *Moiré excitons: From programmable quantum emitter arrays to spin-orbit-coupled artificial lattices*, Sci. Adv. **3**, e1701696 (2017).

[Yun12] W. S. Yun, S. W. Han, S. C. Hong, I. G. Kim, and J. D. Lee, *Thickness and strain effects on electronic structures of transition metal dichalcogenides: 2H-$MX_2$ semiconductors (M=Mo,W; X=S,Se,Te)*, Phys. Rev. B **85**, 033305 (2012).

[Zen12] H. Zeng, J. Dai, W. Yao, D. Xiao, and X. Cui, *Valley polarization in $MoS_2$ monolayers by optical pumping*, Nat. Nanotech. **7**, 490–493 (2012).

[Zen13] H. Zeng, G.-B. Liu, J. Dai, Y. Yan, B. Zhu, R. He, L. Xie, S. Xu, X. Chen, W. Yao, and X. Cui, *Optical signature of symmetry variations and spin-valley coupling in atomically thin tungsten dichalcogenides*, Sci. Rep. **3**, 1608 (2013).

[Zha05] Y. Zhang, Y.-W. Tan, H. L. Stormer, and P. Kim, *Experimental observation of the quantum Hall effect and Berry's phase in graphene*, Nature **438**, 201–204 (2005).

[Zha13a] W. Zhao, Z. Ghorannevis, L. Chu, M. Toh, C. Kloc, P. H. Tan, and G. Eda, *Evolution of Electronic Structure in Atomically Thin Sheets of $WS_2$ and $WSe_2$*, ACS Nano **7**, 791–797 (2013).

[Zha13b] W. Zhao, R. M. Ribeiro, M. Toh, A. Carvalho, C. Kloc, A. H. Castro Neto, and G. Eda, *Origin of Indirect Optical Transitions in Few-Layer $MoS_2$, $WS_2$, and $WSe_2$*, Nano Lett. **13**, 5627–5634 (2013).

[Zha14] Y. Zhang, T.-R. Chang, B. Zhou, Y.-T. Cui, H. Yan, Z. Liu, F. Schmitt, J. Lee, R. Moore, Y. Chen, H. Lin, H.-T. Jeng, S.-K. Mo, Z. Hussain, A. Bansil, and Z.-X. Shen, *Direct observation of the transition from indirect to direct bandgap in atomically thin epitaxial $MoSe_2$*, Nat. Nanotech. **9**, 111–115 (2014).

[Zha15a] C. Zhang, Y. Chen, A. Johnson, M.-Y. Li, L.-J. Li, P. C. Mende, R. M. Feenstra, and C.-K. Shih, *Probing Critical Point Energies of Transition Metal Dichalcogenides: Surprising Indirect Gap of Single Layer $WSe_2$*, Nano Lett. **15**, 6494–6500 (2015).

[Zha15b] D. K. Zhang, D. W. Kidd, and K. Varga, *Excited Biexcitons in Transition Metal Dichalcogenides*, Nano Lett. **15**, 7002–7005 (2015).

[Zha15c] X.-X. Zhang, Y. You, S. Y. F. Zhao, and T. F. Heinz, *Experimental Evidence for Dark Excitons in Monolayer $WSe_2$*, Phys. Rev. Lett. **115**, 257403 (2015).

[Zha15d] Y. Zhang, H. Li, H. Wang, R. Liu, S.-L. Zhang, and Z.-J. Qiu, *On Valence-Band Splitting in Layered $MoS_2$*, ACS Nano **9**, 8514–8519 (2015).

[Zha16] W. Zhang, Q. Wang, Y. Chen, Z. Wang, and A. T. S. Wee, *Van der Waals stacked 2D layered materials for optoelectronics*, 2D Mater. **3**, 022001 (2016).

[Zha17a] C. Zhang, C.-P. Chuu, X. Ren, M.-Y. Li, L.-J. Li, C. Jin, M.-Y. Chou, and C.-K. Shih, *Interlayer couplings, Moiré patterns, and 2D electronic superlattices in $MoS_2/WSe_2$ hetero-bilayers*, Sci. Adv. **3**, e1601459 (2017).

[Zha17b] X.-X. Zhang, T. Cao, Z. Lu, Y.-C. Lin, F. Zhang, Y. Wang, Z. Li, J. C. Hone, J. A. Robinson, D. Smirnov, S. G. Louie, and T. F. Heinz, *Magnetic brightening and control of dark excitons in monolayer $WSe_2$*, Nat. Nanotech. **12**, 883–888 (2017).

[Zhu11] Z. Y. Zhu, Y. C. Cheng, and U. Schwingenschlögl, *Giant spin-orbit-induced spin splitting in two-dimensional transition-metal dichalcogenide semiconductors*, Phys. Rev. B **84**, 153402 (2011).

[Zhu14] C. R. Zhu, K. Zhang, M. Glazov, B. Urbaszek, T. Amand, Z. W. Ji, B. L. Liu, and X. Marie, *Exciton valley dynamics probed by Kerr rotation in $WSe_2$ monolayers*, Phys. Rev. B **90**, 161302(R) (2014).

[Zip18] J. Zipfel, J. Holler, A. A. Mitioglu, M. V. Ballottin, P. Nagler, A. V. Stier, T. Taniguchi, K. Watanabe, S. A. Crooker, P. C. M. Christianen, T. Korn, and A. Chernikov, *Spatial extent of the excited exciton states in $WS_2$ monolayers from diamagnetic shifts*, Phys. Rev. B **98**, 075438 (2018).

[Zom11] P. J. Zomer, S. P. Dash, N. Tombros, and B. J. van Wees, *A transfer technique for high mobility graphene devices on commercially available hexagonal boron nitride*, Appl. Phys. Lett. **99**, 232104 (2011).

# List of publications


1. P. Nagler, G. Plechinger, C. Schüller, and T. Korn, *Observation of anisotropic interlayer Raman modes in few-layer $ReS_2$*, Phys. Status Solidi-Rapid Res. Lett. **10**, 185–189 (2015).

2. G. Plechinger, P. Nagler, J. Kraus, N. Paradiso, C. Strunk, C. Schüller, and T. Korn, *Identification of excitons, trions and biexcitons in single-layer $WS_2$*, Phys. Status Solidi-Rapid Res. Lett. **9**, 457–461 (2015).

3. C. Poellmann, P. Steinleitner, U. Leierseder, P. Nagler, G. Plechinger, M. Porer, R. Bratschitsch, C. Schüller, T. Korn, and R. Huber, *Resonant internal quantum transitions and femtosecond radiative decay of excitons in monolayer $WSe_2$*, Nat. Mater. **14**, 889–894 (2015).

4. K. Hao, L. Xu, P. Nagler, A. Singh, K. Tran, C. K. Dass, C. Schüller, T. Korn, X. Li, and G. Moody, *Coherent and Incoherent Coupling Dynamics between Neutral and Charged Excitons in Monolayer $MoSe_2$*, Nano Lett. **16**, 5109–5113 (2016).

5. F. Langer, M. Hohenleutner, C. P. Schmidt, C. Poellmann, P. Nagler, T. Korn, C. Schüller, M. S. Sherwin, U. Huttner, J. T. Steiner, S. W. Koch, M. Kira, and R. Huber, *Lightwave-driven quasiparticle collisions on a subcycle timescale*, Nature **533**, 225–229 (2016).

6. G. Plechinger, P. Nagler, A. Arora, R. Schmidt, A. Chernikov, A. Granados del Águila, P. C. M. Christianen, R. Bratschitsch, C. Schüller, and T. Korn, *Trion fine structure and coupled spin-valley dynamics in monolayer tungsten disulfide*, Nat. Commun. **7**, 12715 (2016).

7. R. Schmidt, A. Arora, G. Plechinger, P. Nagler, A. Granados del Águila, M. V. Ballottin, P. C. M. Christianen, S. M. de Vasconcellos, C. Schüller, T. Korn, and R. Bratschitsch, *Magnetic-Field-Induced Rotation of Polarized Light Emission from Monolayer $WS_2$*, Phys. Rev. Lett. **117**, 077402 (2016).

8. G. Plechinger, P. Nagler, A. Arora, A. Granados del Águila, M. V. Ballottin, T. Frank, P. Steinleitner, M. Gmitra, J. Fabian, P. C. M. Christianen, R. Bratschitsch, C. Schüller, and T. Korn, *Excitonic Valley Effects in Monolayer $WS_2$ under High Magnetic Fields*, Nano Lett. **16**, 7899–7904 (2016).

9. P. Steinleitner, P. Merkl, P. Nagler, J. Mornhinweg, C. Schüller, T. Korn, A. Chernikov, and R. Huber, *Direct Observation of Ultrafast Exciton Formation in a Monolayer of $WSe_2$*, Nano Lett. **17**, 1455–1460 (2017).

10. M. Gehlmann, I. Aguilera, G. Bihlmayer, S. Nemsak, P. Nagler, P. Gospodaric, G. Zamborlini, M. Eschbach, V. Feyer, F. Kronast, E. Mlynczak, T. Korn, L. Plucinski, C. Schüller, S. Blügel, and C. M. Schneider, *Direct Observation of the Band Gap Transition in Atomically Thin $ReS_2$*, Nano Lett. **17**, 5187–5192 (2017).

11. P. Nagler, G. Plechinger, M. V. Ballottin, A. A. Mitioglu, S. Meier, N. Paradiso, C. Strunk, A. Chernikov, P. C. M. Christianen, C. Schüller, and T. Korn, *Interlayer exciton dynamics in a dichalcogenide monolayer heterostructure*, 2D Mater. **4**, 025112 (2017).

12. P. Nagler, M. V. Ballottin, A. A. Mitioglu, F. Mooshammer, N. Paradiso, C. Strunk, R. Huber, A. Chernikov, P. C. M. Christianen, C. Schüller, and T. Korn, *Giant magnetic splitting inducing near-unity valley polarization in van der Waals heterostructures*, Nat. Commun. **8**, 1551 (2017).

13. R. P. Puchert, F. Steiner, G. Plechinger, F. Hofmann, I. Caspers, J. Kirschner, P. Nagler, A. Chernikov, C. Schüller, T. Korn, J. Vogelsang, S. Bange, and J. M. Lupton, *Spectral focusing of broadband silver electroluminescence in nanoscopic FRET-LEDs*, Nat. Nanotechnol. **12**, 637–641 (2017).

14. N. Lundt, P. Nagler, A. Nalitov, S. Klembt, M. Wurdack, S. Stoll, T. H. Harder, S. Betzold, V. Baumann, A. V. Kavokin, C. Schüller, T. Korn, S. Höfling, and C. Schneider, *Valley polarized relaxation and upconversion luminescence from Tamm-plasmon trion-polaritons with a $MoSe_2$ monolayer*, 2D Mater. **4**, 025096 (2017).

15. G. Plechinger, P. Nagler, A. Arora, R. Schmidt, A. Chernikov, J. M. Lupton, R. Bratschitsch, C. Schüller, and T. Korn, *Valley Dynamics of Excitons in Monolayer Dichalcogenides*, Phys. Status Solidi-Rapid Res. Lett. **11**, 1700131 (2017).

16. M. Schwemmer, P. Nagler, A. Hanninger, C. Schüller, and T. Korn, *Long-lived spin polarization in n-doped $MoSe_2$ monolayers*, Appl. Phys. Lett. **111**, 082402 (2017).

17. K. Hao, L. Xu. F. Wu, P. Nagler, K. Tran, X. Ma, C. Schüller, T. Korn. A. H. McDonald, G. Moody, and X. Li, *Trion valley coherence in monolayer semiconductors*, 2D Mater. **4**, 025105 (2017).

18. R. Frisenda, J. O. Island, J. L. Lado, E. Giovanelli, P. Gant, P. Nagler, S. Bange, J. M. Lupton, C. Schüller, A. J. Molina-Mendoza, L. Aballe, M. Foerster, T. Korn, M. A. Nino, D. P. de Lara, E. M. Pérez, J. Fernandéz-Rossier, and A. Castellanos-Gomez, *Characterization of highly crystalline lead iodide nanosheets prepared by room-temperature solution processing*, Nanotechnology **28**, 455703 (2017).

19. M. Selig, G. Berghäuser, A. Raja, P. Nagler, C. Schüller, T. F. Heinz, T. Korn, A. Chernikov, E. Malic, and A. Knorr, *Excitonic linewidth and coherence lifetime in monolayer transition metal dichacogenides*, Nat. Commun. **7**, 13279 (2017).

20. K. Hao, J. F. Specht, P. Nagler, L. Xu, K. Tran, A. Singh, C. K. Dass, C. Schüller, T. Korn, M. Richter, A. Knorr, X. Li, and G. Moody, *Neutral and charged intervalley biexcitons in monolayer $MoSe_2$*, Nat. Commun. **8**, 15552 (2017).

21. N. Lundt, S. Stoll, P. Nagler, A. Nalitov, S. Klembt, S. Betzold, J. Goddard, E. Frieling, A. V. Kavokin, C. Schüller, T. Korn, S. Höfling, and C. Schneider, *Observation of macroscopic valley-polarized monolayer exciton-polaritons at room temperature*, Phys. Rev. B **96**, 241403(R) (2017).

22. A. Raja, A. Chaves, J. Yu. G. Arefe, H. M. Hill, A. F. Rigosi, T. C. Berkelbach, P. Nagler, C. Schüller, T. Korn, C. Nuckolls, J. Hone, L. E. Brus, T. F. Heinz, D. R. Reichman, and A. Chernikov, *Coulomb engineering of the bandgap and excitons in two-dimensional materials*, Nat. Commun. **8**, 15251 (2017).

23. P. Steinleitner, P. Merkl, A. Graf, P. Nagler, J. Zipfel, C. Schüller, T. Korn, A. Chernikov, R. Huber, S. Brem, M. Selig, G. Berghäuser, and E. Malic, *Dielectric Engineering of Electronic Correlations in a van der Waals Heterostructure*, Nano Lett. **18**, 1402–1409 (2018).

24. M. Kulig, J. Zipfel, P. Nagler, S. Blanter, C. Schüller, T. Korn, N. Paradiso, M. M. Glazov, and A. Chernikov, *Exciton diffusion and halo effects in atomically thin semiconductors*, Phys. Rev. Lett. **120**, 207401 (2018).

25. J. Kunstmann, F. Mooshammer, P. Nagler, A. Chaves, F. Stein, N. Paradiso, G. Plechinger, C. Strunk, C. Schüller, G. Seifert, D. R. Reichmann, and T. Korn, Momentum-space indirect interlayer excitons in transition-metal dichalcogenide van der Waals heterostructures, Nat. Phys. **14**, 801–805 (2018).

26. F. Langer, C. P. Schmidt, S. Schlauderer, M. Gmitra, J. Fabian, P. Nagler, C. Schüller, T. Korn, P. G. Hawkins, J. T. Steiner, U. Huttner, S. W. Koch, M. Kira, and R. Huber, *Lightwave valleytronics in a monolayer of tungsten diselenide*, Nature **557**, 76–80 (2018).

27. P. Nagler, M. V. Ballottin, A. A. Mitioglu, M. V. Durnev, T. Taniguchi, K. Wantanabe, A. Chernikov, M. M. Glazov, P. C. M. Christianen, C. Schüller, and T. Korn, *Zeeman Splitting and Inverted Polarization of Biexciton Emission in Monolayer $WS_2$*, Phys. Rev. Lett. **121**, 057402 (2018).

28. J. Zipfel, J. Holler, A. A. Mitioglu, M. V. Ballottin, P. Nagler, A. V. Stier, T. Taniguchi, K. Wantanabe, S. A. Crooker, P. C. M. Christianen, T. Korn, and A. Chernikov, *Spatial extent of the excited exciton states in $WS_2$ monolayers from diagmagnetic shifts*, Phys. Rev. B **98**, 075438 (2018).

29. T. Völkl, D. Kochan, T. Ebnet, S. Ringer, D. Schiermeier, P. Nagler, T. Korn, C. Schüller, J. Fabian, D. Weiss, and J. Eroms, *Abscence of a giant spin Hall effect in plasma hydrogenated graphene*, Phys. Rev. B **99**, 085401 (2019).

30. P. Merkl, P. Steinleitner, F. Mooshammer, K. Lin, P. Nagler, J. Holler, C. Schüller, J. M. Lupton, T. Korn, S. Ovesen, S. Brem, E. Malic, and R. Huber, *Ultrafast transition between exciton phases in van der Waals heterostructures*, Nat. Mater., in press (2019).

# Danksagung

An dieser Stelle möchte ich mich bei allen bedanken, die mich während meiner Zeit als Doktorand und auf dem Weg zur Fertigstellung dieser Arbeit begleitet und unterstützt haben.
Besonders danken will ich hierbei meinem Betreuer *Prof. Dr. Tobias Korn*, der es mir ermöglicht hat, in diesem aktuellen und dynamischen Forschungsfeld zu arbeiten und zu promovieren. Vielen Dank für die hervorragende Betreuung, das entgegengebrachte Vertrauen, die Unterstützung im Labor, die Genehmigung zahlreicher Forschungsaufenthalte und Konferenzbesuche im In- und Ausland und die stets offene Tür bei Fragen jeder Art.
Vielen Dank an *Prof. Dr. Christian Schüller* für die freundliche Aufnahme in die Arbeitsgruppe, die Finanzierung eines Großteils meiner Stelle über das Graduiertenkolleg und die vielen angenehmen Gespräche. Bei *Prof. Dr. Rupert Huber* möchte ich mich für die Übernahme der Zweitkorrektur dieser Arbeit und die tolle wissenschaftliche Zusammenarbeit während der letzten Jahre bedanken.
Ein großer Dank geht an *Alexey Chernikov* für die vielen unterhaltsamen wissenschaftlichen und nicht-wissenschaftlichen Gespräche auf großen wie auf kleinen Runden und den wesentlichen Beitrag bei mehreren Projekten dieser Arbeit. Eine besondere Freude war es auch, mit *Gerd Plechinger* zusammenzuarbeiten und in das Feld der 2D Materialien einzutauchen. Die gemeinsamen Auslandskonferenzen und insbesondere unser Aufenthalt in Nijmegen im Jahr 2015 werden mir immer im Gedächtnis bleiben. Vielen Dank an das Team vom Hochfeld-Magnetlabor in Nijmegen, insbesondere *Dr. Anatolie Mitioglu*, *Mariana Ballottin*, *Dr. Andrés Granados del Águila* und *Prof. Dr. Peter Christianen* für die tolle Arbeitsatmospähre vor Ort und den unermüdlichen Einsatz zu jeder Tag- und insbesondere Nachtzeit. Ebenso bedanken will ich mich bei *Prof. Dr. Mikhail Glazov* und *Dr. Mikhail Durniev* vom Ioffe Institut in St. Petersburg für die äußerst angenehme und fruchtbare Zusammenarbeit im Rahmen des Biexzitonen-

Projekts, bei *Fabian Mooshammer* für seine SHG Messungen an Heterostrukturen und das ausführliche Korrekturlesen der Arbeit und bei *Nicola Paradiso* für das Annealen der Proben.
Ein herzliches Dankeschön geht vor allem auch an meine aktuellen und ehemaligen Kollegen der Arbeitsgruppe, *Sven Gelfert*, *Christian Gradl*, *Johannes Holler*, *Michael Kempf*, *Sebastian Meier*, *Christoph Schönhuber*, *Gerd Plechinger* und *Markus Schwemmer* für die großartige und sehr gemeinschaftliche Arbeitsatmosphäre und viele schöne Erlebnisse auch außerhalb der Universität. Gleiches gilt für die Mitglieder der AG Lupton, darunter insbesondere *Robin Puchert* und *Josef Haimerl*. Vielen Dank für viele gemeinsame angenehme Stunden. Danke auch an alle Mitglieder des Mittagsmeetings und die Freizeitschwimmer am Nachmittag.
Abschließend will ich meiner Familie und meiner Freundin Maresa für die langjährige Unterstützung danken.